Feasibility of curved pipe pull operations on sandy seabeds

by

Ing. J. Noorman

to obtain the degree of Master of Science
at the Delft University of Technology,

Student number:	4325818	
Project duration:	August, 2018 – September, 2019	
Thesis committee:	Prof. dr. ir. K.G. Gavin	TU Delft, Chairman
	Dr. ir. D.J. Peters	TU Delft, Daily supervisor
	Dr. ir. A. Askarinejad	TU Delft, Supervisor
	Ir. A.A.J. Smit	Boskalis, Daily supervisor

This thesis is confidential and cannot be made public until September 11, 2021. Op dit verslag is geheimhouding van toepassing tot en met 11 september 2021.

TU Delft Boskalis

Abstract

Due to often existing subsea infrastructure or challenging seabed conditions, engineers are forced to design new nearshore pipeline trajectories that are not always in a straight line. Since subsea tie-in operations are often complex and relatively expensive, alternative methods like pulling pipelines into a curve are worthwhile. By means of this research fundamental knowledge of pipe pull operations into curved trajectories is acquired.

This thesis research focuses on the soil - structure interaction between the sliding pipeline and the seabed. A more thorough understanding is obtained of the geotechnical processes that create lateral resistance of the pipeline against the forces applied by the installation vessel. The main goal behind this thesis is to expand the capabilities of pipeline installation by exploring the feasibility of curved pipe pull projects.

The research is based on three fundamental elements:

1. An extensive theoretical study
2. A validated numerical soil-structure interaction model
3. A successful physical test campaign of thirty-two experiments

The theoretical study of the thesis focuses on the physical processes that play a role during curved pipe pull operations. Research is conducted to gather knowledge of the three main subjects of research, being:

1. Structural behaviour of a concrete covered pipeline
2. Geotechnical behaviour of soil under lateral pipeline displacement
3. Geotechnical behaviour of soil under axial pipeline displacement

Since this was the first known research into curved pipe pull operations, influences of dynamic environmental loads are excluded from the scope of research.

The second stage of the research focused on creating an engineering model that enabled to predict to what extend partially embedded pipelines can be pulled into a curved trajectory on sandy seabeds. After considering multiple simpler structural models, the final result was a non-linear spring supported tensioned bending beam model. Within this computational prediction model: the lateral soil resistance is modeled by means of a P(Y) spring model, while the pipeline is represented by the tensioned bending beam. The applied lateral soil resistance model is computed based on researches of Wang et al. (2018) and Verley and Sotberg (1994).

After the model was completed, a purpose made test facility was created to pull scaled pipelines into a curved trajectory. During the test-campaign, five different model pipelines were tested on a scale range of 1/11.8 to 1/5.3. The physical test campaign provided valuable experimental data of thirty-two successful drained curved pipe pull tests.

By means of the acquired set of experimental data the model was able to be validated. Since the model pipelines differed in diameter, specific weight and bending stiffness, the influence of those parameters is examined. From the fact that the majority of the model pipelines was pulled into a radius that was 0-30% lower than the computed radius, we can state that the numerical model predictions gives a well defined upper limit of the controlled pull radius of pipelines.

Along the classified critical curved pulls, the imposed lateral force during the experiments was within 20% of the maximum predicted force in 86% of the physical tests. From this observation we can conclude that the numerical model captures the maximum lateral pull force with a high accuracy.

Contents

List of Tables

List of Figures

List of abbreviations

Throughout this research certain abbreviations are used. The meaning of the mentioned abbreviations are listed on this page.

2D	Two-Dimensional
3D	Three-Dimensional
CPT	Cone Penetration Test
DNV	Det Norske Veritas
EOM	Equation Of Motion
GCP	Ground Control Point
PLEM	Pipeline End Manifold
PVC	PolyVinyl Chloride

Nomenclature

Throughout this research symbols are used to represent certain parameters. The meaning of the used symbols are listed within this nomenclature.

Symbol	Explanation	Unit
α	Pull angle	$[°]$
γ'	Effective soil unit weight	$[N/m^3]$
ε_c	Strain of the concrete weight coating	[%]
$\varepsilon_{c,ax}(z,x,t)$	Strain of the concrete weight coating, caused by tension	[%]
$\varepsilon_c(z,x,t)$	Strain of the concrete weight coating	[%]
ε_s	Strain of the steel pipeline	[%]
$\varepsilon_T(y,t)$	Tension component of strain	[%]
$\varepsilon(y,x,t)$	Strain of the material	[%]
θ	Pipeline deflection	$[°]$
$\kappa(x,t)$	Curvature of the member	$[m^{-1}]$
λ	Scale factor	$[-]$
μ	Friction factor	$[-]$
ϕ	Internal friction angle of the granular material	$[°]$
ρ	Density	$[N/m^3]$
ρ	Mass density	$[N/m^2]$
ρ_s	Grain density	$[N/m^3]$
σ'_v	Effective vertical soil pressure	$[N/m^2]$
a	Transverse acceleration	$[m/s^2]$
A	Cross-sectional area	$[m^2]$
A_c	Cross-sectional area of pipeline concrete weight coating	$[N]$
A_s	Cross-sectional area of pipeline steel	$[N]$
D	Diameter pipeline	$[m]$
D_r	Relative density	$[-]$
e	Void ratio	$[-]$
E	Young's modulus member	$[N/m^2]$
E_c	Young's modulus of concrete	$[N/mm^2]$
E_s	Young's modulus of steel	$[N/mm^2]$
F_f	Friction force	$[N]$
$F_{L,brk,d}$	Lateral force at breakout in drained soil conditions	$[N/m]$
F_p	Passive soil resistance	$[N]$
I	Moment of inertia member	$[m^4]$
L	Model pipe length	$[°]$
$L_{fullscale}$	Full dimension	$[m]$
L_{model}	Model dimension	$[m]$
m	Mass	$[N]$
M	Bending moment	$[Nm]$
n	Porosity	$[-]$
q_c	Cone resistance	$[N/m^2]$
q_1	External vertical load	$[-]$
$R(x,t)$	Radius of the pipeline	$[-]$
$T(x,t)$	Tensile force in the pipeline	$[N]$
V	Vertical component tension	$[N]$
V	Vertical pipe-soil force per unit length	$[N/m]$
$V(x)$	Shear force	$[N]$

Symbol	Explanation	Unit
w	Transverse motion	$[m]$
W	Weight of the pipeline	$[N]$
z	Embedment (measured from original seabed level)	$[m]$
z	Level within cross-section from neutral axis	$[m]$
z/D	Normalized pipeline embedment	$[-]$

Preface

You just started reading the report of the research I conducted in order to obtain my Master of Science degree at the Delft University of Technology. A good friend of mine once told me, I should consider it as the crown on my academic studies. And, although it took me a bunch of effort to finish, I can safely say I am incredibly proud of the crown that I put on my Master.

Throughout the thirteen months during journey, Boskalis facilitated me to combine practical experiments and academic modelling into one research. This suited great to my professional career so far, which included gaining on-site experience and academic knowledge as well. In the end, the physical test results of our experimental campaign fitted the numerical model computations well. These satisfying results gave me (and the project team) a rush of enthusiasm that made the amount of work that went into this research worth-while.

I would not have been able to finish my thesis and Master without the support of my supervisors and loved ones.

First of all; I would like to thank my committee-members and involved colleagues, in particular my daily supervisor Axel Smit. Each of you supported me with patient advice and reviewed my work with great constructive criticism. I admired the way we worked together to make this research into a success, and I hope to work together again one day. You again reminded me how cool and challenging the civil / offshore industry can be.

Second; I would like to thank my girlfriend, sister, family and friends (including my new fellow Boskalis graduate friends) for the mental support that you gave me throughout my studies and thesis. If I needed a chat, some time off or a hug you were able to give them to me and I would not have been able to finish it off without those. It is a shame that I had to sacrifice our mutual time to enjoy the nice things in life, but I know we will catch up these moments as soon as possible!

Last but not least; I have to thank my loving parents. Throughout my life, I was always supported with love and goods to establish where I am at this point in life.
Unfortunately; my dad, Anne Noorman, will not be able to witness my graduation, since he sadly passed away two years ago. He inspired me to become an engineer, as he was into engineering too. Throughout his career he encountered the feeling that he reached an imaginary ceiling, because he did not have a Bachelor or Master Degree. He did not want me to feel such thing and therefore supported me with an incredible trust that I would reach this goal. Even after he left us, I still felt his support every day since.

I am very glad that I will graduate Delft University of Technology, but I will always have respect for the ones who obtained their knowledge from practical experience too.

This one is for you dad!

Jaimy Noorman
Breda, September 2019

1
Introduction

Figure 1.1: Pipeline pull-out operation in Magellan, Argentina

1.1. Topic of this research

Due to often existing subsea infrastructure or seabed conditions, engineers are forced to design new nearshore pipeline trajectories that are not always in a straight line. Since subsea tie-in operations are often complex and relatively expensive, alternative methods like pulling pipelines into a curve are worthwhile. By means of this research fundamental knowledge of pipe pull operations into curved trajectories is acquired.

This thesis research of MSc Civil Engineering graduate Jaimy Noorman focuses on the soil - structure interaction between the sliding pipeline and the seabed. A more thorough understanding is obtained of the geotechnical processes that create lateral resistance of the pipeline against the forces applied by the installation vessel. The main goal behind this thesis is to expand Boskalis' market share in pipeline installation by exploring the feasibility of curved pipe pull projects.

1.2. Installation methods of nearshore pipelines

Although the renewable energy market has grown exponentially over the last decades, a substantial amount of offshore oil and gas projects are expected to keep arising in the near future. These offshore oil and gas projects often depend on pipelines to transport their crude products towards the refinery plants onshore. Hence globally still thousands of kilometers of offshore pipeline are installed on a yearly basis.

The majority of these offshore pipelines are installed by means of large offshore pipelay vessels. Offshore pipelay vessels are designed to operate and install pipelines in deep water conditions (>10m). Obviously, the pipelines need to cross, often shallow, nearshore areas to be connected to the shore. In these shallow water conditions pipe lay solutions are cumbersome due to the large draught of the pipe lay vessels. Therefore most pipelines in nearshore areas are installed by pulling them across the seabed.

1.2.1. Pull-out versus pull-in method

Two options of installation of marine pipelines by means of the pulling method are the pull-in and the pull-out methods. Pipelines are pulled in axial direction by means of a pull head and steel pull wire. During a pull-in, pipeline sections (with a standard length of 12.2 meter) are connected on board of an offshore situated pipelay vessel or barge and pulled in shore-ward direction. The pipeline is guided from board, by for instance a stinger, and pulled by means of a land-based linear winch. Boskalis' most recent nearshore pull-in operation can be observed in figure 1.2.

Figure 1.2: Pull-in operation from pipelay vessel stinger in Kurgalsky, Russia

During a pull-out, pipeline strings, consisting of multiple pipeline sections, are connected on-shore and pulled in offshore direction. The pipeline will leave the shore via a landfall and is pulled offshore by means of a linear winch onboard of an offshore positioned barge or installation vessel. An example of a pull-out procedure is displayed in figure 1.3.

Figure 1.3: Pull-out operation from shore in Magellan, Argentina

The length of the pipeline strings is chosen most favourable for the given project site. After creating a durable weld connection, including a composite cover juncture, the pipeline strings are stored in the stringing yard. At the right side of figure 1.4 an example of a stringing yard of a former project can be observed.

Figure 1.4: Example of a firing lane (l) and stringing yard (r) in Magellan, Argentina

Although Boskalis has successfully installed dozens of nearshore pipelines by the two former mentioned methods, the company has not yet installed pipelines into curved trajectories. Aforementioned methods are applied if a pipeline trajectory is in a straight line. In other cases, where natural or artificial obstacle prevent straight pipeline trajectories, the pipeline will have to be installed around it. This can either be realized by connecting two straight pipelines by means of subsea tie-in or by means of a curved a pipe pull operation. Since subsea tie-in operation are labour intensive and relatively expensive, considering curved pipe pull operations becomes worthwhile.

This new kind of projects ask for an adopted installation method which applies a lateral force to the pipeline, enabling it to curve during the pull operation. An adapted version of the pull-out method has proven to have the broadest support within Boskalis to install pipelines into curved trajectories. The focus of this research will therefore be based on this adapted pull-out method, further prescribed in the following subsection.

1.2.2. Adapted pull-out method

The installation of pipelines into nearshore curved trajectories asks for an adaption of the currently used installation methods mentioned in the previous section 1.2.1. This new, adapted pull-out method will be prescribed in this subsection.

To visualize the curved pull-out method, a fictitious project case involving a curved pipeline trajectory is displayed in figure 1.5. Within this fictitious project case, a pipeline is intended to connect an onshore refinery to a pipeline end manifold (or PLEM) by means of a subsea pipeline. A PLEM is a structure that serves as a offshore positioned manifold to split the product flow of the pipeline into multiple routes. Seabed conditions and petrochemical protected areas forced engineers to design a curved pipe trajectory in order to connect the landfall with the PLEM.

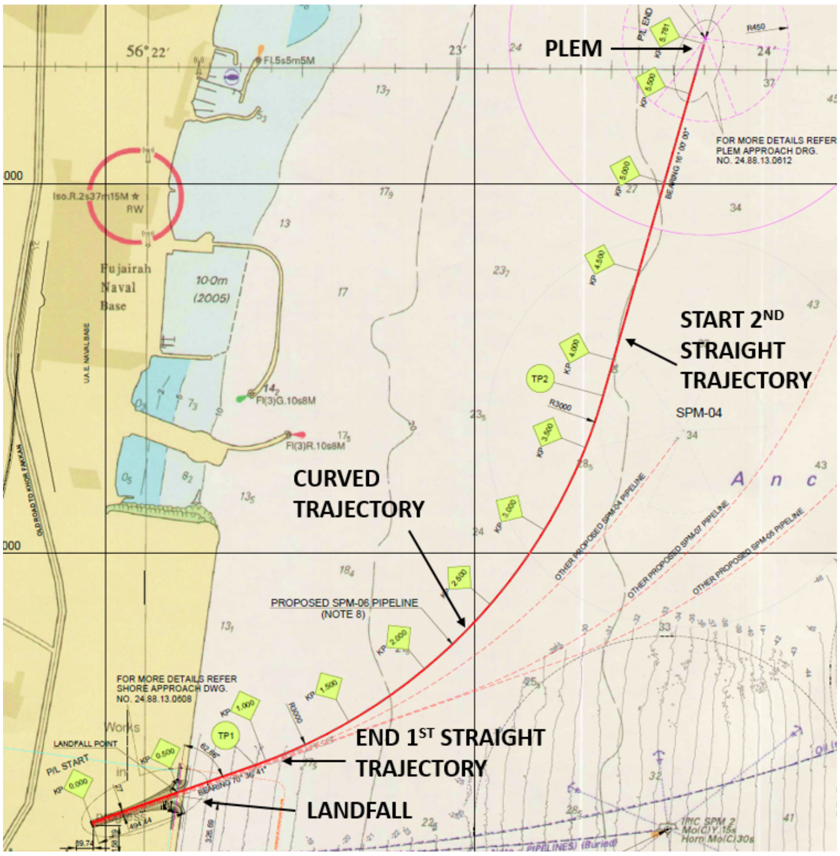

Figure 1.5: Example of a fictitious curved pipe pull trajectory

Throughout this research, the adapted pull-out method will form the base case of predicting model computations and physical experiments. Hence, the computations and tests relate to the future installation method that Boskalis has in mind.

Start of the adapted pull-put
During the adapted pull-out method, the set-up is comparable to that of a standard pull-out procedure. When a sufficient amount of pipeline strings is produced and ready to be installed, the pull-out procedure is initiated. The first pipeline string is installed onto rollers (the so-called firing lane) to reduce the force required to obtain axial movement, easing the pull-out. This process can be observed in figure 1.4. Offshore, an installation vessel or barge is situated. By means of a pre-layed messenger wire, the actual pull-wire is brought from installation vessel to shore. The pull wire is connected to the pipeline via a pull head. The aforementioned procedures are repeated until the desired pipeline length is pulled out.

After a certain amount of time the pipe string has most of her length off the rollers and onto the seabed. A new section of pipe string can be installed onto the empty space on the rollers. First and second string of the pipeline can be connected by means of an aforementioned durable connection, same as that of the pipe sections. The pipeline now consists of two pipeline strings and the pull-out procedure can continue by pulling the pipeline offshore another pipe string length, onto the seabed.

A visualization of the first step of the curved pullout procedure can be observed in the 1.6

Curved trajectory of the adapted pull-out method
The aforementioned cycle has to be repeated until the pipe head has reached the desired start position of the

curved pipeline trajectory. There, the role of the installation vessel will become much more dynamic as it was during the first part of the installation.

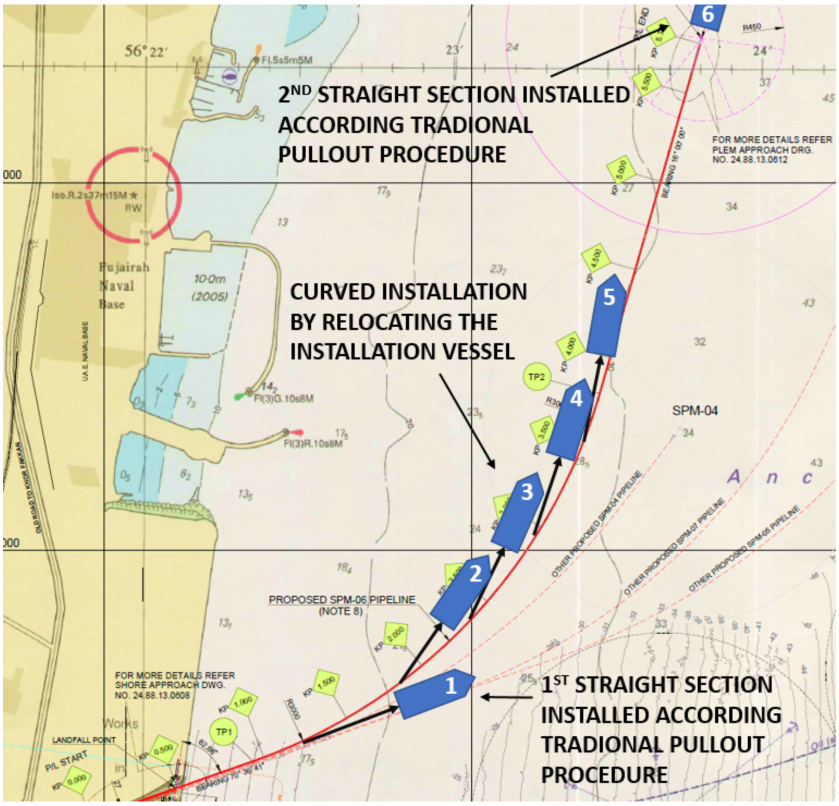

Figure 1.6: Example of a fictitious curved pipe pull trajectory

While the installation vessel first was in a static position over the previous part of the installation, this vessel will now reposition itself to the inner side of the proposed pipeline curve trajectory (as visualized in step 2 of figure 1.6). During the curved part of the pull, the pull wire should approach the pipe head with as little seabed interaction as possible. Since the installation vessel is on the inner side of the curved pipe trajectory, the vessel is able to pull on the pull head under an angle. The axial part of this inclined pull force will cause the pipeline to move in axial direction. The lateral component of the load will, if controlled successfully, forces the pipeline into a curve during the pull. Controlling the curved pull out method will be a delicate process with lots of project specific variables. The influence of these variables is discussed in chapter 5, and determine the maximum angle and minimum radius at which the pipeline can be pulled in a controlled manner.

During the curved pull, the pipeline is expected to align itself with the pull wire. It is of major importance that the pull wire connection keeps a horizontal position during a pull; as it should not lift the pipe head from the seabed. If the inclination of the pull wire and pipeline has become too small (and the applied lateral force has decreased too much), the installation vessel should be re-positioned towards the inner bend. Repositioning of the installation vessel is visualized in step 3-5 of figure 1.6.

After the curved trajectory of the adapted pull-out method

After the desired amount of re-positioned pulls the pipeline is installed in a curved trajectory. If desired, the pipeline can be pulled in a straight trajectory after the curved section. This position of the installation vessel throughout the pull of the latter prescribed straight pull traject can be observed in figure 1.6, vessel position 6.

1.3. Scope of this research

By excluding particular subjects out of the scope of research, the actual focus of the research becomes clear. Within this section one can read which subjects are included into the scope and which are not.

At first, during an actual pipe pull operation the pipeline is subject to different load effects. Since the focus of this research is to obtain the build-up of axial and lateral resistance during a pulling operation as a function of pipe displacement, it is important that we control the loads which trigger these resistances. Hydrodynamic influences like waves, swell and current will exert fluctuating loads on the pipe and surrounding seabed. To prevent scatter effects of environmental loads during the analysis, these are not taken into account .

Secondly, the water level and seabed will be kept horizontal and plane during the research. Fluctuations and therefrom resulting gradients of the water level and seabed are outside the scope. Focus will be on a submerged situation of pipeline pull operations, as this is where most proposed curved installations are expected. Furthermore we expect this to be the normative situation due to reduced lateral resistance following from a decreased effective pipe weight. A sloping bed is avoided, since the focus is on the most basic situation.

Thirdly, the psychical tests will be executed on non-cohesive granular material since land-falls are often performed on sandy or silty seabed conditions. Rock and clay bottoms result in rough installation conditions, cover a relatively limited market-share and are therefore less of our interest than granular beds.

Fourthly, since the focus of this research is understanding the core principles of two-dimensional friction mechanisms during this research, trenches are excluded from the scope. Installation in a trench provides extra lateral resistance capacity due to the slope and a larger passive resistance providing sand mass. Initial embedment of the pipeline into the underlaying soil is a natural phenomenon during axial pull operations and is therefore inevitable to include into the scope of research.

Fifthly, effects of pull wire - seabed interaction on the pipeline loads is excluded from the research scope. Taking this interaction into account would distract from the main goal of the research: acquiring knowledge of the build-up of axial and lateral soil resistance on sliding pipelines. Besides the latter, wire pulls on the seabed are highly complicated processes that require dedicated studies themselves. Installation vessel motions are, as a result of excluding pull wire – pipeline interaction, not part of the research scope either.

Lastly, the pipe and sand specifications throughout the experiments should be scaled down correctly from real pipe specifications. By aiming for a corresponding stiffness and roughness the obtained data of the scaled physical tests will be extrapolated to full-scale.

1.4. Research question

The focus of this research is based on the sliding behaviour of a pipeline upon one specific seabed soil type and excludes dynamic environmental loads and the dynamic components of installation vessel loads. This leads to the following main research question.

To what extend can a concrete covered, submerged, steel pipeline be installed in a curved trajectory during pull operations on a plain, non-cohesive, granular seabed, in absence of environmental loads?"

1.4.1. Sub research questions

When one wants to answer the main research question, sub research questions arise. The sub research questions focus on sub effects that contribute to the complete soil structure interaction. Answers to them should provide the base for the answer to the main research question. The three most important sub research questions of this thesis are summed up down below.

What is the build-up of axial soil resistance of a submerged pipeline on a plain, non-cohesive, granular seabed, as a function of displacement?

What is the build-up of lateral soil resistance of a submerged pipeline on a plain, non-cohesive, granular seabed, as a function of displacement?

What is the influence of the stiffness of a pipeline on the trajectory of the submerged curved pull operation?

1.5. Research plan

A well-organized research plan is required to ensure the research objective can be obtained and the research questions are answered. The thesis can be distinguished by five main stages. In reality these stages will interfere and some processes will be iterative.

The five main stages are:

1. Literature study
2. Modelling
3. Physical testing
4. Validating predictions
5. Reporting and presenting outcome

1.5.1. Literature study

During the literature study it is the goal to create an overview of information that is available on the subject of research. Literature will be found on reliable sources like DNV codes, applicable books, papers from ResearchGate and internal Boskalis' lessons-learned from former projects. Since no exact research on this subject is available; this research will combine related information that contributes to the understanding of appearing phenomena in the researched subject. The literature will provide answers to the sub research questions stated in the previous section.

1.5.2. Modelling

During the modelling phase, a model will be created to compute to what extend it will be feasible to pull partially embedded pipelines into a curved trajectory. The two-dimensional soil-structure interaction (of which knowledge is acquired during the literature study) will be taken into account in the model. At the end of this phase computations can be made to (unverified) to predict the minimum pull radius of a certain pipeline on a specific sandy seabed.

1.5.3. Physical testing

Experimental data will be obtained by means of scaled physical testing of curved pipe pulling operations. The physical test data will provide a feed-back loop, which enables to verify the model predictions. During the tests it is aimed to realize a test setup that replicates pipe pulling operations as well as reasonably possible; while scatter generating effects are minimized as much as possible (more elaborately discussed in section 1.3). Design, construction and sensor installation are part of the scope of the research as well.

1.5.4. Validating predictions

After obtaining the test results the hypothesis' predictions are checked with the outcome of the physical tests. If required, discrepancies will be clarified and recommendations will be made for subsequent studies. The model computations may either be confirmed, partly confirmed or proven to be false.

1.5.5. Reporting and presenting outcome

The student will report his findings and present the outcome of his research in a graduation-presentation at Delft University of Technology.

2

Theoretical background

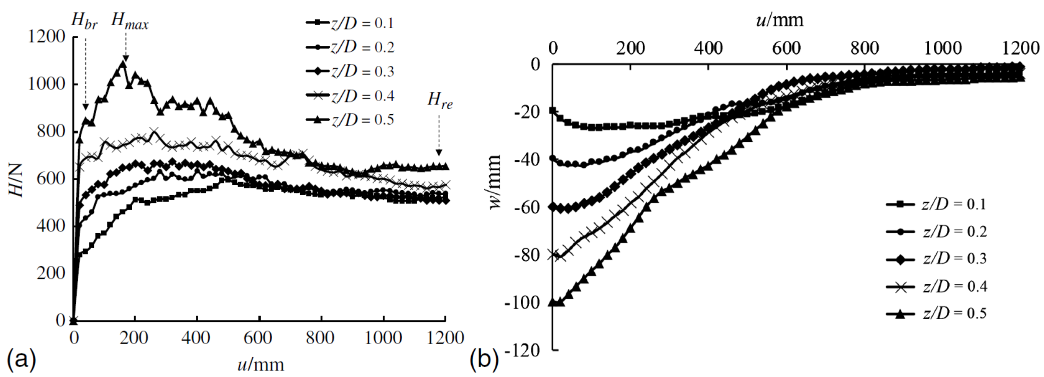

Figure 2.1: Physical test results including (a) lateral soil resistance curves and (b) pipe trajectory curves by Wang et al. (2018)

Chapter 2 provides information regarding the important physical processes that play a role within the scope of this research. In fact, it can be seen as a summary of most literature that is used within this thesis. The research questions, stated in 1.4, form the base of the subjects that are examined.

The chapter treats pipeline behaviour and characteristics, geotechnical behaviour of partially embedded pipelines and related phenomena that will play a role during future curved pipe pull operations. At the end of the chapter, a brief summary of the findings is enclosed to conclude. These findings form the base for the modelling works done during this research.

2.1. Pipeline behaviour and characteristics

The focus of this research is the soil - structure interaction between sliding pipelines and the surrounding seabed. During curved pipe pull operations, the stiffness characteristics of the pipeline is one of the two most important influences on the radii that can be obtained. Within this section, a thorough understanding of the pipeline characteristics is acquired.

Figure 2.2: Artist impression of a pipeline with concrete weight coating

2.1.1. Structural behaviour pipeline

A pipeline is build up out of two structural components, being the steel pipeline and the concrete weight coating (as can be observed in 2.2). When a pipeline is pulled into a curved trajectory, it is subjected to two main loading mechanisms. Often, the major one of the two will be the tension in the pipeline, since the pull length is generally multiple kilometers. As a result of the induced curvature, the second structural loading mechanism is bending moment. During future curved pipe pull projects, Boskalis would like to obtain bending radii in the order of multiple hundreds to thousands times the pipeline diameter. When applying such large design radii; the overall bending moment (and stresses that come along with these bending moments) in the pipeline are expected to be relatively low.

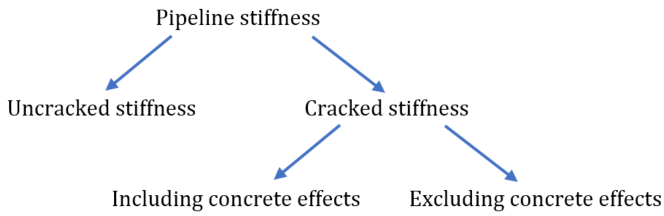

Figure 2.3: Different assumptions for pipeline stiffness modelling

The behaviour of the pipeline is influenced by the stress history of the pipeline. If, at a former stage, the concrete of the pipeline has experienced stresses that exceeded the tensile strength of the material, it will be cracked. The different methods of the bending stiffness modelling of concrete covered steel pipelines is presented in figure 2.3. During this research, a model for the uncracked and cracked pipeline is supplied. It is up to the engineer to decide which model has to be applied.

Stress and strain distributions The stress and strain distributions within a cross section of a concrete covered pipeline can be described by means of basic structural mechanics relations. For the sake of this research the influence of bending moment is presented as function of the bending radius. Equation 2.1 holds for the strain distribution over a pipeline cross-section.

$$\varepsilon(y,x,t) = \frac{1}{R(x,t))} z + \varepsilon_T(x,t) \tag{2.1}$$

In which:
$\varepsilon(y,x,t)$ = Strain of the material [%]
z = Level within cross-section from neutral axis $[m]$
$R(x,t)$ = Radius of the pipeline $[-]$
$\varepsilon_T(y,t)$ = Tension component of strain [%]

Influence of the radius of curvature and the pull tension can be extracted from the relation. From the aforementioned relation 2.1 the resulting stress distribution follows by multiplying with the local Youngs' modulus of the material. Relation 2.2 provides the stress distribution over a cross-section.

$$\sigma(y,x,t) = \frac{1}{R(x,t))} zE + \varepsilon_T(x,t)E \tag{2.2}$$

In which:
$\sigma(y,x,t)$ = Local stress in the pipeline $[N/mm^2]$

By the previous formula we can observe that the maximum steel stress appears on the outer end (outside of the bend) of the cross-section. Equation 2.3 can be used to determine the maximum stress of a pipeline subject to tension and bending:

$$\sigma_{s,max}(x,t) = \frac{1}{R(x,t))} \frac{D_s}{2} E_s + \frac{T(x,t)}{A_s} \tag{2.3}$$

This relation holds when there is no interaction between the concrete and steel. If there is collaboration between the two materials relation 2.3 underestimates the steel tension.

2.1.2. Uncracked structural response pipeline

If we assume uncracked behaviour of the pipeline, it implies that the strain at every location along the interface of the steel pipe and the concrete cover is the same. There is hundred percent bond and interaction between the steel pipeline and the concrete weight coating. This situation is displayed in figure 2.4. The neutral bending axis is vertical since the pipeline will experience horizontal bending.

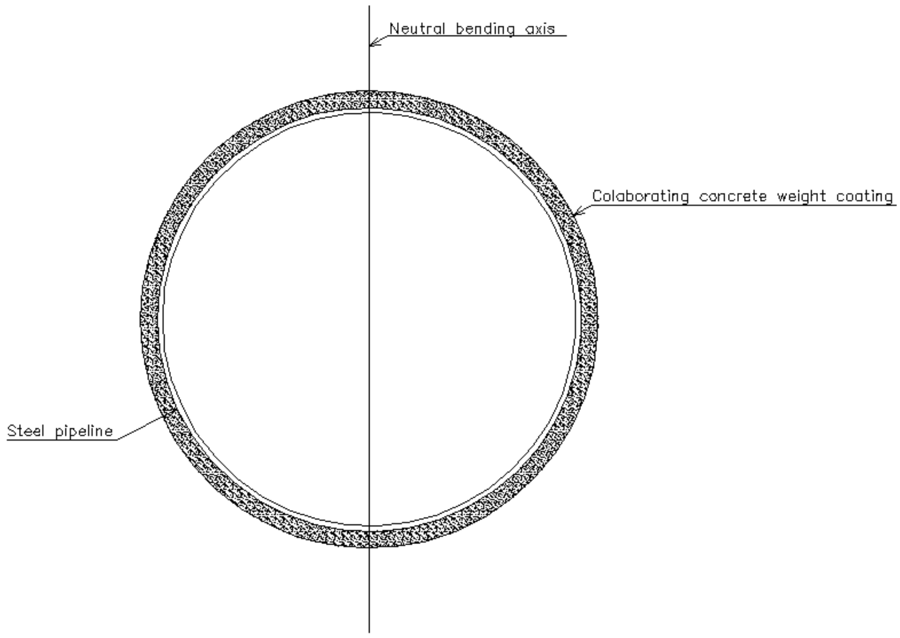

Figure 2.4: Uncracked cross-section of a concrete covered pipeline

Pure tension Under pure tension the strain of the uncracked pipeline is equal over the complete cross-section. From axial equilibrium follows that the distribution of the tensile forces under pure tension can be prescribed according the following relation.

$$T(x,t) = \varepsilon_s E_s A_s + \varepsilon_c E_c A_c \tag{2.4}$$

In which:
$T(x,t)$ = Pull tension in the pipeline $[N]$
ε_s = Strain of the steel pipeline [%]

E_s = Youngs' modulus of steel $[N/mm^2]$
A_s = Cross-sectional area of pipeline steel $[N]$
ε_c = Strain of the concrete weight coating [%]
E_c = Youngs' modulus of concrete $[N/mm^2]$
A_c = Cross-sectional area of pipeline concrete weight coating $[N]$

Tension and bending combined When pure bending is obtained the strain at the interface of concrete and steel is equal, in case of an uncracked weight coating. According to relations 2.1 and 2.2 the strain and stress distributions of an uncracked pipeline are characterized as displayed in figure 2.5.

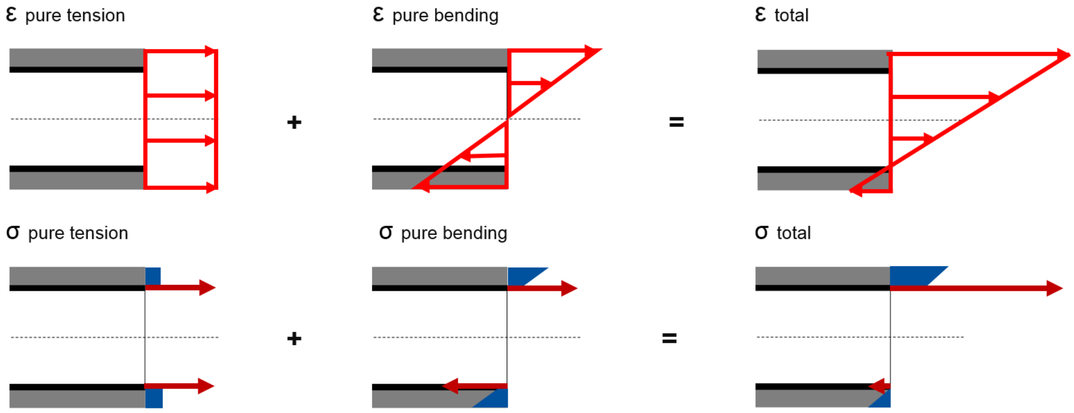

Figure 2.5: Cross-section of uncracked pipeline reaction under (l) pure tension, (m) pure bending and (c) the combination of the latter

2.1.3. Cracked structural response pipeline

During pipeline installation the maximum tensile capacity of the concrete weight coating is often exceeded. Within this subsection, the behaviour of a cracked pipeline is described. This situation is displayed in figure 2.6. As for the uncracked cross-section the neutral bending axis is vertical since the pipeline will experience horizontal bending. The neutral axis of the cracked cross-section is shifted towards the inner bend since the outer bend concrete does not contribute to the bending stiffness after cracking.

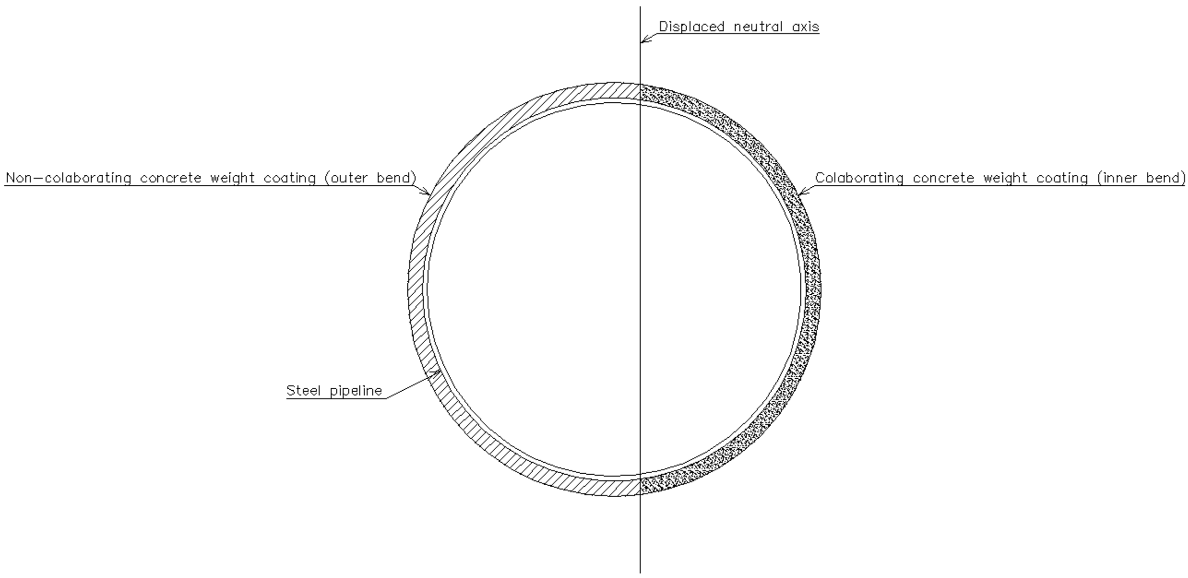

Figure 2.6: Cracked cross-section of a concrete covered pipeline

Pure tension If we assume cracked behaviour of the pipeline, the concrete cover will not contribute to the total tensile capacity anymore. Under pure tension the steel pipeline delivers all resistance. According these assumptions, the following relation holds:

$$T(x,t) = \varepsilon_s E_s A_s \tag{2.5}$$

Tension and bending combined When pure bending is obtained the concrete on the inner side of the bend contributes bending resistance. The concrete on the outer bend side of the pipeline does not contribute, since it can not resist to tensile strains after loosing her integrity. ccording to relations 2.1 and 2.2 the strain and stress distributions of an uncracked pipeline are characterized as displayed in figure 2.5.

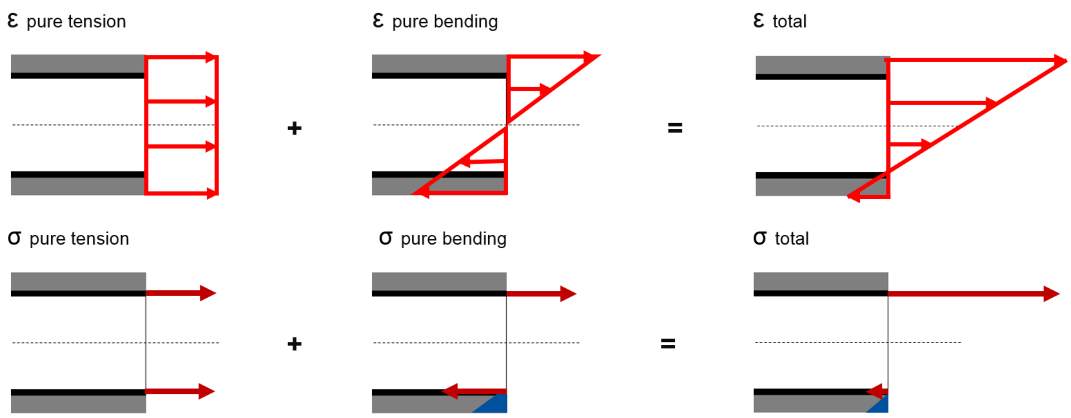

Figure 2.7: Cross-section of cracked pipeline reaction under (l) pure tension, (m) pure bending and (c) the combination of the latter

2.1.4. Structural integrity pipeline

Structural integrity of a pipeline in a pull operations is assumed to be maintained as long as the tensions within the pipeline does not exceed the maximum stress capacity of the pipeline steel. If the maximum stress of the pipeline steel is not reached, yielding will not occur.
Typically pipelines are examined on global buckling, a mechanism that might appear when a pipeline is pressurized. Since pipelines are tensioned during a pull operation, there is no risk of global buckling and no need to perform analysis' of this failure mechanism. For the final installation design a local buckling check should be performed.

2.1.5. DNV design standard pipeline

The concrete weight coating of a marine pipeline should be maintained to ensure the pipeline is safely founded on the seabed. Concrete weight coating is maintained as long as it does not crush under the influence of bending induced pressure. Concrete crushing requires a small bending radius of the pipeline to occur, it is questionable whether such radii will occur during curved pull operations.

DNVGL-ST-F101 regarding Submarine pipeline systems gives explicit guidelines to prevent crushing of the concrete weight coating during pipelay operations. For pipelay installation, concrete crushing is one of the normative fail mechanisms in pipeline design. It is highly recommended to perform the check for the final installation design of a curved pipe installation.

During a concrete crush check the compressive strain (calculated regarding relation 2.6) the concrete coating should not exceed the compressive strain capacity of the concrete. If the concrete specifications are not available, concrete crushing may be assumed to occur when the strain in the concrete (at the compressive fibre in the middle of the concrete thickness) reaches -0.2 percent.

$$\varepsilon_c(z,x,t) = \frac{1}{R(x,t))} z + \varepsilon_{c,ax}(z,x,t) \tag{2.6}$$

In which:
$\varepsilon_c(z,x,t)$ = Strain of the concrete weight coating [%]
z = Level within cross-section from neutral axis $[m]$
$R(x,t)$ = Radius of the pipeline $[-]$
A_s = Cross-sectional are of steel in the pipeline $[N]$
$\varepsilon_{c,ax}(z,x,t)$ = Strain of the concrete weight coating, caused by tension [%]

2.1.6. Structural assumptions of the industry

Since the high density concrete ($\approx 3100\ kg/m^3$) weight cover of the pipeline is primarily added to provide extra on-bottom stability of the pipeline, the minor structural contribution of this concrete shell is often neglected. When a pipeline is installed by means of a pipelay vessel, it curves during her way towards the seabed. During this installation, small bending radii can appear. These small bending radii result in large stresses and strains. Large stresses and strains can lead to cracks in the concrete weight coating, which is the reason the structural contribution of this layer is often neglected. Extra stiffness and strength can be assumed positive during this installation method.

If the pressure in the concrete coating becomes too large, the concrete will crush and might loose contact with the pipeline. When the concrete crushes and breaks from the pipeline, it naturally does not contribute to the pipe stiffness anymore. The radii at which the concrete crushes are usually in the order of hundreds of times the outer pipe diameter, radii which we do not expect to be able to reach during submerged curved pipe pull operations. Due to the latter argument, we assume crushed concrete covers do not appear during curved pipe pull installation.

Although concrete crushing is an excluded effect; concrete cracking, which takes place at lower strains, appears if the maximum concrete tensile strength is exceeded. When the concrete shell is cracked, it cannot resist tensile forces anymore. Concrete lacks the ability to resist high tensile strains, but it is known for its resistance against pressure. It should be mentioned that a concrete cover, even though it might be cracked, will still contribute to the bending stiffness of a pipeline when pressurized. If the concrete cover is neglected during computations of a curved pipe pull, the stiffness of the pipe is underestimated and the predicted minimum pull radius will be under-estimated as well. During future projects this might ultimately lead to design pull radii that cannot be obtained in practice. In contrast to pipelay installation of offshore pipelines, unexpected extra stiffness might initiate a problem during curved pull installations.

2.2. Geotechnical behaviour of partially embedded pipelines

To compute well-defined predictions of the ability to pull pipelines into curved trajectories on sandy seabeds, it is of major importance to understand the behaviour of sand surrounding the partially embedded pipeline. During this research, pipelines between zero and fifty percent embedment are examined, since these are the embedments that are observed in former pipe pull operations. Within this section the behaviour of sandy seabeds during pipe movement is described.

2.2.1. Axial pipeline - seabed interaction

The axial resistance of the pipeline is determined by the friction between the pipeline and the sand. The specifications of these two determine the amount of axial resistance that occurs. Pipe weight, roughness of the concrete weight cover and the internal friction angle of the seabed are the main parameters that play a role. Due to the often limited amount of pull force, pipelines are equipped with buoyancy modules, to reduce the pull force required to obtain axial sliding of the pipeline.

When assessing axial friction of partially embedded piplines, there is a distinction between static friction and kinetic friction. The static friction that has to be overcome to set the pipeline into axial motion is called the axial breakout resistance. During the following paragraphs an overview of an existing applicable relation and experience is presented.

Coulomb friction The simplest way to describe the maximum magnitude of friction between a subject and a granular material is by means of the Coulomb friction method. If the underlying material is cohesive, the effect of cohesion is added to the Coulomb friction. Since this research focuses on sandy seabeds with negligible cohesive properties, cohesion is neglected. The formula of Coulomb friction is stated in equation 2.7.

$$F_f = \mu\, W = \tan(\phi) W \tag{2.7}$$

In which:
F_f = Friction force $[N]$
μ = Friction factor $[-]$
W = Weight of the pipeline $[N]$
ϕ = Internal friction angle of the granular material $[°]$

Former project pipeline pull data By examining two pipe pull projects of Boskalis, the applied friction factor μ within this research is validated. The friction factor follows from the former project data logs and corresponds to the Coulomb relation for an internal friction angle of sand ($\phi \approx 31$ degrees). In table 2.1 the applicable factors for submerged and dry conditions can be observed for pipelines.

Material	μ_{WET}	μ_{DRY}
Pipeline - sandy seabed	0.6	0.6

Table 2.1: Mean friction factors former projects

As aforementioned in the start of this subsection: the startup force of a pull operation is often higher than the running force of a sliding pipeline. During a pipe pull operations Boskalis often observes a high breakout tension, after which there is a drop of tension. Pull records of a 24” and 48” subsea pipe pull operation show breakout forces conform the proposed friction factors in table 2.1. Running forces drop soon after the break-out of the pipeline, to a fraction of the latter. Throughout this research, the friction factors of table 2.1 will be applied to determine axial friction of examined pipelines.

2.2.2. Lateral pipeline - seabed interaction

Although the bearing capacity of subsea pipelines is a primary input parameters for many design calculations, most of these calculations focus on the on-bottom stability and global buckling management. Therefore the known lateral resistance relations apply on either static or large lateral movement situations of subsea pipelines. This research is concerned with the buildup of the drained bearing capacity of a subsea pipeline that is subject to vertical and horizontal loading. The different phases of a lateral displaced partially embedded pipeline are displayed in figure 2.8. Few studies have been performed on minor lateral displacement of pipelines and above all not on sandy soils. Within this section the examined studies concerning this subject are prescribed.

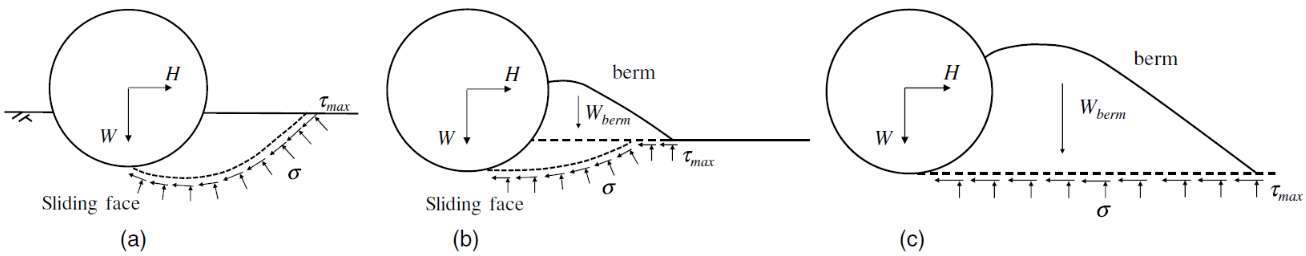

Figure 2.8: Mechanism of soil resistance response under different stages: (a) breakout stage, (b) unstable movement stage and (c) residual stage

Origin of former lateral pipeline - seabed interaction studies If the seabed around a pipeline has insufficient bearing capacity to resist externally-applied environmental or installation loads; significant movements may occur, jeopardizing the integrity of the pipeline. Accurate assessment of the available resistance can lead to significant cost savings in capital expenses for offshore projects if pipeline stabilization measures can be optimized. Besides expansion as a result of high temperature and pressure, oil and gas pipelines also undergo operational expansions during start-up and shutdown cycles, which must be safely accommodated to prevent pipeline damage. Global buckling design is particularly complicated because the geotechnical resistance must be modeled: a conservative design may rely on either an upper or lower estimate depending on the context.

Drained geotechnical response
Pipeline bearing capacity is further complicated by the fact that either drained or undrained (or intermediate, partially drained) conditions can prevail during breakout. Drainage conditions depend on the consolidation properties of the soil, the rate and duration of loading and the embedment condition of the pipeline. Drainage affects both the shear strength of the soil as well as the kinematics at failure.

During undrained loading volume change does not occur and associated flow conditions prevail at failure. Under drained conditions volume change may occur at failure and the soil strength is controlled by friction. For drained failure the mobilized shear strength varies throughout the failure mechanism, and the resulting kinematics are complicated by the occurrence of volumetric strains due to non-associated flow.

Since this research concerns permeable sand and the lateral velocities (and associated accelerations) of the pipeline will be relatively small during pull operations: this research is based on a drained geotechnical response.

Verley and Sotberg (1994)
The current understanding of drained pipeline bearing capacity is based primarily on experimental studies. Verley and Sotberg (1994) summarized three datasets from full scale testing on silica sands and proposed a power law relationship to calculate the peak breakout resistance, which is a function of the applied vertical load and the pipeline embedment. Relation 2.8 is widely used and adapted by the DNV.

$$F_{L,brk,d} = 0.6V + F_p \tag{2.8}$$

In which:

$$F_p = \gamma' D^2 (5 - \frac{0.15\gamma' D^2}{V})(z/D)^{1.25} \qquad for\ \frac{V}{\gamma' D^2} \geq 0.05 \tag{2.9}$$

$$F_p = 2\gamma' D^2 (z/D)^{1.25} \qquad for\ \frac{V}{\gamma' D^2} < 0.05 \tag{2.10}$$

And:
$F_{L,brk,d}$ = Lateral force at breakout in drained soil conditions $[N/m]$
V = Vertical pipe-soil force per unit length $[N/m]$
F_p = Passive soil resistance $[N]$
γ' = Effective soil unit weight $[N/m^3]$
z/D = Normalized pipeline embedment $[-]$
z = Embedment (measured from original seabed level) $[m]$
D = Diameter pipeline $[m]$

This method was based on tests conducted for embedments less than 35 percent of the pipeline diameter and no data was provided regarding the friction angle or other strength characteristics of the materials tested. Since the relation of Verley and Sotberg (1994) is adapted by the DNV design code, relation 2.8 probably underestimates the actual drained lateral soil resistance. Summing the latter with the fact that DNV is globally applied throughout the offshore industry, the relation is an attractive base for this research. One can observe two terms within relation 2.8: the Coulomb friction term and the passive resistance term.

Wang et al. (2018)
To gain a broader proof of the relations of Verley and Sotberg (1994), the research of Wang et al. (2018) is used. Wang et al. (2018) conducted a research concerning the buildup of drained lateral soil resistance for small lateral pipeline displacement, based on unsaturated experiments. An illustration of the test setup of the research can be observed in figure 2.9. The study provides important physical data for this research, since it is the only found source containing detailed physical test data of drained lateral soil resistance of partially embedded pipelines in sand. Within this research, the relations of Verley and Sotberg (1994) are verified by the Wang et al. (2018) data, before being used for modeling purposes.

During the physical tests of Wang et al (2018), 200mm pipelines (varying in weight and initial embedment) were displaced in lateral direction. The pipeline section was not constraint for vertical movement. Along a forced lateral breakout the lateral forces were logged, as well as the displacement in vertical and lateral direction. Magnitude of lateral displacement during an experiment was either 0.5D or 6D.

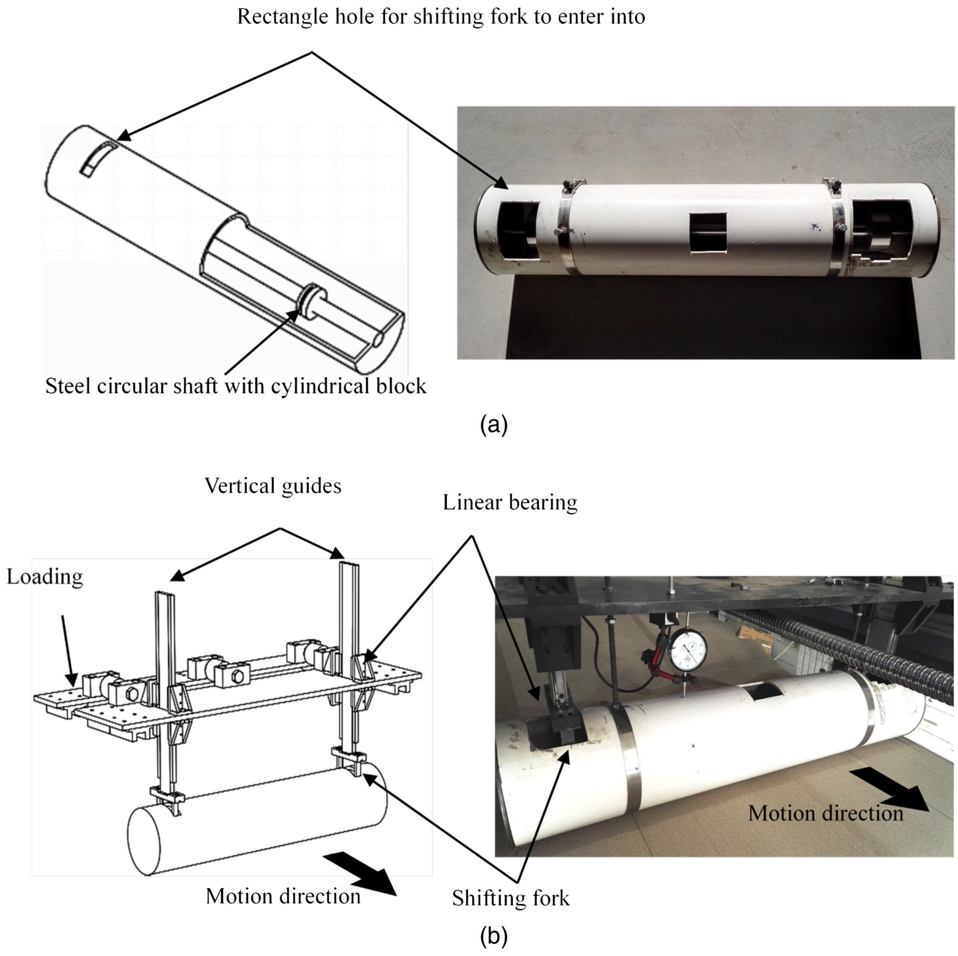

Figure 2.9: Physical test setup of Wang et al (2018)

After determining the breakout forces of the experiments and analyzing the comparison with five different relations, Wang et al. concluded that the DNV adopted relation 2.8 of Verley and Sotberg (1994) with the first passive resistance term gave the best fit with the obtained data. In figure 2.10 one can observe lateral soil resistance curves concerning multiple embedments of one test model and the accompanying comparison of different breakout relations.

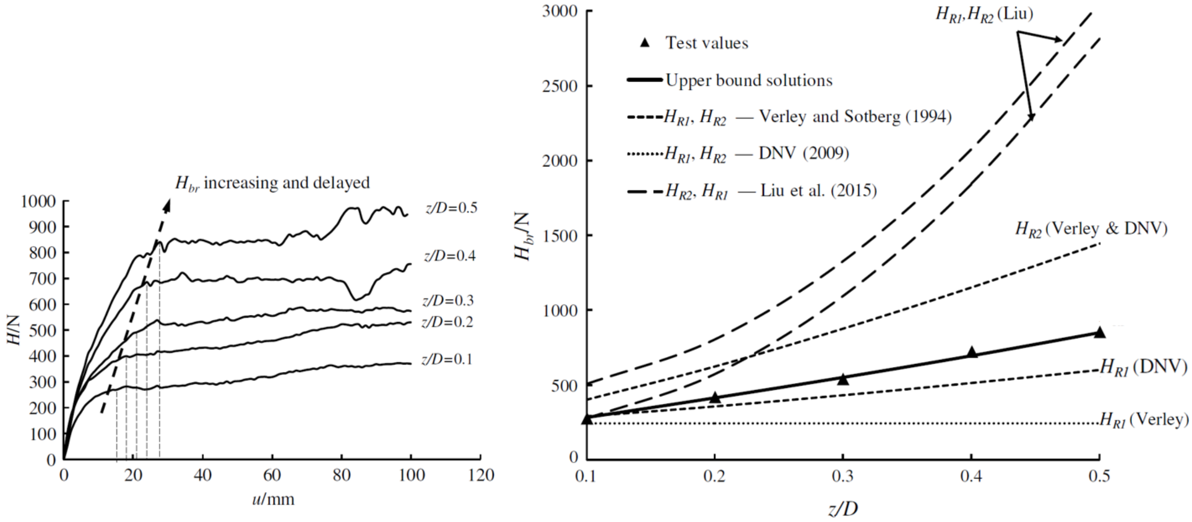

Figure 2.10: (l) Resistance curves of laterally displaced pipelines (D_0=200mm, L=1000mm and W=402N) and the (r) related comparison of this physical test data with five different relations

From these comparisons we can learn that the DNV adopted Verley and Sotberg (1994) relation (denoted as H_{R1}(DNV)) slightly underestimates the maximum lateral breakout capacity of the partially embedded pipeline: as was expected in the previous paragraph. H_{R2}(Verley & DNV) is not defined clearly within the available paper and H_{R1}(Verley) is equal to the friction part of relation 2.8.
After this verification, the relations of Verley and Sotberg (1994) are assessed to be applicable for the modelling of maximum breakout resistances of partially embedded pipelines.

Final lateral soil resistance model

Now the applicable relation for the maximum lateral soil resistance is set, the buildup of resistance towards this maximum value has to be determined. The experimental data of Wang et al. (2018) provides detailed info regarding the parameters and processes that play a role in the buildup of lateral resistance.

The buildup of lateral resistance can be prescribe prescribed as a relation of lateral pipe displacement. The typical shape of the drained response resistance curves of laterally displaced can be found in figure 2.10. During the lateral motion, the pipeline builds up resistance until the breakout resistance is reached. An example of the inititation of breakout is shown in 2.11.

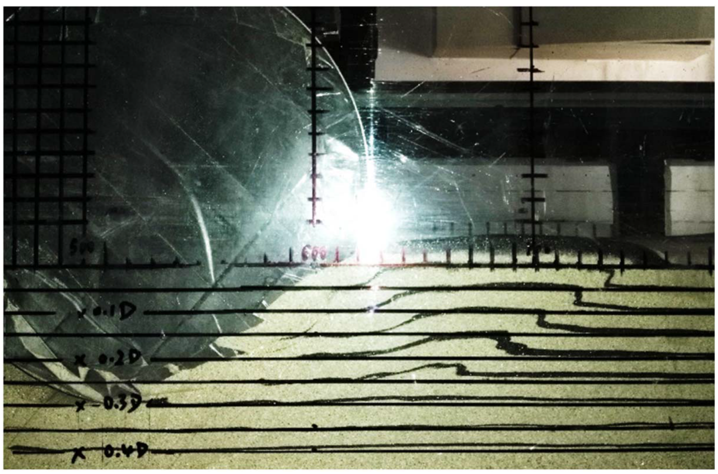

Figure 2.11: Breakout of the 200mm model pipeline (z/D=0.3) of Wang et al. (2018)

Hereafter the plowed heap of sand is pushed across the seabed, a process called bulldozing. During the bulldozing phase and for a drained response of the seabed, the resistance stabilizes. Since the pipeline now requires less energy to propagate an extra unit length, this behaviour is described as "softening" of the soil response. As aforementioned, it requires a certain displacement to buildup to the breakout force. This lateral mobilization distance of the breakout resistance is prescribed in the DNVGL-RP-F114 (2017) and displayed in figure 2.12. The different uncertainty cases of the DNV are checked with the experimental data of Wang et al. (2018). From this analysis it was concluded that the "best estimate" lateral mobilization distance delivered the best fit to the experimental breakout data of Wang et al. (2018). Therefore the best estimate is chosen as the lateral mobilization distance.

Parameter	*Uncertainty case*	*Typical values*[3]
y_{brk}	Low estimate, LE[1]	$\frac{y_{brk}}{D} = 0.004 + 0.02 \cdot \frac{z}{D}$
	Best estimate, BE[2]	$\frac{y_{brk}}{D} = 0.02 + 0.25 \cdot \frac{z}{D}$
	High estimate, HE[2]	$\frac{y_{brk}}{D} = 0.1 + 0.7 \cdot \frac{z}{D}$

Notes:
1) The low estimate is a minimum value which considers the model test results from statically embedded pipe data
2) The best and high estimates consider statically and dynamically embedded model test data
3) All values represent a secant fit to the displacement when $F_{L,brk}$ is fully mobilized. No distinction is made between drained and undrained behaviour.

Figure 2.12: Lateral mobilization distance to breakout resistance by DNVGL-RP-F114 (2017)

Softening drained lateral soil resistance can be prescribed by means of a tangent hyperbolic relation. An example can be found in the DNVGL-RP-C212 (2017) design standard for "Offshore soil mechanics and geotechnical engineering" in which the lateral soil reaction on foundation piles is prescribed. Since the lateral soil resistance of partially embedded pipelines has a tangent hyperbolic shaped development, this character is adopted into our lateral soil model. Verley and Sotberg (1994) relations supply the restricting maximum of the resistance, while the lateral mobilization displacement provides the distance at which the resistance should have reached the maximum. We assume Verley and Sotberg (1994) relations capture the influence of light and heavy pipe behaviour, since it represented both light and heavy pipe behaviour well in the experiments of Wang et al. (2018).

The resulting P(Y) model can be prescribed regarding the following relation:

$$P(Y) = F_{L,brk,d}\, tanh(C_Y * Y) \tag{2.11}$$

In which:

$$C_Y = \frac{1 + 5\frac{z}{D}}{Y_{brk}} \tag{2.12}$$

And:
$P(Y)$ = Lateral soil pressure per unit length $[N/m]$
$F_{L,brk,d}$ = Lateral force at breakout in drained soil conditions $[N]$
C_Y = Embedment coefficient $[m^{-1}]$
Y_{brk} = Lateral mobilization distance to breakout resistance (best estimate) $[m]$

The P(Y) model prescribes a theoretical buildup of lateral soil pressure as a function of lateral pipeline displacement. Embedment coefficient C_Y is initiated to capture the stiffening effect of embedment on the P(Y) curves, the coefficient is based on a curve fit of the experimental data of Wang et al. (2018). An example of this curve fit can be observed in figure 2.13.
Throughout the modelling section of this research (treated in chapter 5) the P(Y) model is used to incorporate the lateral soil reaction on partially embedded pipelines.

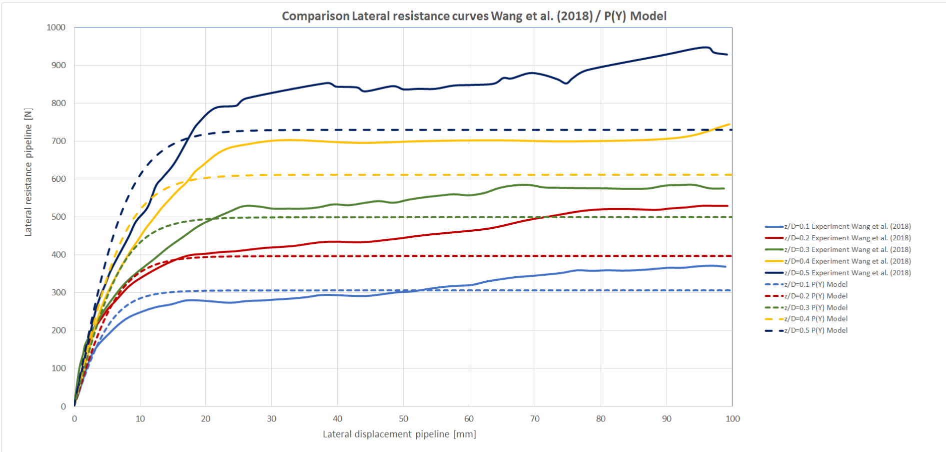

Figure 2.13: Comparison of the resistance curves of different embedded model pipelines (D_0=200mm, L=1000mm and W=402N) from Wang et al. (2008) and the proposed P(Y) model

2.3. Related phenomena

Throughout this research multiple phenomena are encountered that will appear and influence curved pipe pull operations. Within this section, three of these phenomena are described. The numerical model developed during this research does not take these phenomena into account, since it focuses on the core of the knowledge gap that is faced.

2.3.1. Creating pipeline embedment

During the axial pull of a pipeline, the pipeline tends to create more embedment as it propagates across the sandy seabed. Typical embedments of pulled pipelines are between 10 and 50 percent, but there are even examples of pipelines being pulled through submerged sand heaps.
The submerged pipe weight, compaction of the seabed and pull head are factors that have a large influence on the embedment that is reached. In figure 2.14 the prescribed digging behaviour can be examined by means of a 3D survey image.

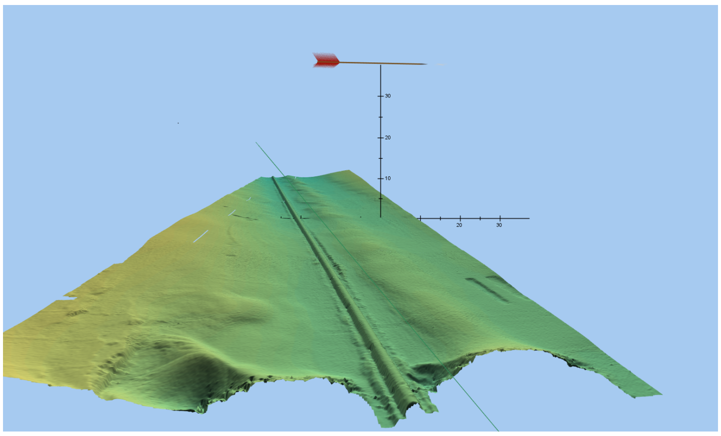

Figure 2.14: Digging behaviour of 48” pipeline pulled in trench

2.3.2. Light and heavy pipeline behaviour

During a lateral breakout, soil is plowed as a result of displacement of the pipeline. The amount of plowed soil has a strong effect on the subsequent pipe-soil interaction response. After the breakout this plowed sand berm, combined with the Coulomb friction of the pipeline, delivers the residual lateral resistance of the pipeline. The volume of plowed sand is dependent on the lateral pipe path that appears during the breakout. Wang et al. concluded that initial embedment and effective weight of the pipeline play a large role in the observed lateral breakout paths. Figure 2.15 shows the propagation angle of the different model pipes during lateral breakout.

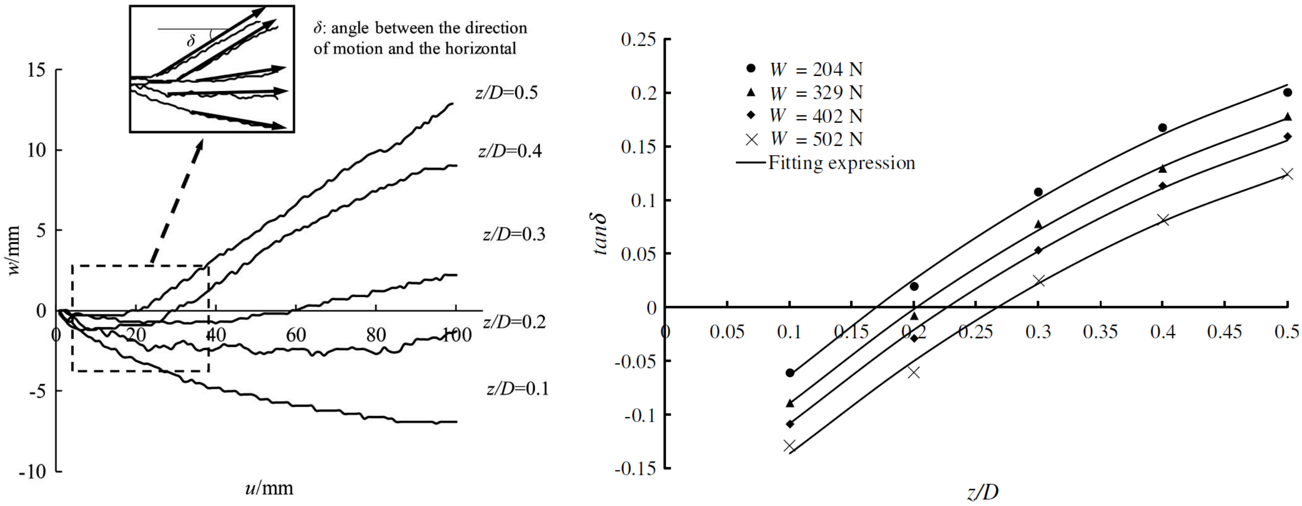

Figure 2.15: Light and heavy pipe response during the breakout phase of experiments Wang et al. (2018)

The dependency of lateral pipe paths can be summarized as follows: shallow embedded pipelines tend to propagate downwards and deeper embedded pipelines tend to propagate upwards during a lateral breakout. Subsea pipelines have a relatively low submerged density and are therefore expected to come up to seabed level again. Heavier pipelines plow more soil than lighter pipelines, since they reach larger depths and take more lateral displacement to come up to seabed level again.

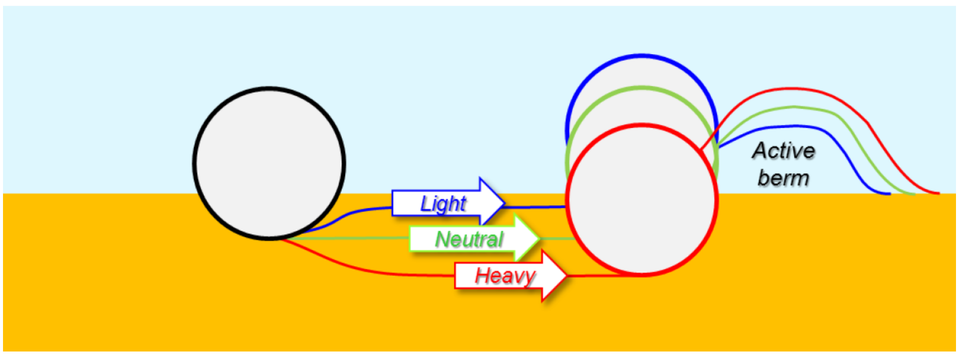

Figure 2.16: Light and heavy pipe response according Bruton et al. (2006)

The aforementioned mechanisms can be connected by the ”light pipe” and ”heavy pipe” responses presented by Bruton et al. (2006). Light pipe response is defined as the pipe exhibits upward motion when a breakout occurs. In contrast, the pipeline will plow into a deeper embedment in the heavy-pipe response. Light and heavy pipe behaviour are illustrated in figure 2.16

2.3.3. Caterpillar behaviour

As can be read in section 2.2.1, it takes (relatively small) axial movement of the pipeline to propagate from the static friction phase into kinetic friction phase. At the start of a straight pipe pull operation, the pipeline is positioned statically on the seabed until the applied pull force on the pipe exceeds the complete breakout friction of the pipeline. When the complete pipeline is propagating in axial direction with a constant velocity; the entire pipeline is subject to a, more or less, normally distributed kinetic friction force.

Between the latter two described situations, of complete statics and constant propagation of the pipeline, we encounter another phase of the pull process. The projects within the scope of this research involve pipelines up to a length of multiple kilometers. Although the percentage of strain of a pipeline is relatively small, the combination of the applied pull force and enormous lengths of the considered pipelines result in an elongation that can be substantial (in the order of meters). This implies that (in an extreme case), although the pull head side of the pipeline might already be propagating at a constant velocity, the back of the pipe is still building op friction to overcome the breakout force.

A process like prescribed in the former paragraph creates axial dynamic shock waves through the complete pipeline. These shock-waves create axial velocity differences over the pipeline; causing the pipeline to propagate with a 'caterpillar' like movement. Under particular circumstances this can lead to a stop-and-go propagation of the complete pipeline. It happened during the experiments of this project, which was visible in the pull datalog as displayed by an example in figure 2.17. Please note that the horizontal axes does not start at zero and is zoomed in, to ease analyzing.

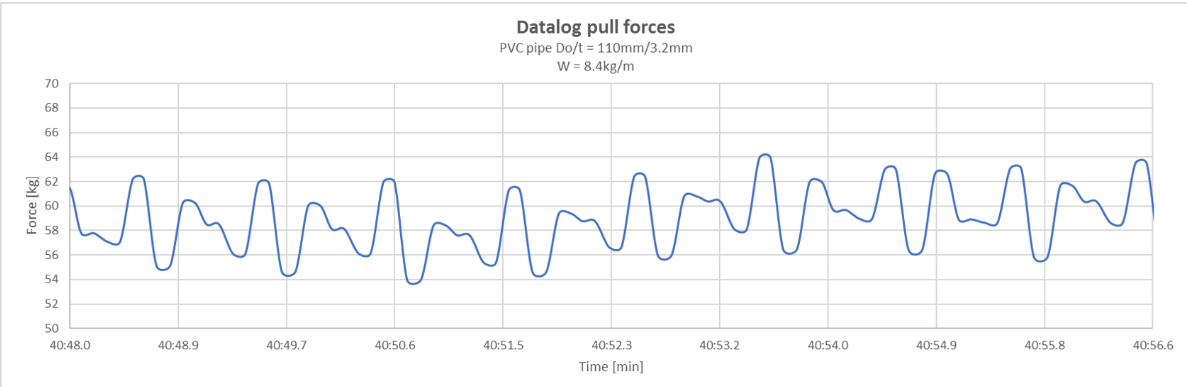

Figure 2.17: Datalog of pull tension showing caterpillar behaviour of the D_o=110mm model pipeline

Caterpillar behaviour of propagating pipelines is an interesting phenomena that may influence the capabilities to pull pipelines into curved trajectories. Since the prescribed caterpillar behaviour of pipelines is a highly dynamic process of which the influence to the scope is estimated relatively small, the phenomena is not analyzed any further within this research.

2.4. Summary of theoretical background

The previous sections of this chapter where devoted to the existing theory describing the influence of the pipeline, seabed and known phenomena of pipe movements in both axial and lateral direction. This theory forms the base for the modelling works of this research.

Pipeline behaviour Section 2.1 regarding pipeline behaviour describes how pipeline stiffness is determined. A distinction is made between the uncracked an cracked behaviour of the pipeline. Besides the latter, the relations that hold for internal pipeline tensions and pipeline integrity are prescribed. DNVGL-ST-F101 provides the limits of structural integrity for pipeline curvature.

From this section can be concluded that the loading history of the pipeline has an influence on the behaviour of the pipeline throughout the complete pipe pull operation. During future curved pipe pull operations these influences should be studied extensively since they will influence the feasibility of the installation procedure. Throughout this research the pipeline is assumed constant over length.

Geotechnical behaviour of partially embedded pipelines In section 2.2 the influence of the sandy seabed surrounding a partially embedded pipeline is described. The axial resistance is examined by means of the Coulomb friction relation.

The lateral pipeline resistance is examined more extensively. By combining researches of Verley and Sotberg (1994) and Wang (2018), a lateral non-linear P(Y) model is obtained to model the lateral resistance of partially embedded pipelines on sandy seabeds.

Related phenomena Throughout section 2.3 three phenomena that influence curved pipe pull operations are discussed. Since this study has an exploring purpose, it focuses on the core of the knowledge gap and neglects most effects of the phenomena mentioned in 2.3.

3
Physical test setup

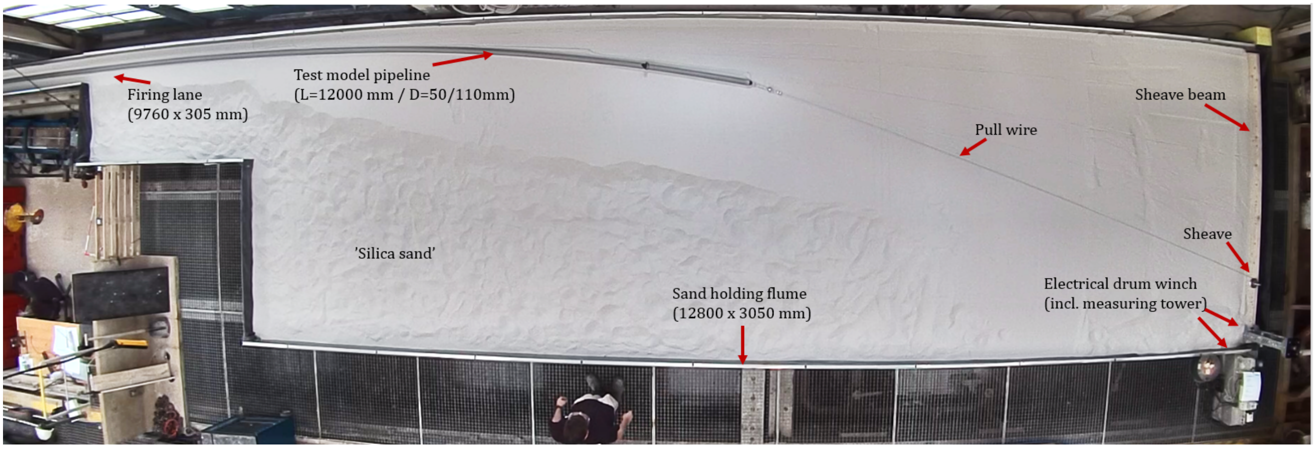

Figure 3.1: Overview of the unique physical test setup of this research

Chapter 3 provides information regarding the design of the physical test setup. The refence between the setup and the underlying theory is exposed.
The chapter treats the different components of the setup, refers to the theory that founds the setup design and describes how the model pipelines are scaled. At the end of the chapter, a brief summary of the findings is enclosed to conclude.

3.1. Setup explanation

The different components of the unique physical test setup are described within this section. An overview of the component locations can be found in figure 3.1.

3.1.1. Pipeline test models

Throughout section 3.3.2 the properties and scaling behaviour of the model pipelines are discussed extensively. Where five specific model pipelines were tested, these were three actual pipelines of which one (D_o= 50mm and t= 3.2mm) was tested with three different ballast quantities.

Pipeline - pull wire connections Pull head designs come in different shapes. The pull head design of the test models is a conical shaped, wooden plug which is connected to the pull wire by means of a steel connector. Efforts were made to create pull heads that were as symmetrical as reasonably possible. At the back of the pipe there is a comparable pipe-end which is cylindrical.

By means of the following two figures 3.2 and 3.3, one can compare an example of a real pull head with that of one of the model pipelines.

Figure 3.2: Pull head of 48' pipeline

Figure 3.3: Pull head of the D_o=50mm and t=1.8mm test model during an experiment

Bending stiffness Before physical model tests were conducted, the pipe models were examined on bending stiffness. First, the cross-sectional dimensions of the pipes were measured. No significant discrepancies of the pipe dimensions were observed.
Second, the Young's modulus was verified by means of a simply supported bend test. No significant discrepancies of the Young's modulus were observed. A photograph of this test is displayed in figure 3.4.

Since PVC is known for its creep behaviour, this was examined as well. Creep can cause plastic deformation of the model pipelines, which is a highly undesired effect during the experiments. Emperical relations, like Maxwell and Kelvin-Voigt, describe the behaviour of the material under the influence of stress, loading time and temperature. According to Van der Vegt (1991) large creep influences appear when PVC is loaded under high stresses and/or for a time frame more than multiple hours. Since the stresses in our models pipes (due to the mild pull forces and mild curves) were only a minor fraction of the maximum capacity of PVC and the time frame of an experiment was in the order of 20-30 minutes, creep effects are assumed to be negligible for the experiments conducted within this research.

Figure 3.4: D_o=50mm and t=1.8mm test model during a bend test

The typical load duration of the bend tests was approximately 20-30 minutes, corresponding to the order of time that the pipelines experience loads and deflection throughout experiments. An additional twenty-four hours creep test was performed prior to the experiments, to ensure the feasibility of the use of PVC model pipes. Results of the creep test are shown in figure 3.5. The bending tests and creep tests confirmed the assumption of negligible influence of creep for short term loading at the stress levels that appear during the experiments. Throughout the testing phase, no plastic deformation of the model pipelines was observed during short term loading. After the long term creep test a fraction of approximately 10% of the deformation was plastic.

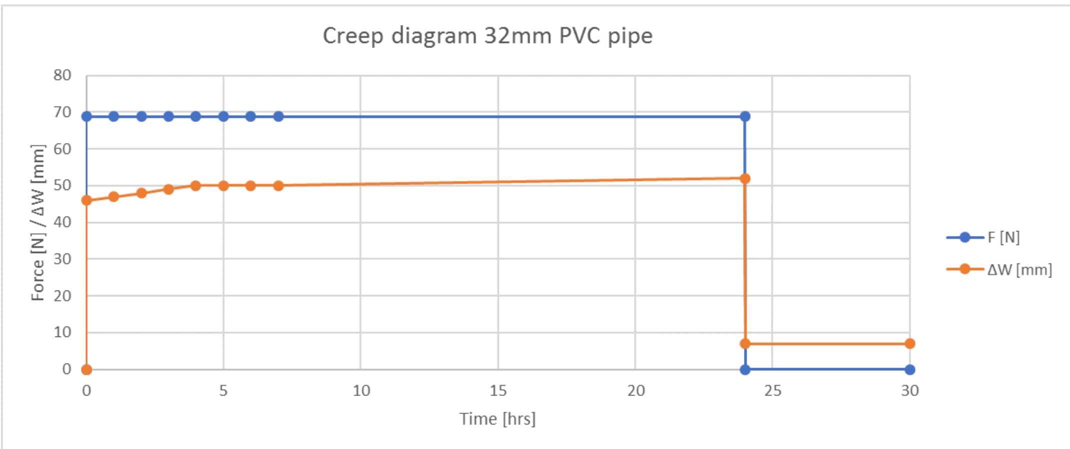

Figure 3.5: 24 hours creep test results

In between the physical experiments, the model pipelines were stored in a straight position to minimize the risk of creep. Throughout the complete test campaign, no actual creep of the models was visibly identified.

3.1.2. Pull wire

During all conducted experiments, the same pull wire was used. The pull wire is constructed from a plane 2.5 mm steel cable with a cotton wire core. The cable is flexible and the weight is negligible (approximately 0.02 kg/m).

The model pull wire does not scale with the pull wires used in pipe pull operations, as the diameter is too small and the specific weight is too low. Actual pull wire diameters are in the order of 100mm and they can way up to approximately 100 kg/m. According the applicable scales within the conducted experiments, the target wire diameters would be 8mm (λ=11.8) and 19mm (λ=5.3). As a result of the non scaling wire diameter it is hard to scale the weight of the wire in an appropriate way. Since this research focuses on pipe-seabed interaction and excludes pull-wire seabed interaction, the relatively low pull wire weight has a positive side effect.

3.1.3. Sand holding flume

The sand holding flume is constructed out of high quality wood that is normally used for concrete form work purposes. It consists of a firing lane, being a section with a small width, and a wider section where the model pipelines are pulled into a curved trajectory. Total length of the flume is approximately 23 meters and the maximum width of 3.05 meters. Height of the upstanding boundary is 400mm.

Figure 3.6: Top view of the large part of the test setup, including the sand holding flume

A PVC pond foil ensures the sand and water tightness of the flume. It is connected to the flume by means of a leveling rails, that provides guiding to the leveling devices (prescribed in section 3.1.8).
Sand properties are prescribed in the previous section. A total amount of 12 metric tons of S80 silica sand is applied in the flume. The desired sand layer thickness after leveling is 250mm. This value is determined based on the influence depth of the bearing behaviour a the 50 percent embedded 110mm pipe in sand, as prescribed in section 3.2.1.

3.1.4. Pull mechanism

Model pipelines are pulled by means of an electrical drum winch. By means of an electrical frequency drive, the pull velocity can be regulated to the desired value ($\approx$ 2 cm/s). Multiple pulleys direct the pull wire from the drum into the flume.

Figure 3.7: Electrical drum winch including frequency drive and measuring tower, located on the sheave beam side of the flume

3.1.5. Sheave beam

The sheave beam enables to create the desired angle between the pull wire and pipeline. It consists of a perforated wooden beam and a steel sheave that is relocatable by means of the sheave axis. The sheaves consist bearing and provide a smooth guidance of the pull wire.

3.1.6. Back-hold tension mechanism

A back-hold tension supplying winch is installed to provide pre-tensioning to the pipeline end, which represents extra pipe length at the back of the pipe. It is constructed by means of a winch with a purpose-made slipping steel drum, situated on the end of the firing lane.

3.1.7. Pull data logging

Both winches are equipped with a data logging system to log the pull forces that they apply to the system.

Measuring tower At the pull winch side of the system the pull tension is measured by means of a purpose-made measuring tower, visible in figure 3.7. The load cell measures (twice) the load that is applied to the pull wire via a pulley, after which the wire continuous towards the pipe head.

Measuring bar The measuring bar is situated at the back-hold winch side of the firing lane, shown in 3.8, and measures the back-hold tension according the same as the measuring tower. After passing the load-measuring bar the wire continues towards the pipe-end via a pulley.

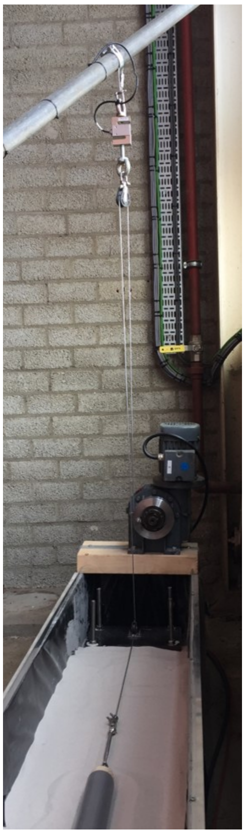

Figure 3.8: Back-hold tension mechanism including load measuring bar, located at the end of the firing lane

3.1.8. Leveling devices

Three different leveling devices are constructed to obtain a leveled sand bed in the flume. Although seabeds had a wide variety of bed ripples and dunes, a smooth leveled bed is required to validate the numerical model of this research.

Figure 3.9: (l) Largest of the three level tools during first test and (r) sheave beam including steel sheave

Leveling devices of the setup are build from wood and have a steel support frame equipped with four wheels. They level the sand while propagating along the guiding reels, pulled by the pull winch.

3.2. Reference to the theory

The main goal during the design phase of the test setup was to achieve a test setup that enabled to perform experiments that resembled full-scale curved pipe pull operations as well as reasonably possible. The physical tests should also enable to validate the numerical model computations. By doing so, it should be able to verify the feasibility of the adapted pull-out method. Testing the actual proposed curved pipe pull operations via a scaled down adapted pull-out method is the only correct manner to study the behaviour of a pipeline during such an installation. In order to validate the created numerical model in a correct manner, a range of 5 different test models are used throughout the experiments. The actual models are prescribed within the next section 3.3. Besides the test model pipelines, the sand is discussed within that section.

3.2.1. Flume dimensions

After the test models where determined, the required dimensions of the sand holding flume could be determined. The following facts determined the final dimensions of the flume.

Predicted pull radii Numerical model computations predicted pull radii in the order of 25-80 meters, for pipeline models of scale 1/5.3 and 1/11.8. Since it was required to obtain a decent size curve and apply sufficient lateral force to the pull head (which related to the sheave beam length), this was the normative design criterion.

Firing lane As for real pull-out operations, a firing lane should be provided in order to create a storing location from which the test models can be pulled into the flume.

No significant deflection at pipeline end Deflection of the pipe end (opposite side of the pull head) during the physical test is an unwanted effect. During real curved pipe pull operations there would be an extra amount of pipeline dragged along behind the curve, providing extra bending resistance. If the pipe end deflects during a curved pull experiment, it misses the bending resistance that in reality would be provided by the pipeline on the pipe end side of the pipeline.

Influence width seabed surrounding pipeline The influence width of the passive wedges that occur next to the pipe are quantified. The main wedge that should not be influenced by the flume boundaries is the passive wedge on the inner side of the pull curve. At other locations along the pipeline the influence of flume boundaries should be kept as minimum as reasonably possible.
Backhausen and Van der Stoel (2014) give estimates of the influence width surrounding foundations, depending on the ratio between the vertical and pipe horizontal loads and the internal friction angle of the surrounding soil. The influence width of the test model pipelines in this setup is estimated in the range of approximately 2D (H/V=1) to 6D (H/V=0). Implying that once horizontal loads increase the influence width decreases.

Influence depth seabed surrounding pipeline The influence depth of the failure zones that occur underneath the partially embedded model test pipeline are quantified. Influence depth should be determined from the embedment depth of the pipeline. Although the vertical bearing capacity of the surrounding seabed is not the most important parameter within this research, the influence of the horizontal flume boundary (flume bottom) should be kept as minimum as reasonably possible.
Backhausen and Van der Stoel (2014) give estimates of the influence depth underneath foundations, depending on the ratio between the vertical and pipe horizontal loads and the internal friction angle of the surrounding soil. The influence depth of the test model pipelines in this setup is estimated in the range of approximately 0.5D (H/V=1) to 2D (H/V=0). Implying that once horizontal loads increase the influence depth decreases.

Boskalis' in-house HydroLab dimensions The test setup should be build within the Boskalis' in-house test facility HydroLab.

3.3. Scaling

Physical tests relate to reality by means of certain scaling laws. The tests that were conducted during this research where performed to verify the physical model that was created. Since the processes within a curved pipe pull operation are of such low velocities, intertia plays a minor role in the process. Hydrodynamic loads are excluded from the scope of research and are therefore not of interest at this phase. The stiffness of the partially embedded model pipeline, surrounding soil body and the applied forces are the most important parameters within the tests. These can be modeled by classical structural- and geotechnical engineering, just like there soil - structure interaction.

When performing physical model tests in which a structural member is loaded by dynamic forces, it is very important to model according the applicable scaling laws of Froude. The element should be geometrically scaled, meaning that the model and full scale structure must have the same shape and their dimensions should have the same scale ratio.

$$\lambda = \frac{L_{fullscale}}{L_{model}} \tag{3.1}$$

In which;
λ = Scale factor $[-]$
$L_{fullscale}$ = Full dimension $[m]$
L_{model} = Model dimension $[m]$

Besides the length-scales, other applicable parameters scale via a specific power of the geometrical scale parameter. According to the latter, most of the other scaling relations can be derived from the physical units. The scaling factors of Froude are presented in table 3.1.

Physical parameter	Unit	Multiplication factor
Length (Diameter)	$[m]$	λ
Structural mass	$[N]$	λ^3
Force	$[N]$	λ^3
Moment	$[Nm]$	λ^4
Pressure	$[N/m^2]$	λ
Structural stiffness	$[Nm^2]$	λ^5

Table 3.1: Applicable Froude scaling factors

3.3.1. Target pipeline

To create correctly scaled model pipelines one needs to define a target pipeline. Due to dozens of years of executing and tendering pipe pull projects, there is a broad in-house knowledge within Boskalis regarding the nearshore pipeline installation market.

The tender department of Boskalis was concerned to define a target pipeline for the physical tests of this research. The specifications of the target pipeline can be found in table 3.2. The weight and bending stiffness of the pipeline are acquired in accordance with the calculation methods stated in Chapter 2.

Property	Abbreviation	Magnitude	Unit
Diameter / thickness ratio steel pipeline	Ds/t	40	$[-]$
Diameter steel pipeline	Ds	508	$[mm]$
Thickness steel pipeline	t	12.7	$[mm]$
Thickness concrete weight cover	C	40	$[mm]$
Total outer diameter	D	588	$[mm]$
Dry weight	W	369	$[kg/m]$
Target submerged weight	Wsub	80-250	$[kg/m]$
Bending stiffness (assuming zero bond with concrete coating)	EI	$127 * 10^6$	$[Nm^2]$

Table 3.2: Target pipeline of the physical scale tests

3.3.2. Model pipelines

Because it is hard to geometrically scale sand grains to a small scale, the initial approach of the physical tests was to create a test setup in which the pipe scale was kept as large as reasonably possible. Furthermore, large scale experiments would help to assess the curved pipe pull tests with a higher certainty, since measurement errors and scale effects of large scale experiments are smaller.

Since the moment of inertia of a geometrically scaled pipeline scales to the fourth order and structural stiffness scales to the fifth order, the material that is chosen should be more flexible than steel. Therefore different dimensions of polyvinyl chloride (PVC) sewer pipes were examined. The PVC pipes were concluded to scale well with the proposed target pipeline. The three different pipe dimensions of model pipelines are presented in table 3.3. During the subsequent subsections we will zoom into their most important properties.

Property	50 mm - 1.8 mm	50 mm - 3.2 mm	110 mm - 3.2 mm	Unit
Outer diameter	50	50	110	$[mm]$
Wall thickness	1.8	3.2	3.2	$[mm]$
Scale factor λ	11.8	11.8	5.3	$[-]$

Table 3.3: Dimensions of tested PVC models

The model pipelines are tested at a length of twelve meters. Although the pipes could not be bought of the desired length, homogeneous pipe behaviour was the aim of the design. Per model pipe, three different sections where connected by means of an inner socket and special PVC glue. An example of these sockets can be observed in figure 3.10. By means of this connection the influence of enlarged bending stiffness and diameter is reduced to the minimum. After every test the connections where checked for glue failure, this was never visibly observed. Test results did not show sign of stiffness discrepancies at the pipe connections.

Figure 3.10: Socket connection of the 50 mm - 3.2 mm model

3.3.3. Scaling pipeline stiffness

In table 3.4 the actual stiffness and scaled stiffness of the tested model pipelines is presented. One can observe that the stiffness of the small diameter model pipelines (50mm) are of the same order of magnitude as the stiffness of the scaled down target pipeline. The larger diameter pipeline (110mm) is almost one order of magnitude less stiff as the scaled down target pipeline stiffness. Although the latter might suggest that the largest diameter pipeline is too flexible, the model should give correct computations for more flexible pipelines as well. Therefore it is interesting to test this relatively large and flexible pipeline as well.

By conducting tests with different (scaled) pipe stiffness's within the scope of interest, the influence of pipe stiffness's can be examined extensively.

Parameter	50 mm - 1.8 mm	50 mm - 3.2 mm	110 mm - 3.2 mm	Unit
Outer diameter	50	50	110	$[mm]$
Wall thickness	1.8	3.2	3.2	$[mm]$
Scale factor λ	11.8	11.8	5.35	$[-]$
Target stiffness	566	566	29200	$[Nm^2]$
Actual stiffness	238	388	4600	$[Nm^2]$
Percentage of target stiffness	42.0	68.6	15.75	[%]

Table 3.4: Stiffness properties tested PVC models

3.3.4. Scaling pipeline weight

Since the scaled empty weight of the pipelines is insufficient, compared to our arget pipe weights defined in section 3.3.1, the pipeline weight was modified. Special attention was payed to influence the stiffness of the pipeline as little as possible. Therefore the two small pipelines are ballasted with (one, two or three) flexible steel cables and the larger diameter pipeline was ballasted by means of an anchor chain.

Figure 3.11: Anchor chain ballast installation of the 110 mm model test pipeline (fixed to pull head)

By conducting tests with different (scaled) pipe weights within the scope of interest, the influence of pipe weight can be examined extensively. The actual weight and scaled weight of the tested model pipelines are listed in tables 3.5 and 3.6.

Parameter	50 mm - 1.8 mm	50 mm - 3.2 mm	110 mm - 3.2 mm	Unit
Outer diameter	50	50	110	$[mm]$
Wall thickness	3.2	1.8	3.2	$[mm]$
Scale factor λ	11.8	11.8	5.3	$[-]$
Empty weight	0.35	0.61	1.40	$[kg/m]$
Weight (incl. 1 cable)	-	0.96	-	$[kg/m]$
Weight (incl. 2 cables)	-	1.29	-	$[kg/m]$
Weight (incl. 3 cables)	1.36	1.62	-	$[kg/m]$
Weight (incl. 1 chain)	-	-	8.40	$[kg/m]$

Table 3.5: Actual weight tested PVC models

Parameter	50 mm - 1.8 mm	50 mm - 3.2 mm	110 mm - 3.2 mm	Unit
Scale factor λ	11.8	11.8	5.3	$[-]$
Scaled empty weight	48.4	84.4	40.0	$[kg/m]$
Scaled weight (incl. 1 cable)	-	133	-	$[kg/m]$
Scaled weight (incl. 2 cables)	-	178	-	$[kg/m]$
Scaled weight (incl. 3 cables)	188	224	-	$[kg/m]$
Scaled weight (incl. 1 chain)	-	-	240	$[kg/m]$

Table 3.6: Scaled weight tested PVC models

One might notice that the weight seems to be scaled by the second order, instead of the third order presented in table 3.1. In this case that is valid because we discuss a set length of pipeline (one running meter). In accordance with the geometrically scaling theory, the length would normally decrease with the scaling factor as well.

3.3.5. Scaling effects sand

The setup was filled up with a clean spherical silica sand that, according to the international NEN-EN-ISO 14688 standard, is qualified as very fine to medium fine sand. It was tested in the Boskalis inhouse geotechnical lab Dolman to define the properties. The median sieve diameter (D50) of the sand is $166\mu m$, which is comparable to the sand on the Dutch coast.

Continuum behaviour When conducting experiments which involve soil - structure interaction, it is important to create a scale at which enough soil grains interact with the structural member. When sufficient grains interact with the structural member, one can assume the surrounding soil to react as a continuum. Continuum mechanics relates the kinematics and mechanical behaviour of materials modeled as a continuous mass rather than discrete particles.

Within the geotechnical experiments; a rule of thumb exists which states that the amount of grains that fits into the (smallest) contact length of the structural member is larger exceeds thirty units, the soil will behave as a continuum. For the experiments conducted within this research, the smallest contact length property between the pipeline and the surrounding sand is resembled by the pipeline embedment. The minimum embedment is encountered when the smallest diameter pipeline has the minimum normalized embedment. Equation 3.2 shows that the rule of thumb holds for the lowest normalized embedment (0.1) of the smallest pipeline diameter ($D_o = 50mm$). Taking into account that this is the lower limit of embedment, one can say the continuum soil behaviour holds for all conducted experiments.

$$\frac{(z/D)D_o}{D_{50}} = \frac{0.1x50}{0.166} = 30.12 \tag{3.2}$$

Geometrical scaling The larger grains in the sand cannot be qualified as sand (but gravel) when they are geometrically scaled with respect to the smallest scale, although the grain shape would still be spherical instead of angular (like gravel). Since the sand scales well for the most grains and it is hard to find finer grained sand, the proposed sand is applied. The actual sieve curve and scaled sieve curves are presented in figures 3.12 and 3.13.

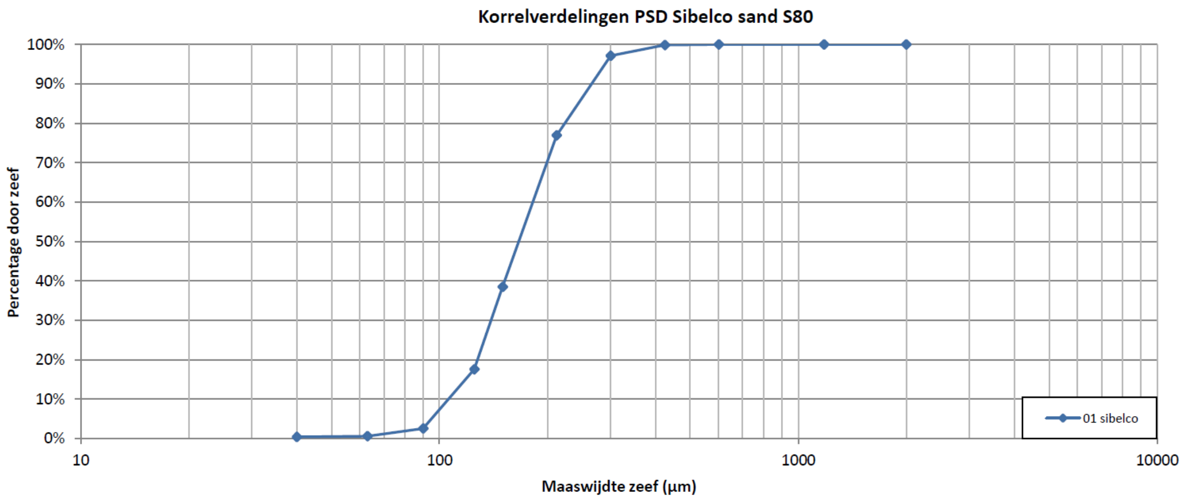

Figure 3.12: Sieve curve of the applied S80 sand

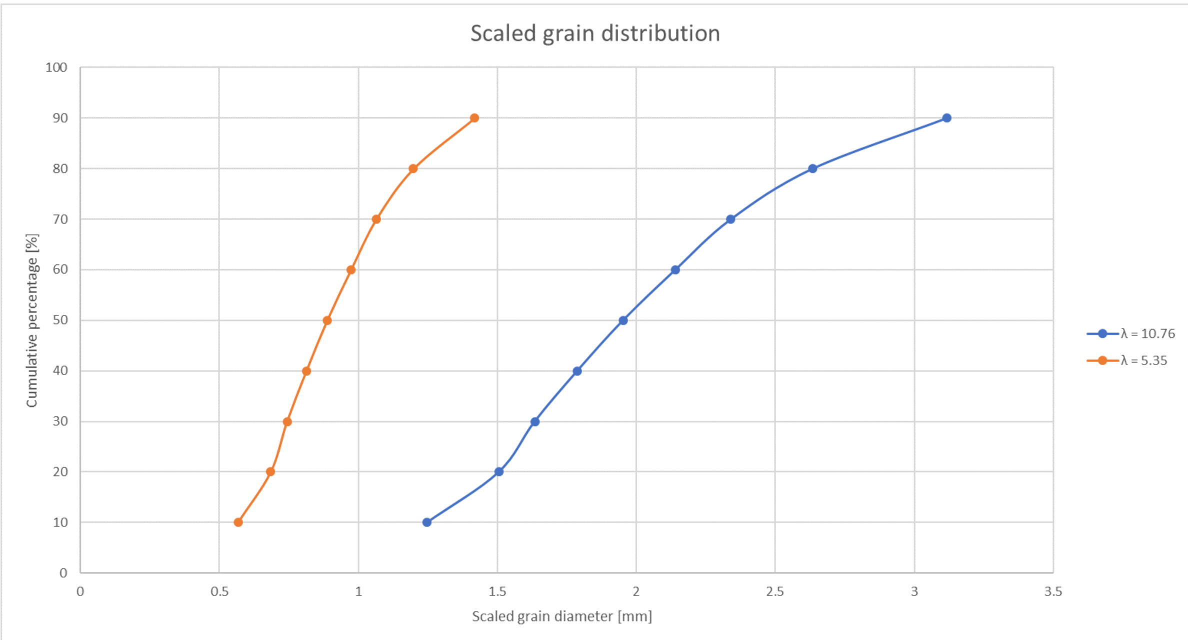

Figure 3.13: Scaled sieve curve of the applied S80 sand

Apart from the grain size of the test sand there are some other soil properties that are of importance to compute the soil resistance during the physical tests. Within the Dolman lab the internal friction angle, minimum and maximum density where determined. The result of these tests can be observed in figure 3.14 and table 6.3. Density of the sand during the physical tests will be between the minimum and maximum bulk density.

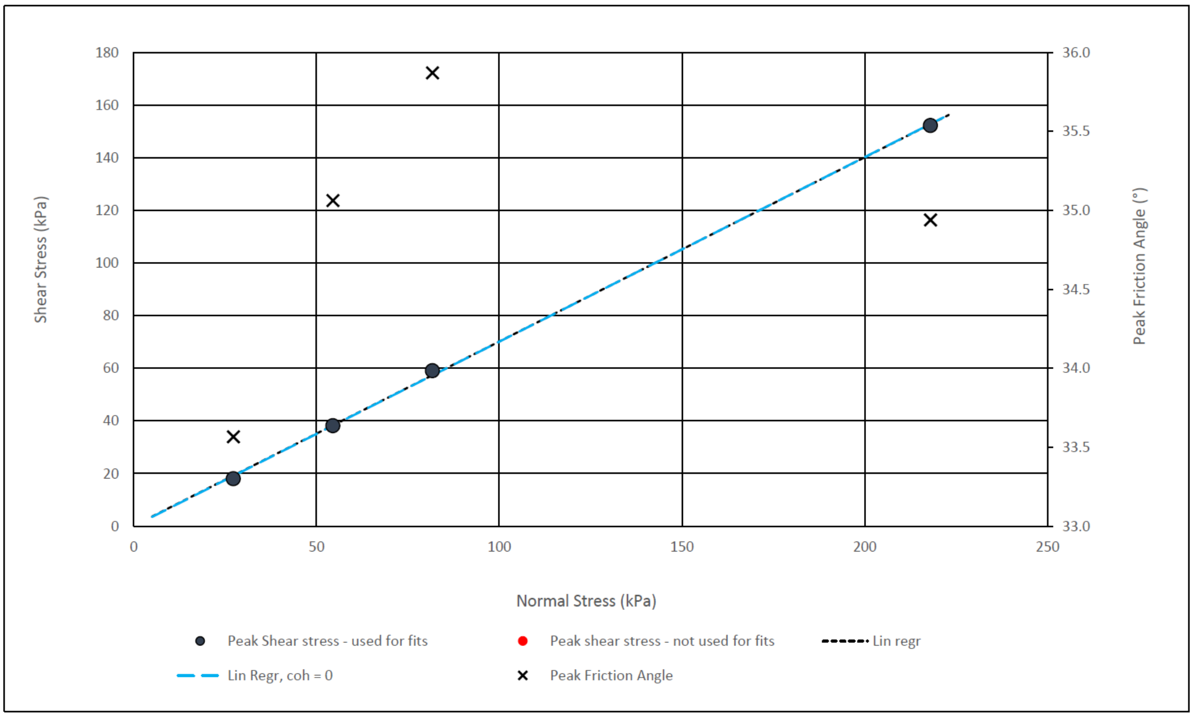

Figure 3.14: Direct shear test results

Property	Magnitude	Unit
Internal friction angle	35.0	$[degrees]$
Maximum bulk density	1602	$[kg/m^3]$
Minimum bulk density	1349	$[kg/m^3]$

Table 3.7: Properties test sand

3.4. Summary of the physical test setup

By means of this chapter, a clear overview of the physical test setup of this research is obtained. The enclosed sections in the chapter describe the different components, design criteria and scaling of the model pipelines. A brief conlusion of these subjects is reported in the following paragraphs.

Setup explanation Section 3.1 gives a brief but clear overview of the test setup. The sections shows that the unique setup enables experiments that model and study the adapted pull out method, described in section 1.2.2, into detail.

Reference to the theory Section 3.2 exposed the design criteria and limitations that created the base for the setup.

Scaling Throughout section 3.3 the scaling of the model pipelines and sand is discussed. Five different model pipelines are examined within the physical tests, so that the computational model can be verified over a wide range of model pipelines. The model pipeline with a D_0 50mm and t=3.2mm has the best scaling properties because the bending stiffness scales well. Fine silica sand is applied to model the behaviour of sandy seabeds as well as reasonably possible.

4

Experiments

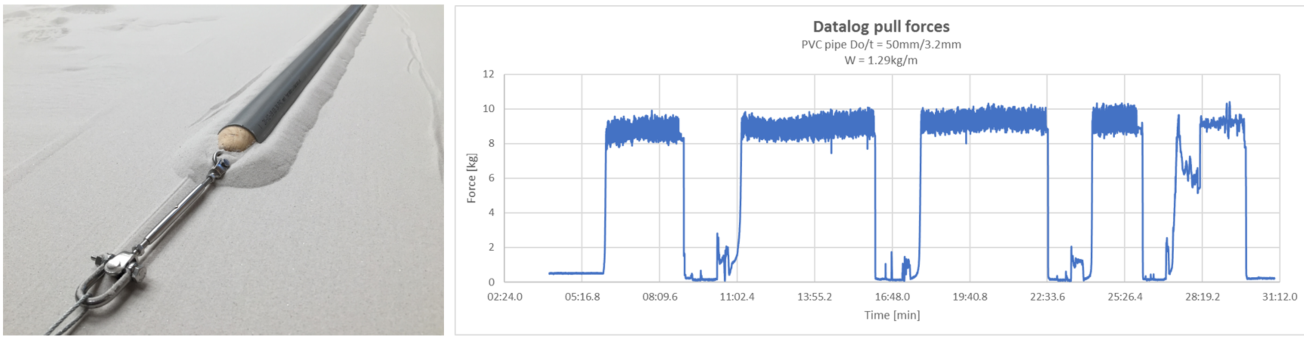

Figure 4.1: (l) Pull head of D_0 50mm pipeline after an experiment and (r) datalog example of pull forces

Chapter 4 provides information regarding the experiments conducted with the physical test setup, which is described in chapter 3. The chapter treats the two different kinds of conducted experiments, the procedures used to gather data and the obtained experimental results. A brief summary of the findings is enclosed to conclude.

Physical testing brings risks, certainly when applying large forces. It is mandatory that the student, project manager in this case, ensures the tests are performed in a safe and correct manner, within applicable standards.

4.1. Explanation of experiments + example

During the physical test phase of this research, two different kind of tests have been conducted:

1. Controlled pull tests (28 experiments)
2. Breakout pull tests (2 experiments)

Both types of tests are related to a specific way of installing pipelines into a curved trajectory. The controlled pull installation method is the prefered one, therefore it is tested more extensively as the breakout pull method. Within the next two subsection, both tests are explained and clarified by means of an example.

4.1.1. Controlled pull tests

The controlled pull experiment is related to the adapted pull-out method, which is described in section 1.2.2. By gently pulling the pipeline into a curve while it propagates in axial direction, it is aimed to obtain a curved pull operation that is as controlled as reasonably possible. During a controlled pull installation of pipelines into a curved trajectory, the goal is to maintain a constant embedment throughout the complete pull.

To force the pipeline into a curved trajectory during an axial pull, a lateral force component has to be imposed to the pipe head. By applying a small angle between the pull wire and the pipe head, the lateral force component is obtained. As described in section 1.2.2, the offshore positioned installation vessel or barge is responsible for an angle between the pull wire and pipeline during a controlled curved pull operation.

During the controlled pull experiments within this research it is the aim to always keep a mild angle between the pull wire and the pipeline. This is achieved by relocating the sheave (on the sheave beam) towards the winch. As the pipeline propagates into a curve trajectory, the pipeline aligns with the pull wire. As a result, the sheave has to be relocated multiple times to maintain a pull angle with the pipe head. A complete example of a test procedure is explained within the next paragraph.

Example controlled pull test We use an experiment of the best scaling pipeline with a D_o=50mm and t=3.2mm (1 ballast cable) as an example. The test sequence can be briefly prescribed by the following stages:

1. Start data logging
2. Straight pull
3. Relocating of the sheave
4. Curved pull
5. Repeat stage 3-4 (until pipe reaches end of the flume)
6. Secure data logging

During stage 1, load cells and camera's are switched on to start the data logging. The pipeline is mainly situated in the firing lane and the pull wire is in line with the pipeline. Stage 1 can be observed in figure 4.2.

Figure 4.2: Starting position of the test, with most pipeline length in the firing lane

When the data logging is started successfully, the actual experiment can start. The pull winch is switched on (stage 2) and the tension in the wire builds up. When the pull tension exceeds the axial pipeline resistance, the model pipe starts propagating in axial direction (desired axial propagation velocity was approximately 0.02 m/s for all conducted tests). As it propagates it will create embedment, as described in 2.3.1.

After a straight section of the trajectory, curvature is induced to the pipeline. The pull is stopped, and by creating some slack in the pull wire the sheave can be relocated in the direction of the winch (stage 3). From now on the pipe head will be loaded in lateral direction and the pipeline will start propagating into a curved trajectory as a result of this lateral component.

When the pipeline slowly curves throughout the curved pull operation (stage 4), it aligns with the pull wire. Since it is important to maintain a lateral component that is as large as possible (without causing a lateral breakout), the sheave is relocated to a new location when the angle of the pull wire and pull head reduces (stage 5). Stage 2 to 5 are presented in figure 4.3.

Figure 4.3: Repositioning of the sheave along a test sequence, to maintain the maximum lateral force possible on the pipe head

After the last relocation of the pull-wire guiding sheave, the pipe is pulled until it almost reaches the end of the flume. When the pipeline is in this final location, the winch is stopped and the pipeline will stop moving as a result of the absence of pull tension. The final situation can be observed in figure 4.4.

Figure 4.4: Final position of the model pipeline after the experiment

When the experiment has stopped, the pull and positioning data of the pipeline should be secured. The pull data (figure 4.5) and videos of the surveillance camera are saved. The drops of pull tension during relocation of the sheave are clearly visible in the pull force datalog.
By using the gantry crane and GoPro, the position of the pipe is logged according section 4.2.2. AgiSoft helps to generate an accurate 2D model of the final stage of the experiment, visible in figure 4.6.

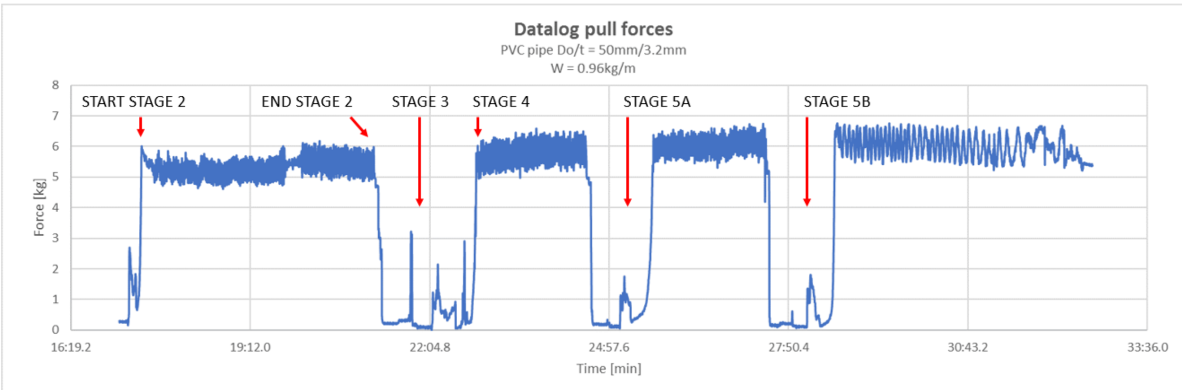

Figure 4.5: Datalog pull forces controlled pull example test

Figure 4.6: 2D AgiSoft model of the experiment, providing positioning data of the pipeline

4.1.2. Breakout pull tests

In contradict to the controlled pull-out, the breakout pull method is a method in which the pipeline will leave the embedment. The lateral force that is applied to the pipe head has a magnitude that enforces a breakout and light pipe behaviour. Forcing a pipeline into lateral breakout behaviour enables to install pipelines into smaller radii as the radii that are feasible with the controlled pull installation method.

Although te numerical model within this research is created to predict curved controlled pipe pull operations, it is tested for the applicability on breakout pulls as well. Within the next paragraph an example of a forced breakout experiment is described.

Example breakout pull test Within this paragraph an example of the lateral break out test of the D_o=110mm and t=3.2mm is explained. This particular example is discussed again in section 6.3.2, where it is used to validate breakout behaviour computations of the numerical model.

Figure 4.7: Starting position of the test, with most pipeline length in the firing lane

The subsequent stages of a breakout pull test can be described as follows:

1. Start data logging
2. Straight pull
3. Relocating of the sheave
4. Breakout pull
5. Secure data logging

Stage 1 and 2 are exactly the same as during a controlled pull out experiment, described in 4.1.1. The starting of the breakout experiment can be observed in figure 4.7. During the relocation procedure of the sheave (stage 3), the step of displacement is significantly larger than during a controlled pull-out experiment. The situation after stage 3 is shown in figure 4.8.

Figure 4.8: Model pipeline after straight pull, ready to be enforced to breakout in lateral direction

After starting the winch, the tension in the pull wire rises (start of stage 4). The pipe head is subjected to a lateral force that exceeds the capacity of the soil, causing bearing behaviour of the surrounding sand and a lateral breakout of the pipeline. Since the axial force does not exceed the axial friction of the pipeline, it does not propagate in axial direction. The latter situation is displayed in figure 4.9.

Figure 4.9: Model pipeline during a lateral breakout, showing no axial propagation

Securing the data is equal to the procedure of the controlled pull test, as described in 4.1.1. The datalog of the pull forces of the breakout pull prescribed in this paragraph is shown in figure 4.10.

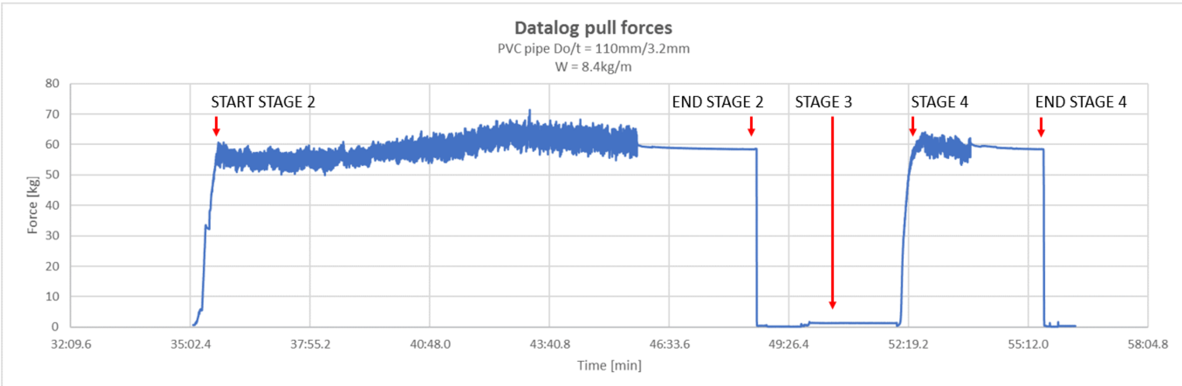

Figure 4.10: Datalog pull forces breakout pull example test

4.2. Procedures

During the physical phase of this research, multiple procedures were in place to facilitate proper data gathering and a safe working environment. The procedures that hold for data gathering of the experiments are prescribed throughout this section.

4.2.1. Video logging

All experiments are logged by means of a surveillance video system. The videos provide a top view of the wide part of the test flume, were the model pipelines are pulled into a bend. An example of the video registration can be found in figure 3.6, there are multiple throughout the report.
By means of the top view videos, every movement is logged and the whole test procedure can be analyzed into detail.

Detailed videos By means of a GoPro camera, particular phenomena can be captured. The GoPro videos provide more detailed images of processes and capture these from another prospect as the surveillance camera. An example can be found in figure 4.11, where the camera was placed on top of the 110 mm test model during the forced breakout experiment.

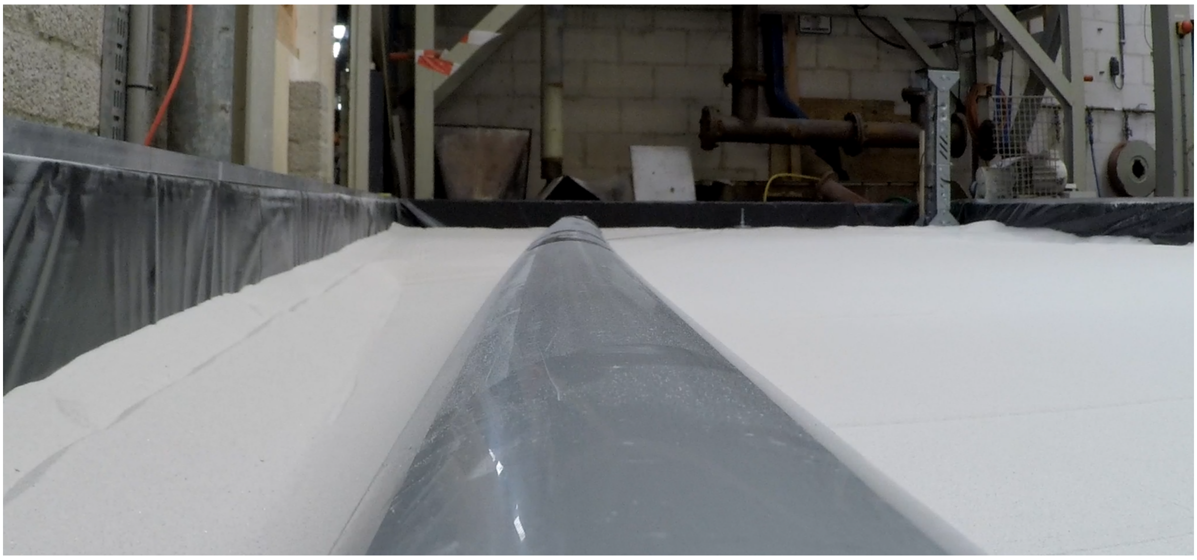

Figure 4.11: GoPro video capture during a forced breakout experiment of the 110 mm pipeline (treated in section 4.1.2)

4.2.2. Position data gathering

A detailed log of model pipelines positioning throughout the experiments is essential to analyze specific interesting situations that appear. Although the surveillance camera captures the major overall motions of the pipeline, it cannot be used to capture the exact position of pipelines during a test. The fish-eye effect of the surveillance camera disables to use it for position logging purposes.

Instead of manually measuring the pipelines along a test, a more advanced method is used. Photogrammetric software package AgiSoft is applied to create a 3D capture of the complete setup after an experiment. Since the outer bend track of the model pipeline is visibly by the trench mark in the sand, the position of the pipeline during every specific moment throughout a test can be recaptured. A short description of the positioning data gathering procedure is prescribed in this subsection.

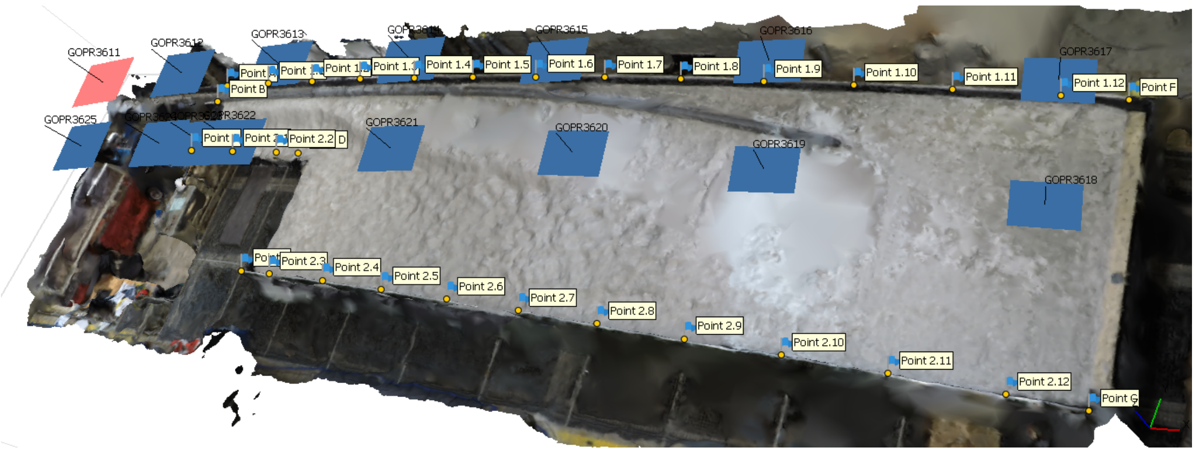

Figure 4.12: AgiSoft 3D model of experiment

From 3D to 2D Collecting the positioning data of the pipeline starts by taking a series of photographs from a top view position. By using the gantry crane of the HydroLab, two lines of photographs are made by means of the GoPro. An overlap of the images is essential to create a proper 3D model.
The photographs are imported into the software and stitched together by means of their overlap and ground control points. Ground control points (GCP's) can be observed in the AgiSoft printscreen of figure 4.13.

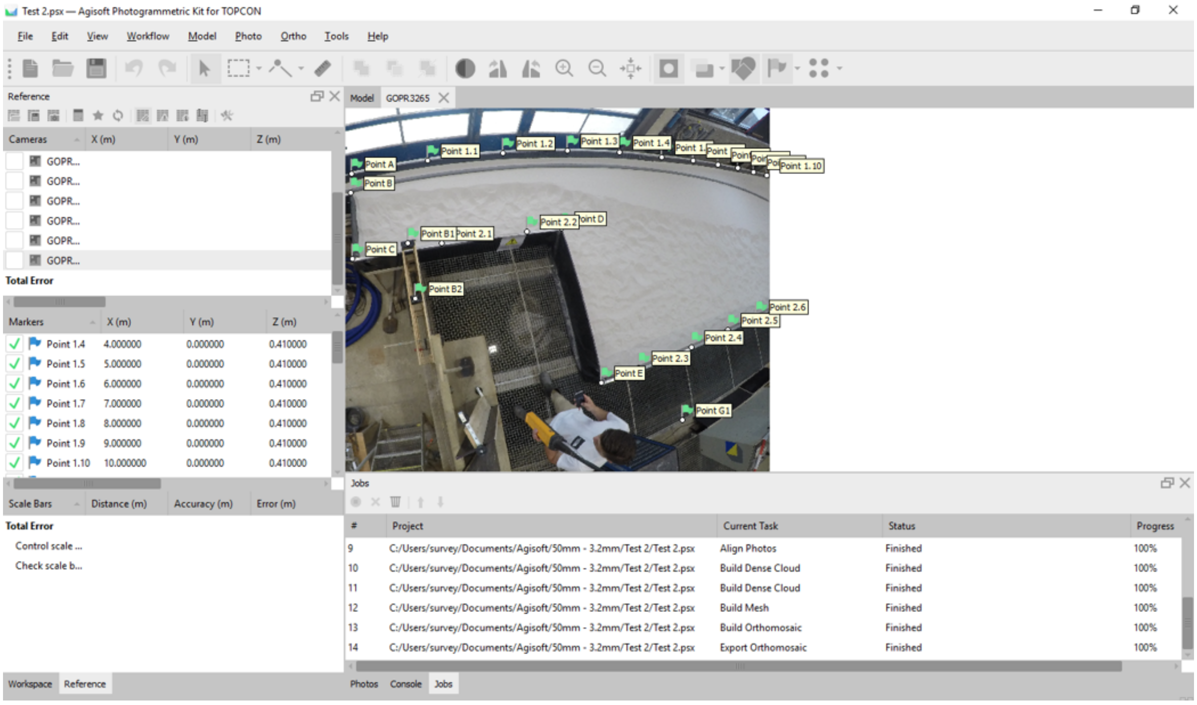

Figure 4.13: Printscreen of AgiSoft user-view, showing GCP's

After stitching of the photographs, a 3D tiled model as displayed in figure 4.12 is obtained. Once the 3D model is constructed, the model can be converted into a 2D model with a one-to-one scale and a accuracy in the order of millimeters. By means of AutoCad software, the radius of the pipeline can be determined. An example of the 2D model is displayed by figure 4.14.

Figure 4.14: AgiSoft generated 2D model of experiment

4.2.3. Pull data gathering

By means of the load measuring equipment the setup supplies the pull data on the pipehead throughout an experiment. By combining the position of the pipe, the pull wire angle with the pipe head and the pull force the subjected axial and lateral force components at the pipe head can be obtained. Pull data will be examined more extensively in chapter 6.

4.2.4. Determining sand compaction

Campaction of the sand is an important input parameter in the geotechnical soil modelling and therefore it has to be determined as precise as reasonably possible. To determine the compaction of the sand two different methods are used:

1. Core ring test
2. Manual cone penetration test (CPT's)

After the conducted soil tests, the in-situ bulk density appeared to be approximately 1500 kg/m^3. This density is taken into account for numerical model calculations. The results of the tests are described in the following two paragraphs.

Core ring test During the core ring test a metal ring is inserted into the leveled sand bed. Hereafter, the ring is closed off by means of lids. By determining the weight of the sand in the ring, the density can be calculated. The results can be found in table 4.1.

In general, core ring tests are performed to undrained or cohesive materials. When applying a core ring test in dry sand, there is more loss of material. Due to the latter, the sand trapped inside the ring decreases and so does the density. This implies that the core ring test underestimates the density (and compaction) of the sand.

Figure 4.15: Core ring test to determine insitu density sand

Property	Magnitude	Unit
Weight core ring	0.11271	$[kg]$
Weight core ring filled with sand	0.26021	$[kg]$
Weight sand in core ring	0.1475	$[kg]$
Core ring volume	100	$[cm^3]$
Density core ring sample	1475	$[kg/m^3]$

Table 4.1: Core ring tests data

Manual CPT's Manual CPT's were conducted before every experiment. The CPT's were performed at the leveled section of the bed. Multiple CPT's were performed for one experiment, few discrepancies were measured per test and over the complete test range. Therefore, the in-situ bulk density was assumed to be steady throughout the physical test campaign.
Within this section the analysis of the CPT data is described.

The manual CPT device was used up to half the sand depth (≈ 0.12m) to prevent influence of the physical test setup bottom. A 5 cm^2 cone was used along all CPT tests. All tests gave a value in the order of 420 Newton, as displayed in figure 4.16.

Figure 4.16: Manual CPT's to determine the sand compaction

Lunne and Christoffersen (1983) give an approximate correlation (displayed in 4.1) between the relative density, cone resistance and effective stress for young silica sands. By means of iteration it is possible to determine the compaction and bulk density of sand when the cone resistance, minimum bulk density and maximum bulk density are known.

$$D_r = \frac{1}{2.91} \ln \frac{q_c}{60 {\sigma'_v}^{0.7}} \tag{4.1}$$

In which:
D_r = Relative density $[-]$
q_c = Cone resistance $[N/m^2]$
σ'_v = Effective vertical soil pressure $[N/m^2]$

And:

$$\sigma'_v = \rho * z \tag{4.2}$$

Within table 4.2 the porosity and void ratio of the minimum and maximum bulk density are displayed. The porosity and void ratio are interrelated by means of relations 4.3 and 4.4.

$$n = \frac{\rho}{\rho_s} \tag{4.3}$$

In which:
n = Porosity $[-]$
ρ = Density $[N/m^3]$
ρ_s = Grain density $[N/m^3]$

$$e = \frac{n}{1-n} \tag{4.4}$$

In which:
e = Void ratio $[-]$

Density	$\rho[N/m^3]$	$n[-]$	$e[-]$
Minimum bulk density	13234	0.491	0.963
Maximum bulk density	15716	0.395	0.653

Table 4.2: Test sand porosity and void ratio

The relation of Lunne and Christoffersen converges to a bulk density (ρ) of 1500 kg/m^3 for the parameters of the sand in the physical test setup. With the relating minimum and maximum density this implies a relative density (D_r) of 0.639.

4.3. Results

Within this section the results of the thirty tests are displayed. The results are categorized after the kind of test (controlled pull of breakout) and the model pipeline.

Within appendices A, B, C, D and in chapter 6 the results of the experiments are threatened more elaborately.

4.3.1. Controlled pull tests

The results of the twenty-eight controlled curved pull experiments are described by means of the minimum pull radius that was obtained during the test. Controlled pull radii are plotted as a function of the relative embedment of the model pipeline. The pull data of every specific model pipeline is displayed is a separate graph for convenience. The graphs are displayed subsequently.

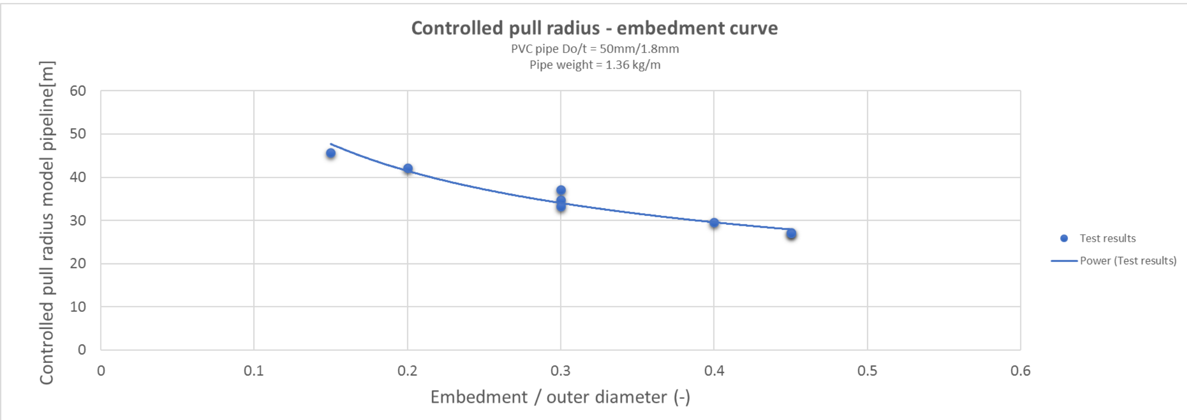

Figure 4.17: Experimental test results of the D_0 50mm (t=1.8mm and W=1.36kg) model pipeline

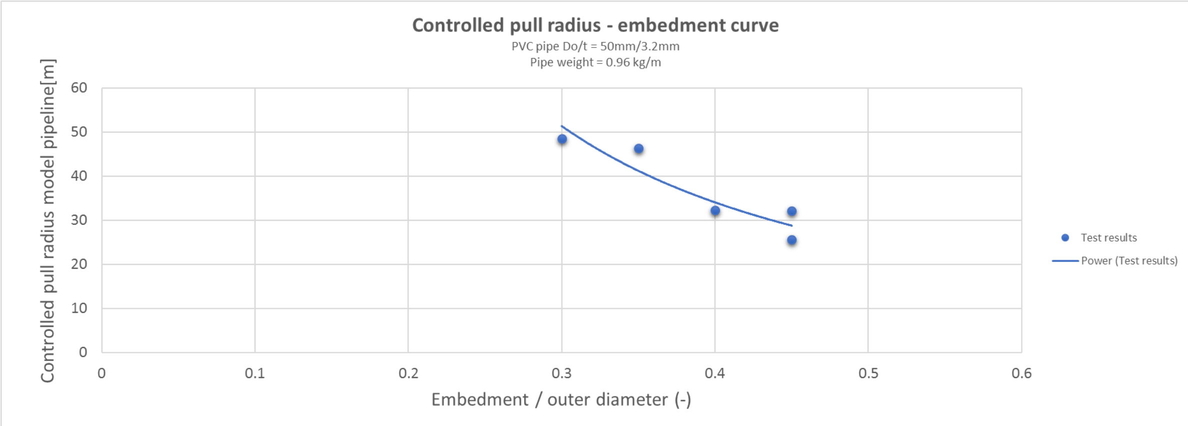

Figure 4.18: Experimental test results of the D_0 50mm (t=3.2mm and W=0.96kg/m) model pipeline

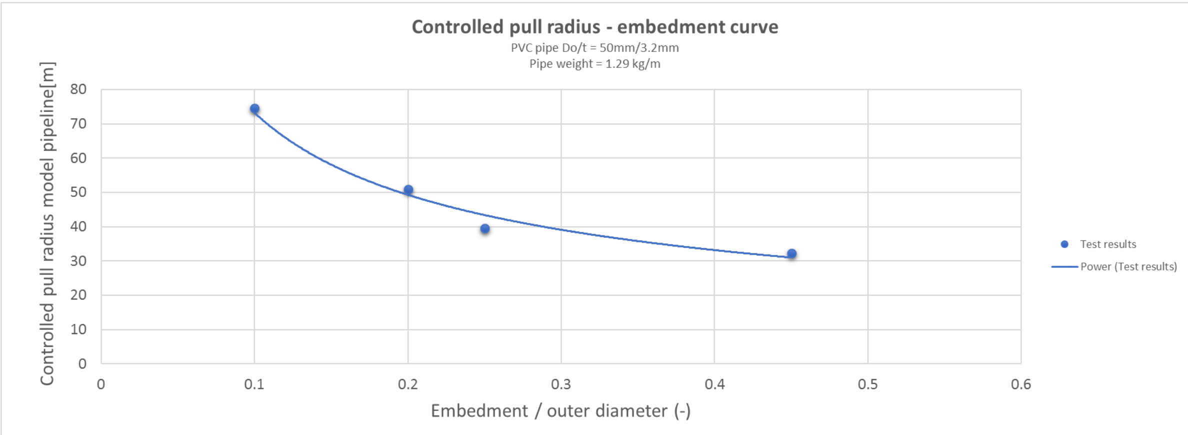

Figure 4.19: Experimental test results of the D_0 50mm (t=3.2mm and W=1.29kg/m) model pipeline

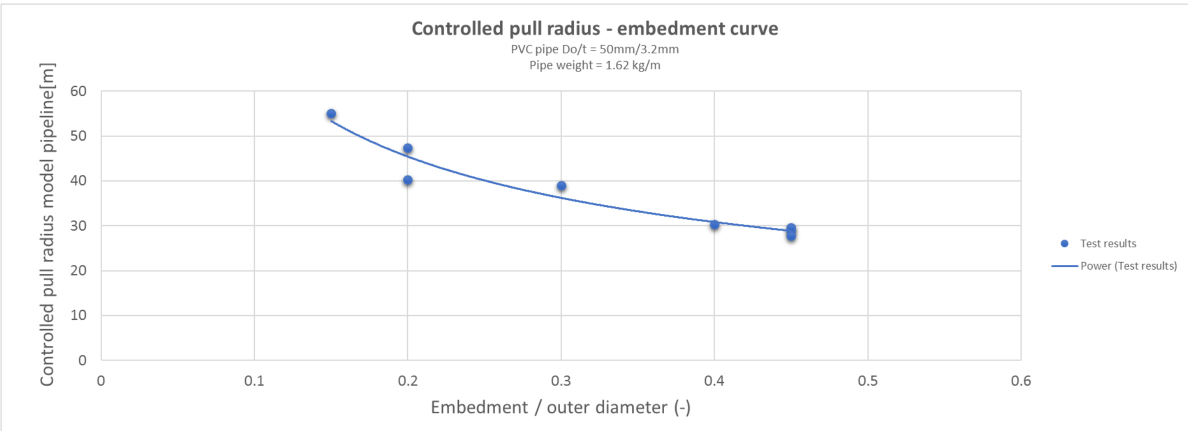

Figure 4.20: Experimental test results of the D_0 50mm (t=3.2mm and W=1.62kg/m) model pipeline

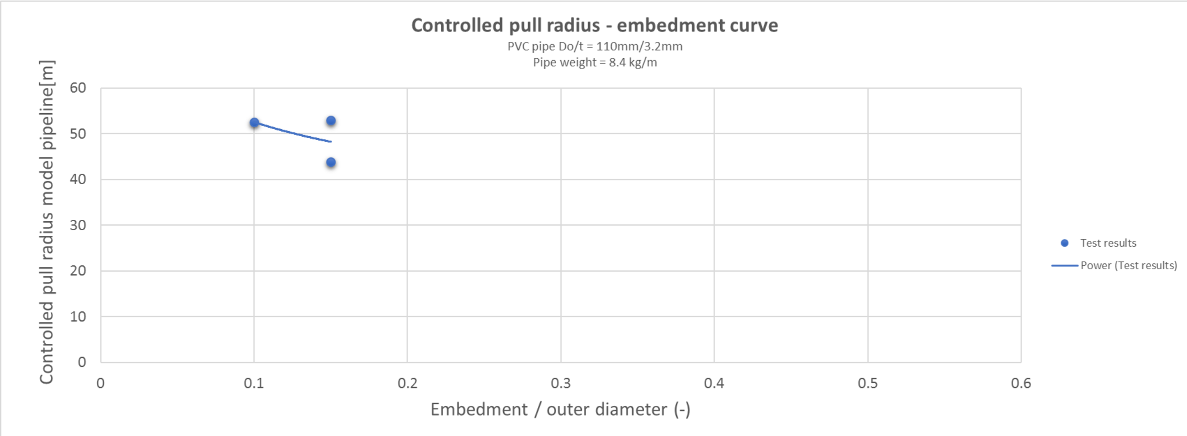

Figure 4.21: Experimental test results of the D_0 110mm (t=3.2mm and W=8.4kg/m) model pipeline

Combined plots

For analyzing purposes, it is interesting to plot pull graphs of different model pipelines together. The most interesting cases appear when all model parameters of those pipeline models are equal, while solely one parameter differs. When the latter happens, the influence of this single (varying) parameter can be examined best. The following two figures show graphs of a combined plot of the test results of multiple pipelines that differ at one single property.

Figure 4.22 shows the controlled pull radii of two D_0 50 mm model pipelines that differ solely in stiffness (neglecting a theoretical 5% weight difference). The thick walled model pipeline has a 63% higher bending stiffness as the thin walled model pipeline.

The second figure 4.23, presents the combined plot of three D_0 50 mm model pipelines that solely differ in weight.

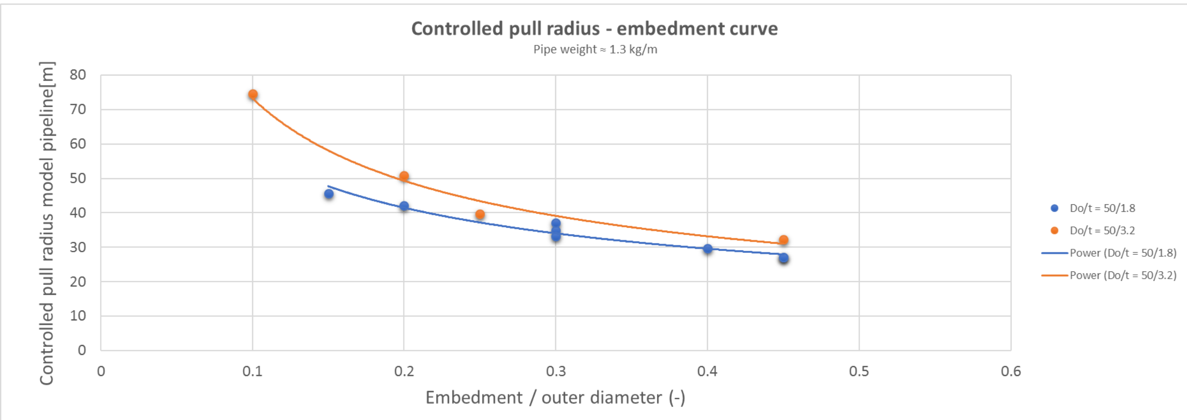

Figure 4.22: Experimental test results of the D_0 50mm (t=1.8mm / t=3.2mm and W≈1.3kg/m) model pipelines

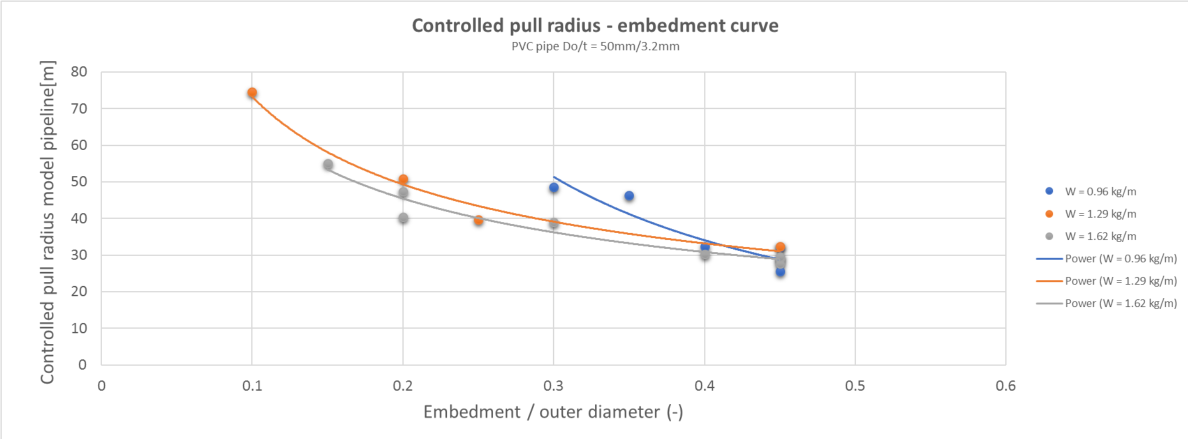

Figure 4.23: Experimental test results of the D_0 50mm (t=3.2mm and W=0.96kg/m / W=1.29kg/m and W=1.62kg/m) model pipelines

Qualitative sensitivity analysis of the experimental parameters
By comparing the plots of obtained experimental (all combined in figure 4.24) of the test campaign, the influences of the changing parameters can be examined qualitatively. Throughout this paragraph we will analyze the influence of the following three parameters:

1. Pipeline stiffness
2. Pipeline weight
3. Pipeline diameter

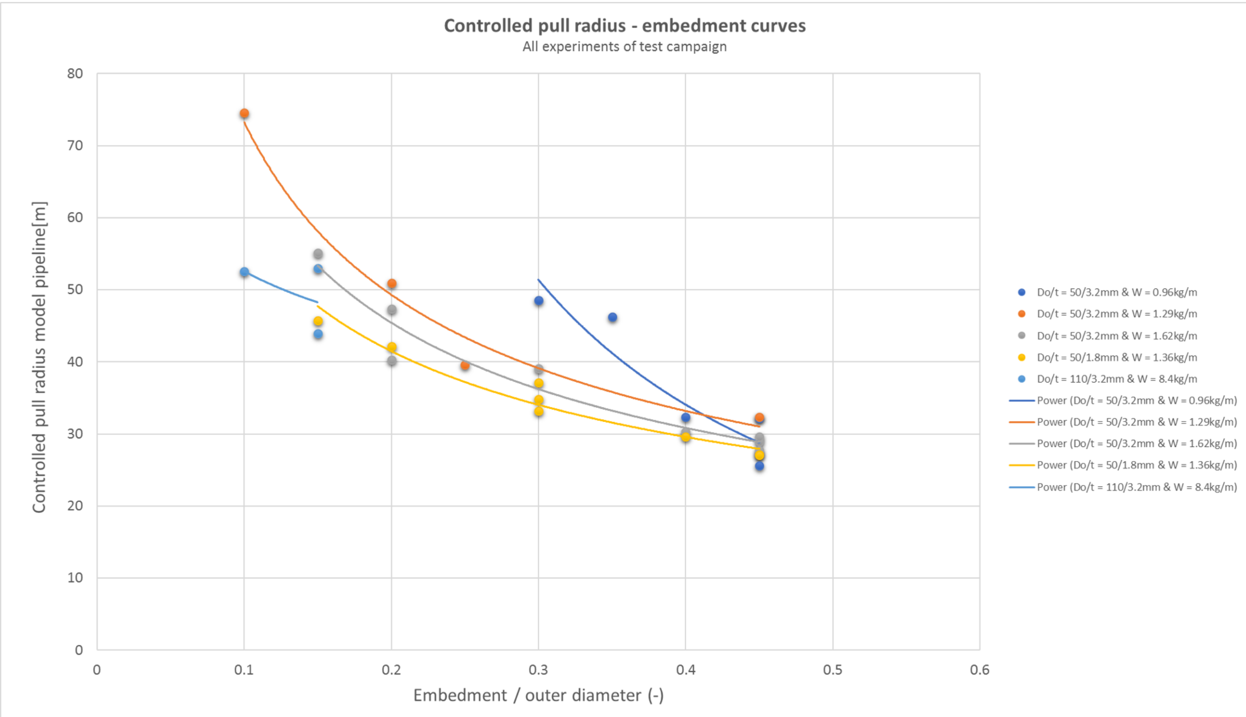

Figure 4.24: Combined plot of all controlled pull results of the test campaign

Pipeline stiffness By examining figure 4.22 the pure influence of pipeline bending stiffness can be deducted. The only difference between the two model pipelines was the wall thickness, resulting in a stiffness of the thick walled model pipe that was 63% higher as that of the thin walled pipeline. Pipeline weight and diameter were equal.

As expected, the pipeline with the large bending stiffness results in larger controlled pull radii. One can observe that the pull radius correlations of the different model pipes differ less then 63%, but 10-20%. From this observation we can conclude that the influence of pipeline stiffness is less than linear, under the applicable test circumstances.

Besides the former conclusion, the pull radius correlations of the two model test results show a contraction effect for larger normalized embedment rates. This can be explained by the influence of the lateral soil resistance, which gains influence with the increase of (relative) embedment. From this observation one can conclude that the relative influence of pipeline stiffness decreases with the increase of embedment.

Pipeline weight By examining figure 4.23 the pure influence of pipeline weight can be deducted. The only difference between the three model pipelines was the weight per running meter. Compared to the lightest pipe, the two subsequently tested pipes were $1/3^{th}$ and $2/3^{th}$ heavier. Pipeline stiffness and diameter were equal.

As for the pipeline stiffness, the pull radius correlations of the three different models show the trend that was expected. Larger pipe weights result in higher friction rates and therefore increase the relative influence of lateral resistance, ultimately enabling smaller controlled pull radii. Within the given test circumstances we can conclude that higher pipeline weights result in smaller controlled bending radii. The influence of weight increase seems to be less than linear, although the lightest (0.96 kg/m) pipelines complicates this analysis a little since it has no experimental data for small embedment rates.

By means of figure 4.23 it is not easy to conclude whether the influence of weight is dependent on the relative embedment of the pipeline. If we compare the light weight (0.96 kg/m) and middle weight (1.29 kg/m) pipelines we can see that the pull radius correlations of the two model pipes contract. This effect can be related to the relative influence of the passive lateral soil resistance in the total lateral soil resistance (as described by Verley and Sotberg (1994), section 2.2.2) for larger embedment rates. It implies that the relative influence of weight induced lateral friction is decreases for larger embedment rates.

Pipeline diameter The four controlled curved pull experiments performed with the 110mm model pipe (results in figure 4.21) reached less relative embedment as observed throughout the smaller 50mm model pipes. This can be a matter of coincidence, but since the 110mm pipe is 2.2 times the scale of the 50mm pipe, it has less relative (or scaled) axial propagation distance within the setup to gain embedment. The scaled weight of the 110mm pipeline, displayed in 3.6, is higher than that of the 50mm pipelines. Based on this fact, a larger embedment would be expected.

If the controlled pull radii of the 110mm pipe are compared to the 50mm pipes, as done in figure 4.24, one will notice that the radii are in the same order of magnitude (for the same embedment rates). Although the stiffness of the 110mm pipeline, given 3.4, is 11.8 or 19.3 times larger (4600/238 and 4600/238) than that of the 50mm pipes: the magnitude of the controlled pull radii is comparable. For an increased stiffness, increased pull radii are expected. Since the scaled pipe stiffness, also stated in 3.4, is too low to scale well with the target pipeline it is hard to draw conclusions from the four experiments with the 110mm pipe.
No conclusion are drawn from the 110mm pipe experiments, but the experimental data provided from the tests of this relatively flexible model are used to validate the numerical model predictions in 6.

4.3.2. Breakout pull tests

The two breakout pull experiments are displayed by means of a top view of the surveillance camera, shown in figures 4.26 and 4.25. Since the radius differs significantly along the forced breakout curvature, no radius is stated.

Figure 4.25: Experimental test result of the D_0 110mm (t=3.2mm and W=8.4kg/m) model pipeline breakout pull

Figure 4.26: Experimental test result of the D_0 50mm (t=3.2mm and W=1.29kg/m) model pipeline breakout pull

4.4. Summary of the experiments

From this chapter can be concluded that a successful campaign of experiments is conducted within this research. The predicted behaviour of the model pipelines during the experiments was as expected. Within the following paragraphs a brief summary of the sections is given.

Explanation of experiments + example Section 4.1 reveals the relation between the experiments conducted within this research and the two proposed installation methods to install pipelines into a curved trajectory. Each kind of experiment is clarified by means of an example experiment.

Procedures Within section 4.2 the logging procedures of the pull loads and positioning of the pipeline are discussed. The pull loads are logged by means of purpose made measuring structures (holding a load cell). Positioning data of the model pipelines is logged by means of a specialized photogrammetry technique.

Results Section 4.3 lines up the experimental results of thirty controlled pull tests and two forced breakout pull tests. Repeatability of the experiments was obtained when a model pipeline reached the same embedment multiple times. This implies low spread and high certainty of the experimental data.
Besides the latter, clear correlations appear in the experimental data plots. These trends are summarized in a quantitative parameter analysis.

5

Modelling

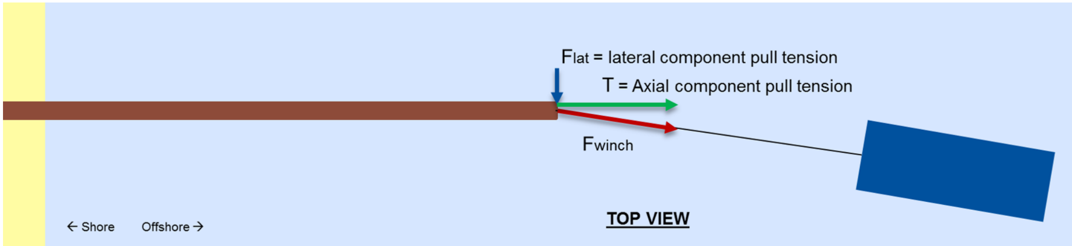

Figure 5.1: Schematization induced forced during inclined pipeline pull out

Within this chapter the link of the theory with the numerical prediction model of the research is explained. Chapter 2 provides the theoretical underlying base of the soil - structure interaction that is faced throughout curved pipe pull operations. During this chapter the behaviour of the pipeline and the surrounding soil are combined into one model that will be used to predict to what extend it is possible to pull pipelines into curves in the future.

5.1. Actual model explained

Due to the complexity of the soil - structure behaviour during a curved pipe pull operation, the final model of this research is a static non-linear numerical model. Along the process of creating this model, simpler taut string and linearly supported beam models were examined and considered to be insufficient for the complex scope of research.

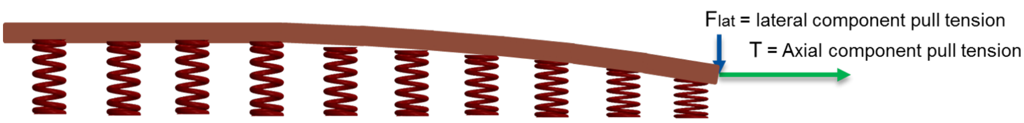

Figure 5.2: Schematization non-linear spring supported, tensioned bending beam

The model used during this research is that of a non-linear spring supported, tensioned bending beam. A schematization of the model is displayed in figure 5.2. It represents a top view model of a partially embedded pipeline subject to an inclined pull load, as can be observed in figure 5.1. Specifications of the proposed pipeline and on site seabed conditions can be adapted into the model according Chapter 2. The pipeline is represented by the bending beam and the lateral soil behaviour is captured by the springs. Due to the non-linearity of the lateral soil resistance in the model, a numerical approach is required to solve the system of differential equations.

5.1.1. Combined model

The model is a combination of the taut string model and the Euler-Bernoulli beam model, as described by Metrikine (2016). The taut string model is used to predict the transverse motion of a string, while the Euler-Bernoulli beam model is used to examine bending of a beam.
Both of the models are obtained by examining a infinitesimally short section of the beam. If this section displaces in lateral direction with a certain acceleration, Newton's second law states that the sum of applied forces on the section should be equal to the mass times the acceleration of the section. By making the assumption that the slopes of the deflecting structural element are small, the relations that are described within this chapter can be obtained.

Within the next two paragraphs the string and beam model are discussed, after which they are merged into the model of a tensioned beam. Please note that the paragraphs prescribe vertical motions of the examined structural members.

Transverse motion of a string

Newtons second's law provides the equation of motion (EOM) for a transverse moving string.

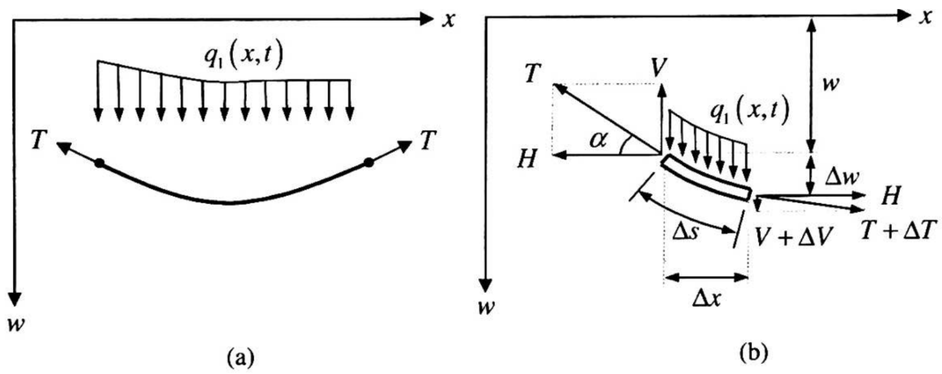

Figure 5.3: (a) Taut string subject to a distributed load and (b) differential element of the taut string subject to the tension and external load

$$\rho A \Delta x \frac{\delta^2 w}{\delta t^2} = V + \Delta V - V + q_1 \Delta x = \Delta V + q_1 \Delta x \tag{5.1}$$

In which:
ρ = Mass density $[N/m^2]$
A = Cross-sectional area $[m^2]$
w = Transverse motion $[m]$
V = Vertical component tension $[N]$
q_1 = External vertical load $[-]$

If one considers the condition of small transverse motions and consequential small slopes, the equation can be reduced to the following shape.

$$\rho A \frac{\delta^2 w(x,t))}{\delta t^2} = \frac{\delta}{\delta x}(T \frac{\delta w(x,t))}{\delta x}) + q_1(x,t)) \tag{5.2}$$

In which:
$T(x,t)$ = Tensile force $[N]$

The latter relation might be hard to read, but in fact it is relatively simple if it is converted into less mathematical terms. When re-writing the equation, Newton's second law is recognized.

$$ma(x,t) = T(x,t)\kappa(x,t) + q_1(x,t) \tag{5.3}$$

In which:
m = Mass $[N]$
a =Transverse acceleration $[m/s^2]$
$\kappa(x,t)$ = Curvature of the member $[m^{-1}]$

The final obtained equation 5.2 is a partial differential equation describing small vibrations of the string about its equilibrium position. This equation can predict the string response both to initial conditions and external loading, provided that the predicted vibrations do not violate the assumption of small transverse string motions.
Note that the tension can be a function of the coordinate x, which in the case of this research will become helpful.

Bending of a beam
Newtons second's law provides the EOM for a bending beam.

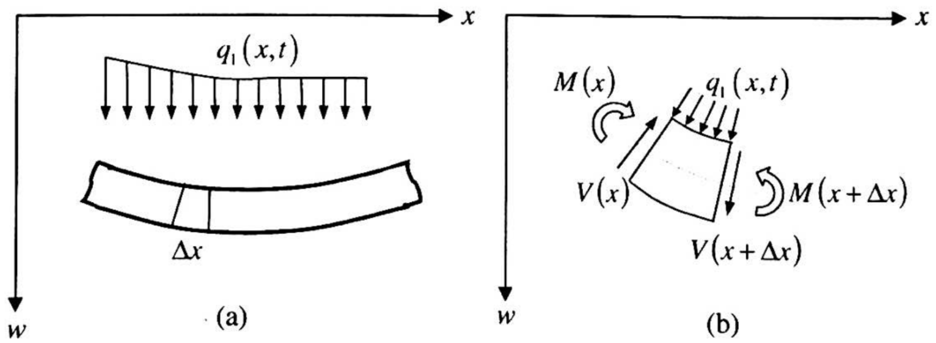

Figure 5.4: (a) Beam undergoing transverse motion and (b) differential element of the beam subject to the shear force, bending moment and external load

$$\rho A \Delta x \frac{\delta^2 w}{\delta t^2} = -V(x) + V(x+\Delta x) + q_1 \Delta x \tag{5.4}$$

In which;
$V(x)$ = Shear force $[N]$

The basic hypothesis of the Euler-Bernoulli theory of beams implies that the intially perpendicular plane cross-sections of the beam remain plane and perpendicular to the neutral axis during bending. As a result, the longitudinal strains vary linearly across the element, which implies that in case of elastic behaviour, the neutral axis of the beam passes through the centroid of the cross-section.
According to this theory the bending moment and curvature are related as:

$$M = -EI\frac{\partial^2 w}{\partial x^2} \tag{5.5}$$

In which:
M = Bending moment $[Nm]$
E = Young's modulus member $[N/m^2]$
I = Moment of inertia member $[m^4]$

By applying Taylor expansion and dividing through delta x, the following relation is obtained.

$$\rho A \frac{\delta^2 w(x,t)}{\delta t^2} + \frac{\delta^2}{\delta x^2}(EI\frac{\delta^2 w(x,t)}{\delta x^2}) = q_1(x,t) \tag{5.6}$$

Like in the previous paragraph, the latter relation might be hard to read, but in fact it is relatively simple if it is converted into less mathematical terms. When re-writing the equation, Newton's second law is recognized.

$$ma + EIV = q_1 \tag{5.7}$$

Relation 5.6 governs transverse motions of a structural element as it responds to external loading and initial conditions. The application of this relation is constraint by the requirements that the slopes of the element are small, the rotational inertia effects are neglected and the Euler-Bernoulli assumptions are not violated significantly.

Transverse motion of a tensioned beam
In case of a curved pipe pull operation, one can neglect neither bending nor tension in the calculation of the restoring force. To obtain the EOM of the transverse motion of this tensioned beam, the most economical approach is to combine the EOM for the beam and the string. The EOM of the taut string can be considered as that of the beam with the restoring force of the bending stiffness neglected. Likewise, the EOM of the bending beam can be considered of that of a taut string with the associated force of the tension neglected.
Thus, to account for these restoring forces simultaneously, one can add the missing restoring term to the relations. In both cases, the result reads as follows.

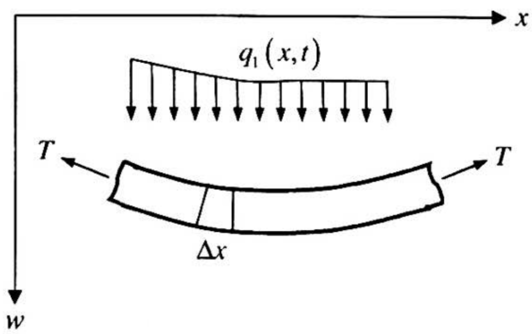

Figure 5.5: Tensioned beam, subject to tension and external load

$$\rho A \frac{\delta^2 w(x,t)}{\delta t^2} + \frac{\delta^2}{\delta x^2}(EI \frac{\delta^2 w(x,t)}{\delta x^2}) = \frac{\delta}{\delta x}(T(x,t) \frac{\delta w(x,t))}{\delta x}) + q_1(x,t) \tag{5.8}$$

When rewriting the equation into less mathematical terms, we can still observe Newton's second law.

$$ma(x,t) + EIV(x,t) = T(x,t)\kappa(x,t) + q_1(x,t) \tag{5.9}$$

Equation 5.8 is the relation for the transverse motion of tensioned beams. If the beam is not tensioned but axially compressed, the tensile force should be replaced by a compressive force with a negative sign.

5.1.2. Defining model parameters

Equation 5.8 consists all components we desire for our engineering model. However, this does not imply that it can be copied one-to-one to be used for examining the behaviour of partially embedded pipelines. While the relation for bending beams is acquired for the vertical pane, pipelines are expected to curve in the horizontal pane. The orientation has rotated ninety degrees, one could say. Consequences of the latter are discussed in this subsection, which will guide towards the final model in the next subsection.

Gravity term Although the weight has a substantial influence on curved pipe pull operations, the first gravitational mass term ρA of equation 5.8 is acting in the vertical pane while we assume an horizontal bending model. Therefore the first term can be neglected. The specific weight of the pipeline is taken into account by means of the P(Y) model.
Lateral accelerations are assumed to be negligible, since the axial pull processes are slow (maximum of ≈ 0.05 m/s) and the lateral velocities of the pipeline are equal to a minor fraction of that velocity.

Bending stiffness term The bending stiffness term EI in the equation is assumed constant over the complete pipeline length and is determined according the relations in Chapter 2.

Tensile force term The tensile force $T(x,t)$ in the member is assumed to regress linearly based on Coloumb friction model, discussed in section 2.2.1. This implies that the tensile force is zero at the start of the pipe and will linearly run up to the axial pull component at the pull head. Potential discrepancies of the Coulomb friction in the curved trajectory of the pipeline compared to the friction of straight sections are neglected. Based on the Coulomb friction model there is no suspicion that the friction in the curved trajectory is different from a straight trajectory, and during the physical test phase this was not observed either. It should be noted that the future curvatures of submerged curved pipe pull operations will be extremely mild.

Distributed load term The distributed load acting on the horizontally bending pipeline $q_1(x,t)$ is mobilized by the sand in which it is partially embedded. The lateral load can be prescribed as a distributed load which it is far from constant over length. As discussed in chapter 2: lateral soil resistance acting on the pipeline is dependent of the lateral displacement of this pipeline. The lateral influence of the surrounding sand on the partially embedded pipeline is captured in the P(Y) model, presented in section 2.2.2.
By replacing the distributed load term $q_1(x,t)$ by the P(Y) term, the lateral soil loads on the pipeline are taken into account.

5.1.3. Final model

After combining the EOM of the transverse motion of a tensioned beam with the defined model parameters, the final relation that is used to examine curved pipe pull operations is obtained. Please note that, according to the differently orientated bending pane, the w(x,t) is replaced by Y(x).

$$EI\frac{\delta^4 Y(x)}{\delta x^4} = \frac{\delta}{\delta x}(T(x,t)\frac{\delta Y(x))}{\delta x}) + P(Y(x)) \tag{5.10}$$

If equation 5.10 is analyzed, one can observe that the tensile force term and the lateral soil reaction term have a restoring character on the lateral motion of the partially embedded pipeline.

One might also have noticed that the time-dependency of the pipelines bending behaviour is deducted. Since the dynamical behaviour of curved pipe pull operations is extremely difficult to examine with a programmed numerical model and pull velocities/accelerations are low, the computations within this research are based on the steady-state response of the partially embedded pipeline.

5.2. Numerical model solution

Due to the non-linear character of the lateral soil resistance: the system of equations evolving from the relation 5.10 cannot be solved by algebra. The system needs to be solved by means of a numerical approach.

5.2.1. Central-Difference method

Numerical methods are used to approximate the outcome of differential equations. The Central-Difference method is a method that can be used to determine derivates of a certain parameter, Vuik (2016). Numerical methods approximate the solution in a certain location by taking into account the influence of the solution at locations that are one, or multiple quantified step sizes away from that point.

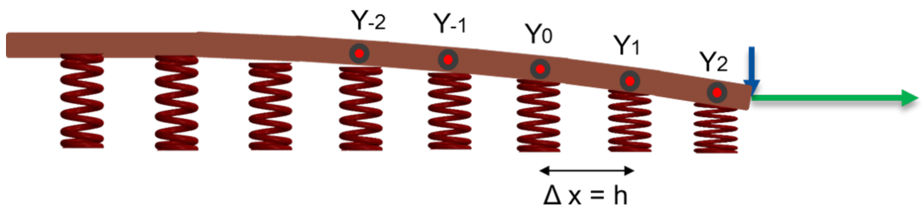

Figure 5.6: Schematization of numerical solutions and step sizes of a tensioned bending beam

The Central-Difference method enables us to approach the solution of the lateral displacement of the pipeline. First; the pipeline is divided into a system of communicating nodes with intermediate distance h. By replacing the partial derivatives in equation 5.10 by the approximate Central-Difference equations, displayed in figure 5.7, it enables us rewrite the equations for the different nodes into a system of differential equations.

Central-Difference Formulas of Order $\boldsymbol{O}(h^2)$

$$f'(x_0) \approx \frac{f_1 - f_{-1}}{2h}$$

$$f''(x_0) \approx \frac{f_1 - 2f_0 + f_{-1}}{h^2}$$

$$f^{(3)}(x_0) \approx \frac{f_2 - 2f_1 + 2f_{-1} - f_{-2}}{2h^3}$$

$$f^{(4)}(x_0) \approx \frac{f_2 - 4f_1 + 6f_0 - 4f_{-1} + f_{-2}}{h^4}$$

Figure 5.7: First to fourth order derivatives of function $f(x_0)$ by Central-Difference method

Where the subscript of Y denotes the location of the node, and the respective order of other nodes on the pipeline. The relation at location Y_0 now holds:

$$EI\frac{Y_{-2} - 4Y_{-1} + 6Y_0 - 4Y_1 + Y_2}{h^4} = T\frac{Y_{-1} - 2Y_0 + Y_1}{h^2} - Fbr * tanh(Cy * Y_0) \tag{5.11}$$

If the pipeline is divided into n steps; a total amount of n+1 nodes is obtained. For every node, except the two outer boundary nodes, an equation as example equation 5.11 is set up.
The final system of non-linear differential equations contains n-1 equations. Combined with two boundary conditions; the system can be solved and the behaviour of the partially embedded pipeline under an inclined pull load can be predicted.

5.2.2. Boundary conditions

The numerical system of equations requires two boundary conditions in order to work properly. The two imposed boundary conditions are stated in the two forthcoming paragraphs.

Kinematic boundary condition at shore side pipeline At the shore side of a pipe pull a natural kinematic boundary condition arises; because the lateral displacement of the pipeline at the firing lane is zero. The size of the numerical steps between nodes should be chosen such that the total model length model is not too short to comply with the boundary condition at the origin.

Kinematic boundary condition at pull head side At the pull head side of the pipeline the allowed displacement needs to be inserted by the user of the model. Within the next section the user can find guidance on how to chose this kinematic boundary condition on the pull head side of the pipe. Like for the boundary condition on the origin of the pipeline: the size of the numerical steps between nodes should be chosen such that the total length of the model is not too short to comply with the boundary condition at the pipe end.

5.3. Predicting pull curves

As mentioned before during this chapter; the extend to which partially embedded pipelines can be pulled during a pull operations will be determined by means of the steady-state response of the system that is modeled. This means that we have to compute model predictions based on assumptions that we can prove.

The boundary condition at the origin of the pipeline never changes; and therefore does not change in influence on the pipeline behaviour. However; the boundary condition on the pull head can be chosen as more or less desired. In the following subsection; the kinematic condition at the pull head is defined for two different manners of curved pipe pull installation.

5.3.1. Controlled pull behaviour

At the start of this research; the focus was to create te installation method in which the pipeline would be installed into a curved trajectory as controlled as reasonably possible. Once the light lateral pipe behaviour was encountered (like prescribed in Chapter 2); the perception arised that the pipeline should be maintained in his embedment during the curved pull, in order to obtain the most controlled installation technique. The final prediction of the pull radius is computed by running the static model with a pull head displacement according this subsection. The underlying idea is that if the pipeline will be stable during this particular curvature, it is possible to pull into that same curvature after.

Because we choose to keep the pipeline embedded during installation; we have to examine within which circumstances it will. From the paper of Wang et al. (2018) and the experiments conducted within this research; it can be concluded that pipelines remain embedded at major part of their initial embedment if they are not displaced more than one and a half pipe diameter. This can be observed in figure 5.8.

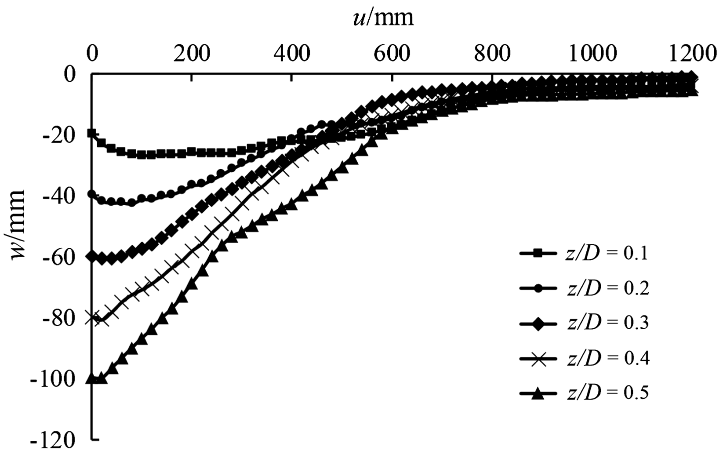

Figure 5.8: Y/Z Displacement of laterally loaded pipelines (D_0=200mm, L=1000mm and W=402N) for different initial displacements, from the research of Wang et al. (2008)

As it is important to control the operation as much as possible, a conservative value is chosen for the boundary condition at the pull head. The boundary condition comes from the DNV and links the lateral displacement to the decreasing lateral reaction of the soil. Although our created P(Y) model, due to the tangent hyperbolic origin, stays constant for large lateral displacements; in reality the maximum lateral force decreases for larger displacements of the pipeline. This behaviour is shown by an example in figure 5.9.

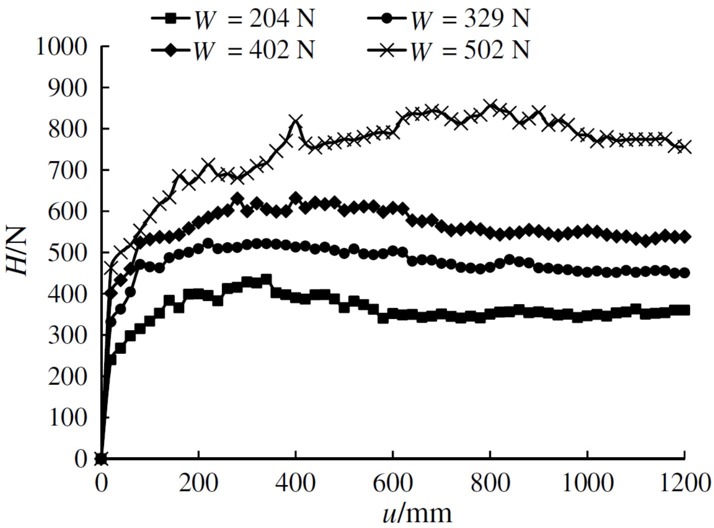

Figure 5.9: Soil resistance curves of laterally displaced pipelines (D_0=200mm and L=1000mm) with z/D = 0.2 and different pipe weights, from the research of Wang et al. (2008)

After a displacement of multiple diameters; a slight decrease of the soil reaction is visible. The stabilized resistance that is obtained after a lateral break out is called the residual lateral resistance. DNVGL-RP-F114 (2017) provides estimates for the mobilization displacement that is required to reach this residual resistance. These estimates can be found in figure 5.10. The mobilization distances that are used to estimate the displacement for residual strength conditions are in line with those used to estimate that of the breakout mobilization distance of our P(Y) model.

Parameter	*Uncertainty case*	*Typical values*
y_{res}	Low estimate, LE	$\frac{y_{res}}{D} = 0.6$
	Best estimate, BE	$\frac{y_{res}}{D} = 1.5$
	High estimate, HE	$\frac{y_{res}}{D} = 2.8$

Figure 5.10: Lateral mobilization displacement to residual resistance estimates, DNVGL-RP-F114 (2017)

After examining the different mobilization uncertainty cases of the DNV and comparing them to the results of Wang et al. (2018) and the conducted curved pipe pull tests within this research; the best estimate of DNV (1.5D) shows the best match. Therefore the value of 1.5D is used as boundary condition to predict the minimum radius of partially embedded pipelines during a controlled pull-out.

An elaborate validation of the numerical model predictions of controlled curved pull operations is described in section 6.1 of the model validation chapter 6.

5.3.2. Breakout pull behaviour

Although the created model was preliminary designed to compute the controlled minimum pull radius of partially embedded pipelines; it should also give an accurate estimate of the behaviour for situations in which the pull head is forced to a break out merely into the lateral direction. The risk of discrepancies appears in the fact that our P(Y) model does include the effect of decreasing soil resistances, which play a role in large lateral pipe displacements. Given that this decrease seems to be marginal and the P(Y) model seems to underestimate the lateral stiffness of the soil slightly (conservative approach of soil strength); the model might give relatively well predictions for a pull head displacement that exceeds the lateral pipe head displacement of the residual mobilization displacement.

An elaborate validation of the numerical model predictions of breakout pull behaviour is described in section 6.2 of the model validation chapter 6.

6

Model validation and value for application

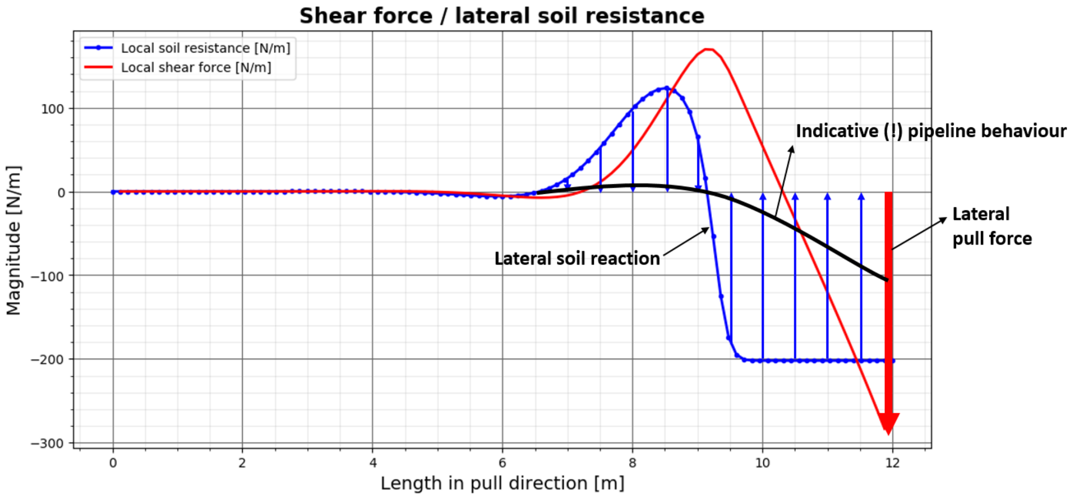

Figure 6.1: Combined plot of the shear force and lateral soil resistance as function of lateral pipeline displacement

Within this chapter the numerical model is validated by means of the physical model tests that were conducted during the research. At first, the controlled pull behaviour is discussed. After the controlled pull behaviour, the behaviour during a forced breakout is examined. The experimental data used within this section is based on a total of 28 controlled pull tests and 2 forced breakout pull tests, which are described in chapter 4 and the appendices.

After the validation of the numerical model, the prediction capabilities of the model are entailed by means of experimental examples. These examples give an important insight into the processes that play a role if a pipeline is pulled into a curved trajectory. The model is applied on the target pipeline (described in subsection 3.3.1) and the influence of the different parameters is elaborated. A brief summary of the findings within this chapter is enclosed to conclude.

6.1. Controlled pull behaviour validation

As described in chapter 3 and 4, the pull forces and radii are logged throughout the experiments. A summary of the results of the thirty controlled curved pull experiments of the testing campaign is displayed within table 6.1. Within appendices A, B and C, elaborate summaries of all experiments are enclosed. Throughout table 6.1 the predicted minimum pull radius and predicted maximum lateral are plotted against the values that were observed within the experiments.

Throughout the physical experiments, three different classifications of pipeline behaviour where examined. To analyze the conducted tests more elaborately, results are examined by coupling the experimental data to the observed pipeline behaviour. The three different classifications are prescribed within the next subsection.

Test model	$W[kg/m]$	Test No.	$z/D[-]$	$R_{exp}[m]$	$R_{pred}[m]$	$F_{lat,exp}[m]$	$F_{lat,pred}[m]$	Classification
50/1.8	1.36	1	0.40	29.61	32.44	2.65	2.67	Critical
50/1.8	1.36	2	0.30	37.08	37.62	4.00	2.26	Breakout
50/1.8	1.36	3	0.45	27.14	32.44	2.86	2.94	Critical
50/1.8	1.36	4	0.45	27.09	32.44	3.32	2.94	Critical
50/1.8	1.36	5	0.30	33.22	37.62	2.70	2.26	Critical
50/1.8	1.36	6	0.20	42.16	49.14	1.81	1.77	Critical
50/1.8	1.36	7	0.15	45.70	55.48	2.20	1.47	Critical
50/1.8	1.36	8	0.30	34.83	37.62	3.35	2.26	Breakout
50/3.2	0.96	1	0.45	25.59	37.62	1.78	3.34	Moderate
50/3.2	0.96	2	0.45	32.17	37.62	3.55	3.34	Breakout
50/3.2	0.96	3	0.35	46.28	43.19	2.35	2.65	Breakout
50/3.2	0.96	4	0.30	48.54	49.14	2.30	2.40	Breakout
50/3.2	0.96	5	0.40	32.31	43.19	2.81	2.94	Breakout
50/3.2	1.29	1	0.10	74.60	76.79	2.34	1.42	Breakout
50/3.2	1.29	2	0.45	32.31	37.62	4.32	3.34	Breakout
50/3.2	1.29	3	0.20	50.93	62.20	3.27	1.71	Breakout
50/3.2	1.29	4	0.25	39.63	55.48	3.39	2.26	Breakout
50/3.2	1.62	1	0.40	30.26	43.19	3.13	3.24	Critical
50/3.2	1.62	2	0.45	29.64	37.62	3.99	3.43	Critical
50/3.2	1.62	3	0.15	55.08	62.20	4.31	1.86	Breakout
50/3.2	1.62	4	0.45	29.64	37.62	2.05	3.43	Moderate
50/3.2	1.62	5	0.45	27.72	37.62	2.87	3.43	Critical
50/3.2	1.62	6	0.30	39.06	49.14	2.91	2.65	Critical
50/3.2	1.62	7	0.20	40.31	55.48	2.86	2.11	Critical
50/3.2	1.62	8	0.20	47.34	55.48	2.01	2.11	Critical
110/3.2	8.40	1	0.15	52.97	63.59	15.21	14.72	Critical
110/3.2	8.40	2	0.15	43.94	63.59	19.14	14.72	Breakout
110/3.2	8.40	3	0.10	52.58	73.37	11.97	12.36	Critical

Table 6.1: Fundamental parameters summary of the controlled curved pull experiments

6.1.1. Classifications

The twenty-eight controlled pull tests are subdivided into three different classifications:

1. Moderate curved pulls (2 experiments)
2. Critical curved pulls (14 experiments)
3. Breakout curved pulls (12 experiments)

Moderate curved pulls Although the aim of the physical test campaign was to pull all models to their controlled curve limit, in practice this was not always achieved. In two experiments the model pipeline was certainly not pulled up to the minimum radius, since the maximum lateral pull force was not reached. An example of such a pull can be observed in figure 6.2.

In the example figure, a detailed view of the location where the model experienced the start of a inclined pull (as described in section 4.1.1) is shown. One can observe a small distortion on the outer bend side of the plowed soil, but the pipeline was able to continue being pulled into a curve without leaving her embedment.

Figure 6.2: Moderate pull example of the D_0 50mm (t=3.2mm and W=0.96kg/m) model pipeline, test 1

Critical curved pulls In the next classification, prescribed as the critical curved pulls, the pipelines where pulled to an extend that almost caused the soil surrounding the pipeline to fail. Of course this is subjective in a way, but during these experiments there always was a clear displacement of the pullhead before the pipeline continued into the curved pull trajectory without leaving her embedment. Due to the latter, a critical curved pull can clearly be distinguished from the other two classifications. An example of a critical classified pull is shown in figure 6.3.

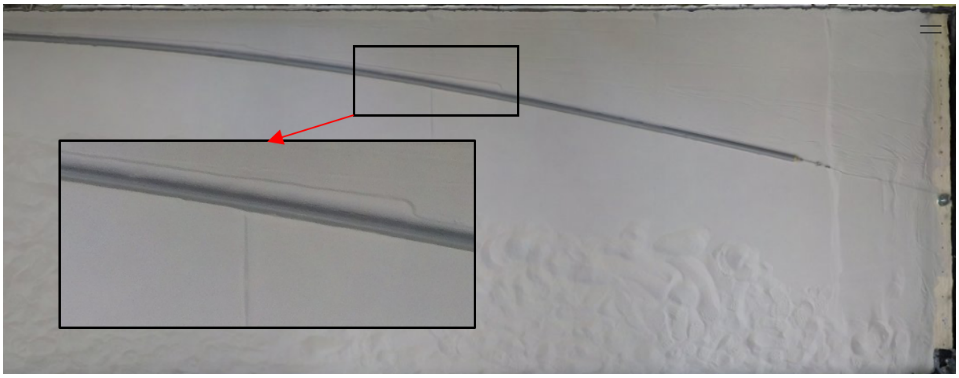

Figure 6.3: Critical pull example of the D_0 50mm (t=1.8mm and W=1.36kg/m) model pipeline, test 4

Breakout curved pulls The last classification consists of model pipelines that are pulled such that the capacity of the surrounding soil was eventually exceeded. Failure of the sand occurred, which caused the model pipeline to leave her embedment. An example of a breakout curved pull is shown in figure 6.3. The curve that is used to determine the minimum radius of the controlled pull is captured by the sand and is visible by means of the dashed line.

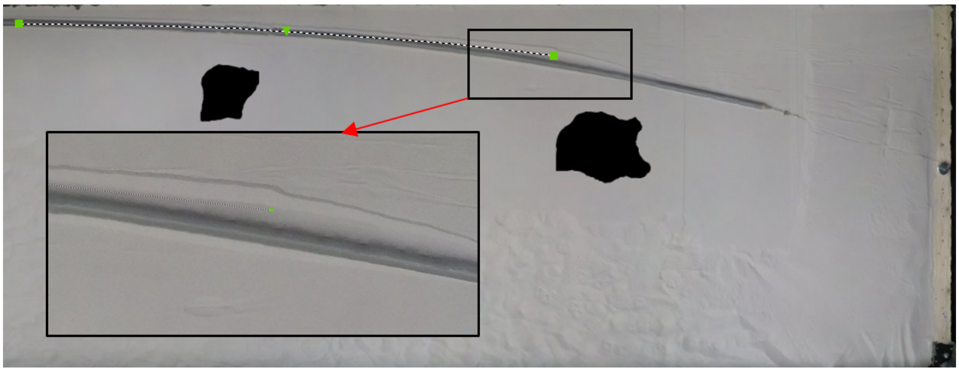

Figure 6.4: Breakout curved pull example of the D_0 50mm (t=1.8mm and W=1.36kg/m) model pipeline, test 8

6.1.2. Comparison of model radii predictions and obtained experimental radii

Plotting the numerical computations of the model pipelines in the same graphs as the experimental data (discussed in section 4.3), enables to visually compare the data of the two. Throughout the following five graphs, the results of the latter can be observed.

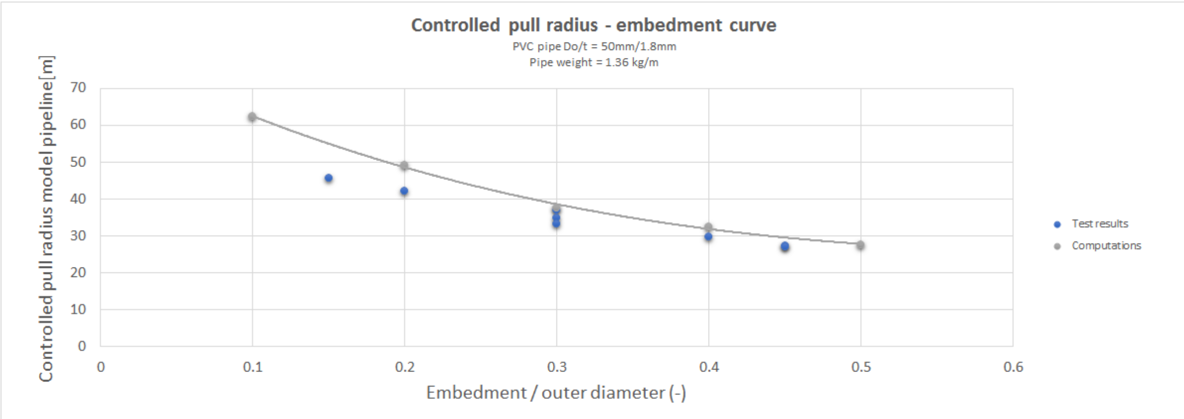

Figure 6.5: Comparison of model predictions and associated test results of the D_0 50mm (t=1.8mm and W=1.36kg) model pipeline

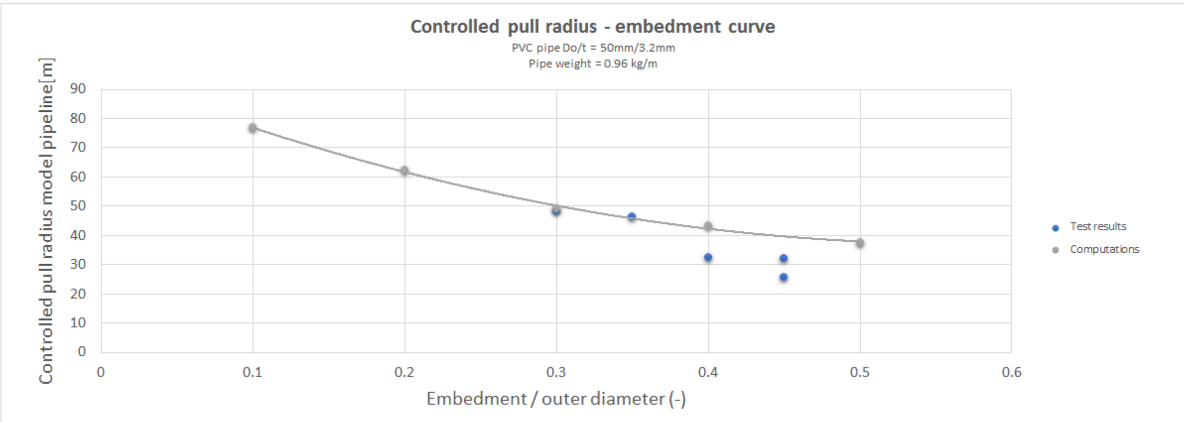

Figure 6.6: Comparison of model predictions and associated test results of the D_0 50mm (t=3.2mm and W=0.96kg/m) model pipeline

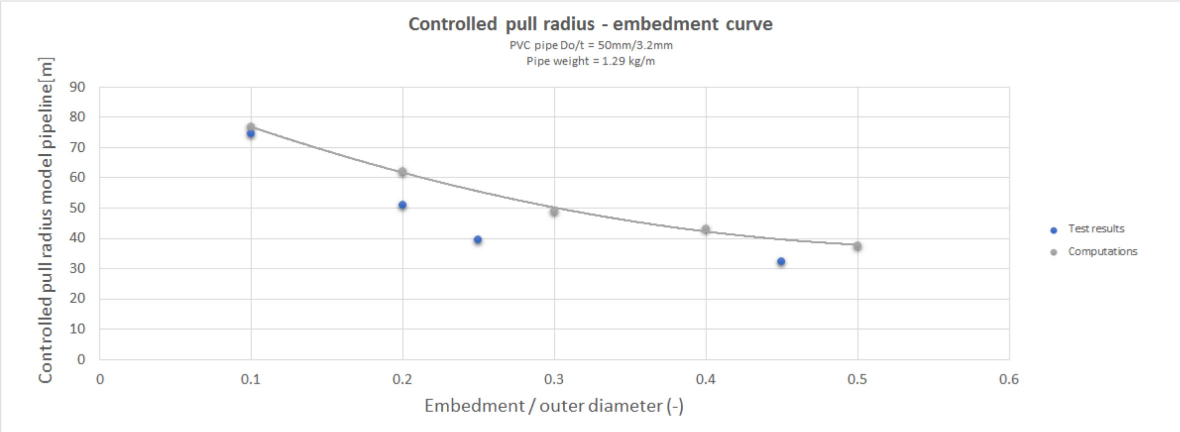

Figure 6.7: Comparison of model predictions and associated test results of the D_0 50mm (t=3.2mm and W=1.29kg/m) model pipeline

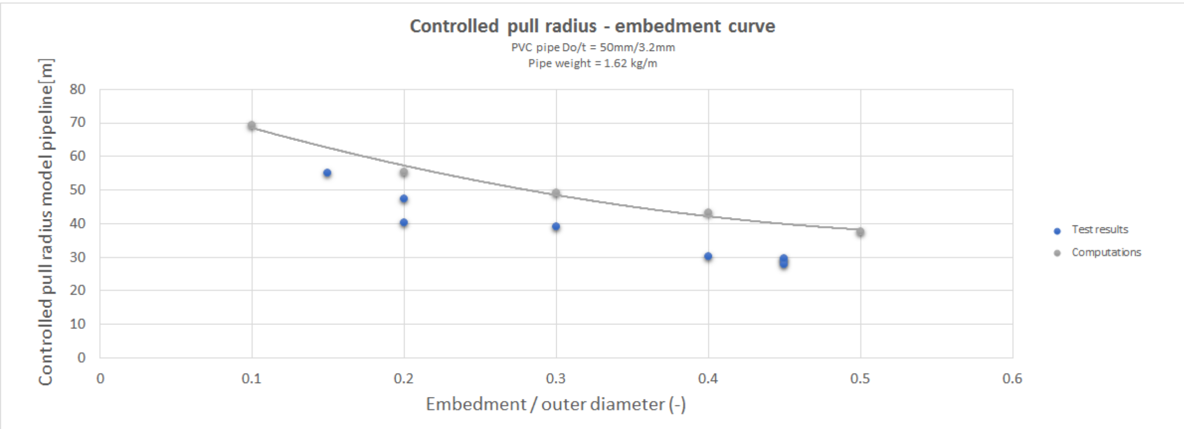

Figure 6.8: Comparison of model predictions and associated test results of the D_0 50mm (t=3.2mm and W=1.62kg/m) model pipeline

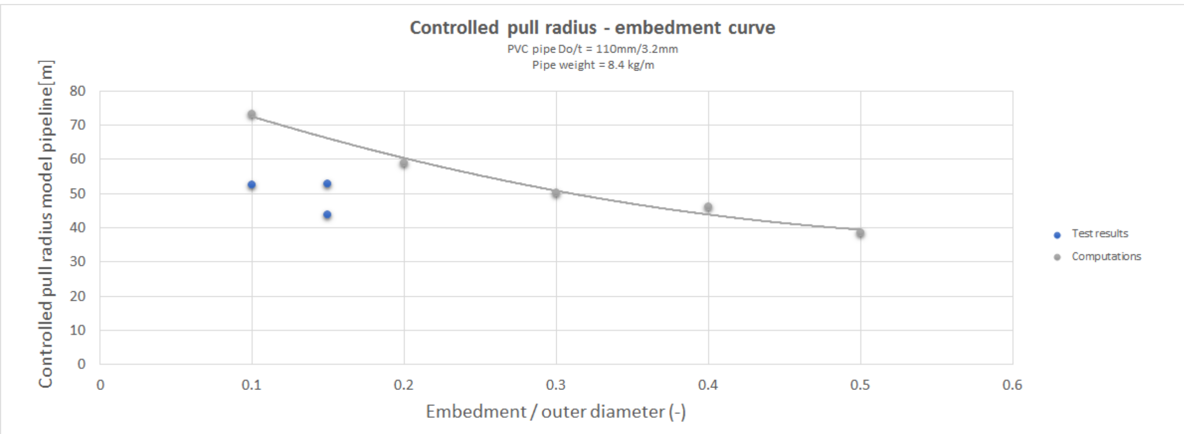

Figure 6.9: Comparison of model predictions and associated test results of the D_0 110mm (t=3.2mm and W=8.4kg/m) model pipeline

Numerical model computations of the controlled pipe pull behaviour pretend to give an upper bound solution of the acceptable pull radius observed during the controlled physical model tests. This implies that the model prediction is a relatively conservative approach of the radii in which a pipeline can actually be pulled.

None of the test pipelines was pulled into a radius that was substantially larger than the expected in the predictions. One can conclude that the model gives a relatively safe prediction of the extend to which pipelines can be pulled into curved trajectories.

Difference ranges of the radii comparison
Within the diagram of figure 6.10 the observed differences of the predicted pull radii and the obtained physical test pull radii are categorized into defined difference ranges. During the physical model tests, 61% of the models was pulled into a trajectory of which the radius differed less than 20% of the predicted radius. The remaining 39% was pulled into a trajectory that differed between 20 and 32% of the proposed radius.

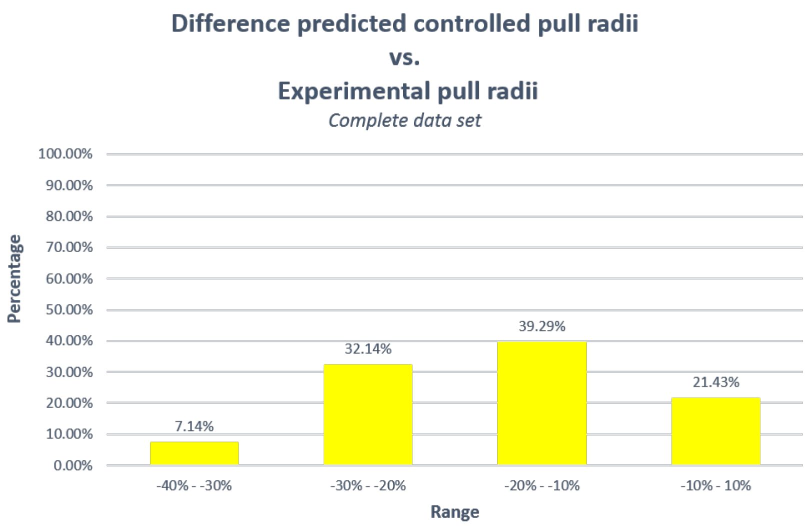

Figure 6.10: Comparison of predicted controlled pull radii and physically obtained controlled pull radii

By extracting the data of the critical curved pulls and the breakout curved pulls into individual graphs (shown in 6.11 and 6.12), an interesting shift in the trend of the difference ranges appears.
Critical curved pulls resulted into pull radii that, on average, subceeded the predicted pull radii more than the obtained breakout pull radii did.

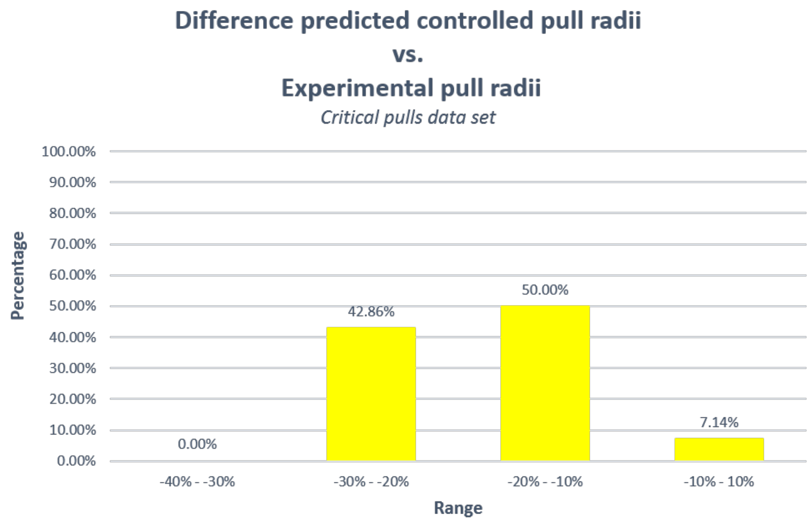

Figure 6.11: Comparison of predicted controlled pull radii and physically obtained controlled pull radii

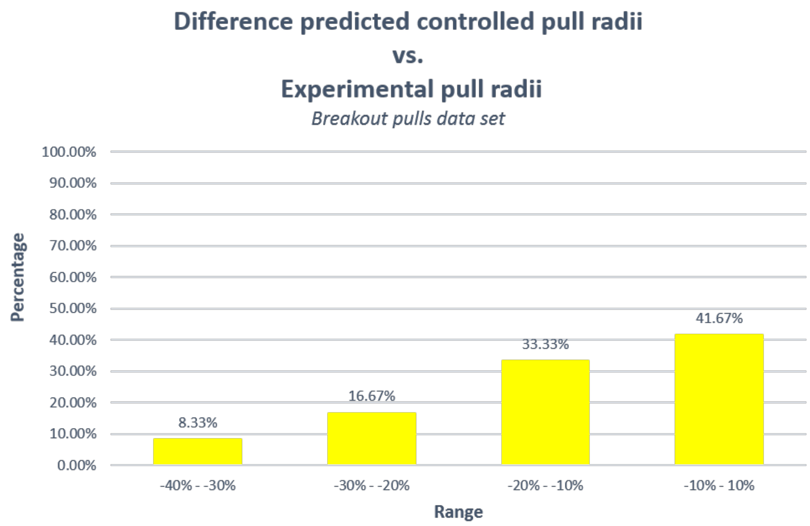

Figure 6.12: Comparison of predicted controlled pull radii and physically obtained controlled pull radii

After analyzing the data within this section one can observe the trend of slight overestimate of the controlled pulled radii throughout the complete set of compared model computations and test results. Resulting from these results, the perception might rise that one or more parameters are not modeled completely correct. Subsection 6.1.4 describes an attempt to clarify the observed discrepancies.

6.1.3. Comparison of maximum lateral pull force predictions and experimental forces

Throughout all experiments the pull forces were logged with the equipment described in chapter 3. By combining the data pull logs with the positioning data of the pipelines throughout experiments; the axial and lateral pull resultants of an experiment can be determined for every specific moment in time.

The lateral component of the pull force is calculated in accordance with the basic hypothesis of the Euler-Bernoulli theory of beams, as prescribed in subsection 5.1.1. The numerical prediction model of this research is based on these assumptions as well. Euler-Bernoulli theory of beams implies that the initially perpendicular plane cross-sections of the beam remain plane and perpendicular to the neutral axis during bending. As a result, the rotation of the pipeline (θ) is neglected, like in the model figures 5.3 and 5.4. A visualization of the model assumption for lateral pull force can be observed by means of the blue arrow in 6.13.

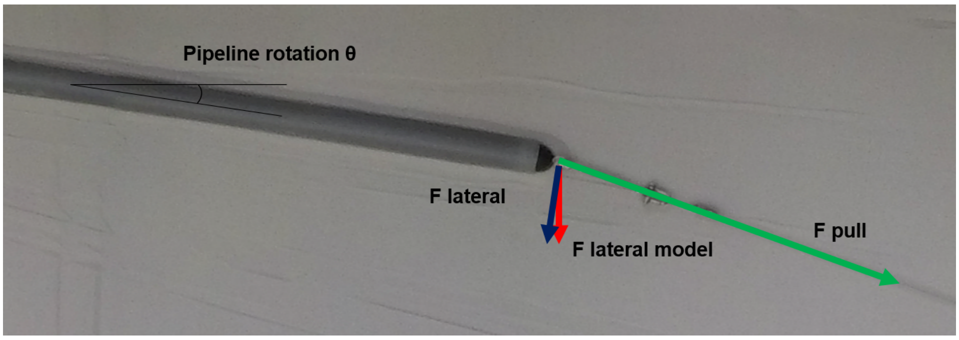

Figure 6.13: Visualization of the actual lateral pull force (in blue) and the model lateral pull force (red)

Difference ranges of the lateral pull force comparison

Within the diagram of figure 6.14 the observed differences of the predicted maximum lateral pull radii and the physically imposed lateral pull forces are categorized into defined ranges. One can observe that in the attempt to pull the model pipelines into the smallest radius possible; 57% of the maximum imposed lateral forces reached a value that differed less than 20% of the predicted maximum lateral force.

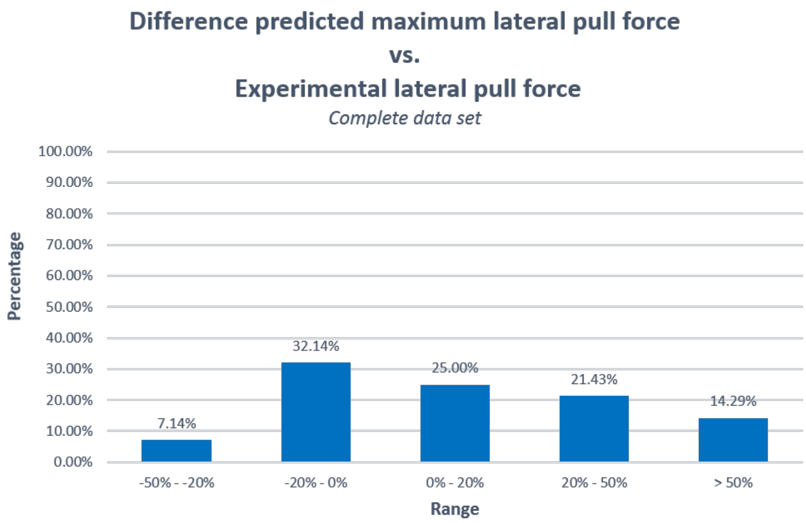

Figure 6.14: Comparison of predicted maximum lateral pull forces and physically imposed lateral pull forces

By extracting the data of the critical curved pulls and the breakout curved pulls into individual graphs (shown in 6.16) and 6.16), another interesting shift in the trend of the difference ranges appears.

Within the classification critical curved pulls (described by figure 6.16), the imposed lateral force during the experiments was within 20% of the maximum predicted force in 86% of the physical tests. From this observation we can conclude that the numerical model is able to predict the maximum lateral pull force with a high accuracy.
For the other 14% of the critical curved pull experiments the soil appeared to have more bearing strength than expected, as the required lateral pull force on the head was 20-50% higher for those cases.

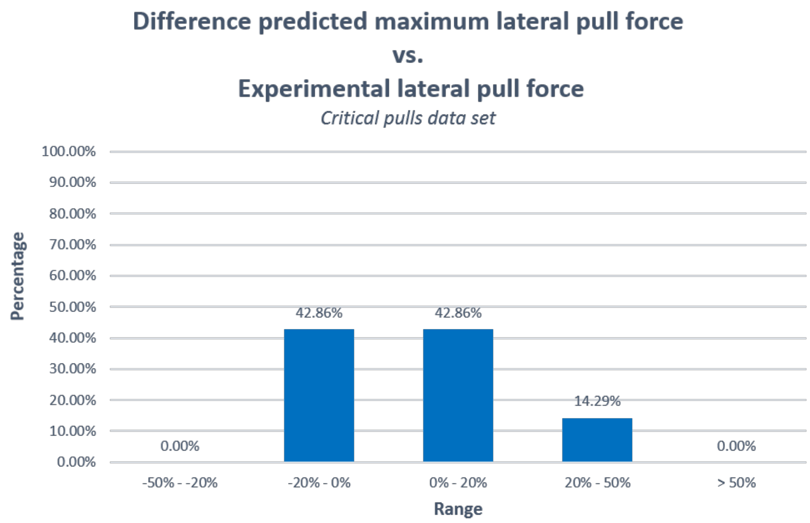

Figure 6.15: Comparison of predicted maximum lateral pull forces and physically imposed lateral pull forces of experiments classified as critical curved pulls

From diagram of curved breakout pulls, displayed in 6.16), one can conclude that 75% of the curved breakouts was expected to appear by the numerical model predictions. Another 25% was likely to happen after the model predictions showed that the physically imposed lateral pull exceeded 80% of the maximum soil capacity. Again, the numerical model was able to predict the behaviour of the pipeline with a high accuracy.

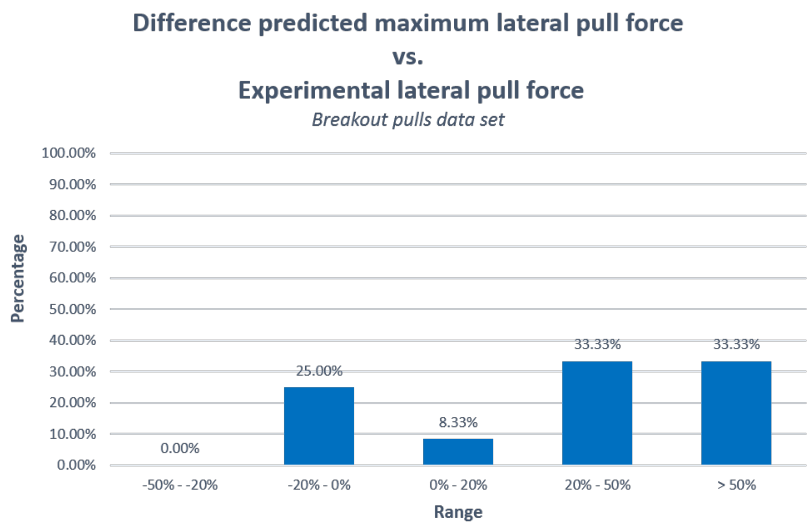

Figure 6.16: Comparison of predicted maximum lateral pull forces and physically imposed lateral pull forces of experiments classified as breakout curved pulls

6.1.4. Clarifying the observed discrepancies

In chapter 3 and 4 discrepancies between the physical test setup and input parameter like pipe stiffness, pipe weight, soil compaction and embedment of the numerical model are minimized as much as reasonably possible. This implies that the discrepancies of the model predictions and experiments would be related to the lateral soil resistance modeling.

As discussed throughout section 6.1.3, the P(Y) model tends to underestimate the lateral soil resistance of partially embedded pipelines by a fraction. By multiplying the breakout force in the P(Y) model with a factor, the model stiffness can be adjusted. Multiple factors (>1) where examined, in order to achieve a better curve fit. In figure 6.17 the comparison between the original P(Y) model and a P(Y) model in which the breakout force is raised with 40 percent is plotted.

The raised lateral stiffness gives an increased fit of the model predictions with the physical test results. The next subsection will give an counterargument to the curve-fit that is obtained within this subsection.

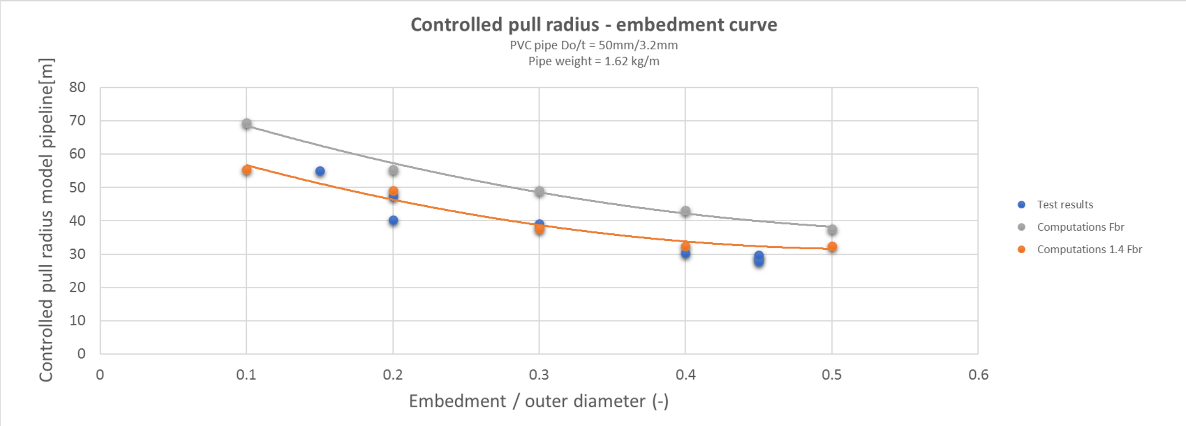

Figure 6.17: Comparison of the original predictions and increased soil stiffness predictions with the associated test results of the D_0 50mm (t=3.2mm and W=1.36kg/m) model pipeline

6.1.5. Concluding the controlled pull validation

Although manually increasing the stiffness of the P(Y) model might give better curve-fits for some comparisons of the model analysis and physical experiments: this does not mean that they hold for all controlled curved pipe pulls. If the stiffness of the P(Y) model is manipulated, some pull radii of the physical tests within this research would be underestimated by their numerical model prediction. Underestimating the pull radius might, in practice, lead to an uncontrolled pull operation.

For an increased fit of the predicted radii curves with the experimental data curves another option would be to optimize the method of the model used to determine the minimum pull radii pipeline. Within this research this is not examined further.

The original P(Y) model gives a well defined upper boundary solution of the expected pull radius that can be obtained during curved pull operations. Given the fact that the critical lateral pull forces are predicted with high accuracy (as concluded in 6.1.3), there is no reason to modify the P(Y) model.

6.2. Breakout pull behaviour validation

By the origin of the model, one might expect it to predict the lateral breakout behaviour of a pipeline with relatively high precision. Based on the comparison of two breakout experiments with two different models, described in section 4.3, one can conclude this is true. A summary of the conducted lateral breakout pulls is enclosed within appendix D.

The lateral displacement of the pipelines was prescribed well until the pipeline started to propagate in axial direction (after the axial pull component exceeded the axial resistance). By means of the 110mm model breakout test we will discuss the validation of the lateral breakout prediction. The model pipeline reached an embedment of 23mm before it was exposed to lateral pull forces.

Figure 6.18: Embedment of the 110mm model pipe before lateral pull, z = 23mm - z/D ≈ 0.21

The computations of the lateral displacement of the model pipe are presented in figure 6.19. One can observe that the model pipeline is expected to find a steady-state after bending over a little more than 4 meter. Mean radius over the bend is equal to 41.54 meter (not displayed in the graph but given by the numerical model).

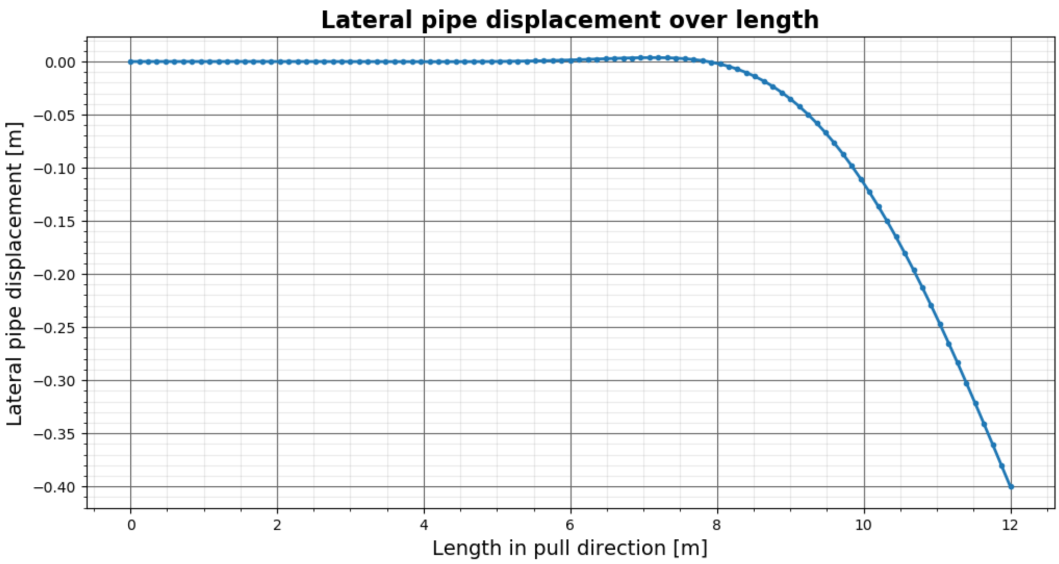

Figure 6.19: Model predictions of the 110mm model pipeline, based on 0.40m pipeline head displacement

If we compare the displacement of the numerical model predictions with the actual lateral displacements obtained during the physical test shown in figure 6.20, one may conclude that the model works and gives a decent representation of a lateral break out. The same conclusion can be drawn from the 50mm model breakout test, summarized in figure D.2, as well.

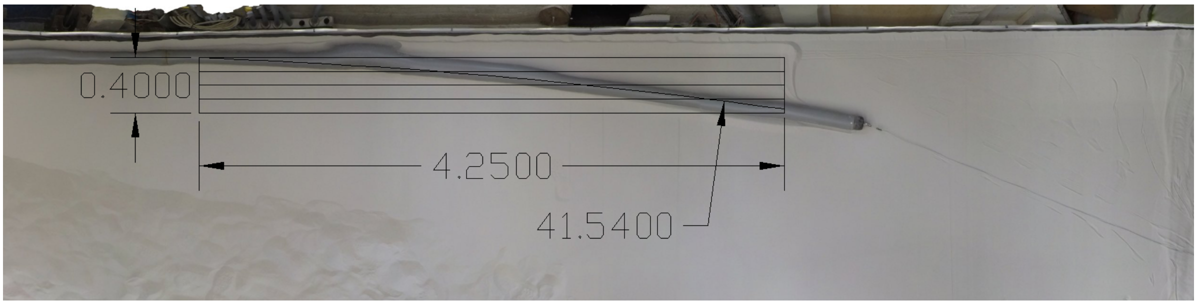

Figure 6.20: Forced breakout test of the 110mm model pipeline, matching the model computations

6.2.1. Prediction of lateral pull force during a breakout

The predicted lateral pull forces of the numerical model represented the actual lateral pull forces of the (well scaling) 50mm model physical test relatively good. On the other hand, the predicted lateral pull forces of the 110mm model pipeline showed slightly underestimated values of the force that was imposed during the physical model test.

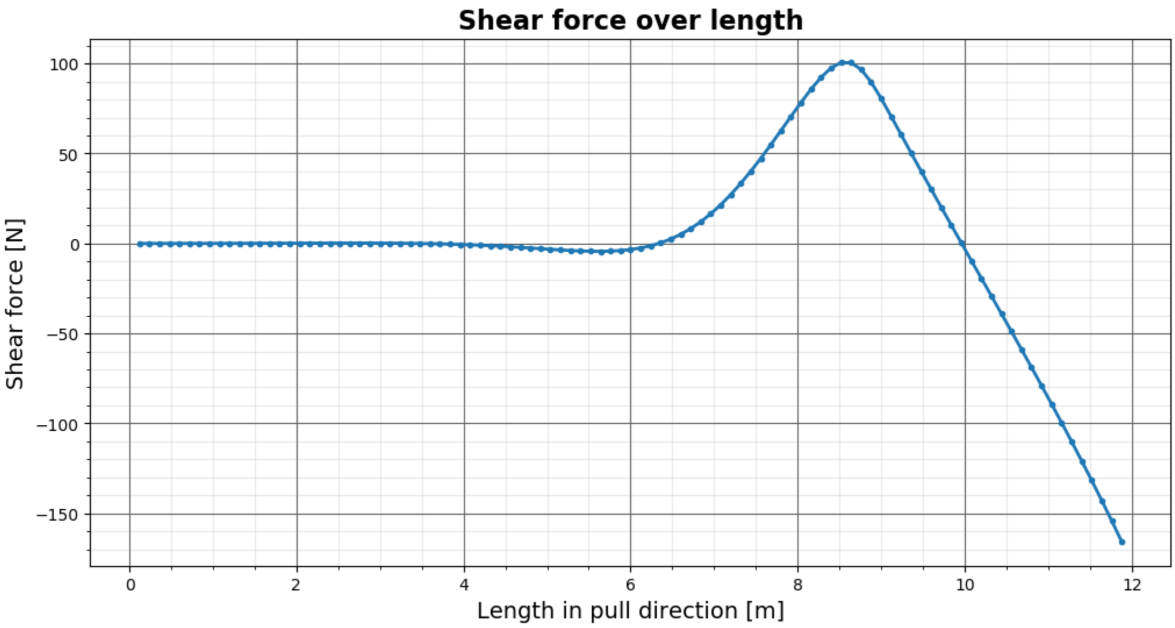

Figure 6.21: Shear force computation of the 110mm test model under a pipe head displacement of 2D

The lateral component of the pull force is equal to the shear force on the pipe head. During the process of a lateral breakout, the shear force at the head of the pipeline varies. From the latter, we can conclude that the lateral pull force is dependent of displacement and time. The required lateral pull force increases for larger pipe head displacements.

To evaluate the physical test results in a correct and precise manner, the lateral pull force was examined for different pipe head displacements (which increased in time). The results of this comparison are plotted in 6.22. The fact that the numerical model uses the maximum design value of lateral soil resistance may again play a role in the slight underestimate of the required lateral pull force.

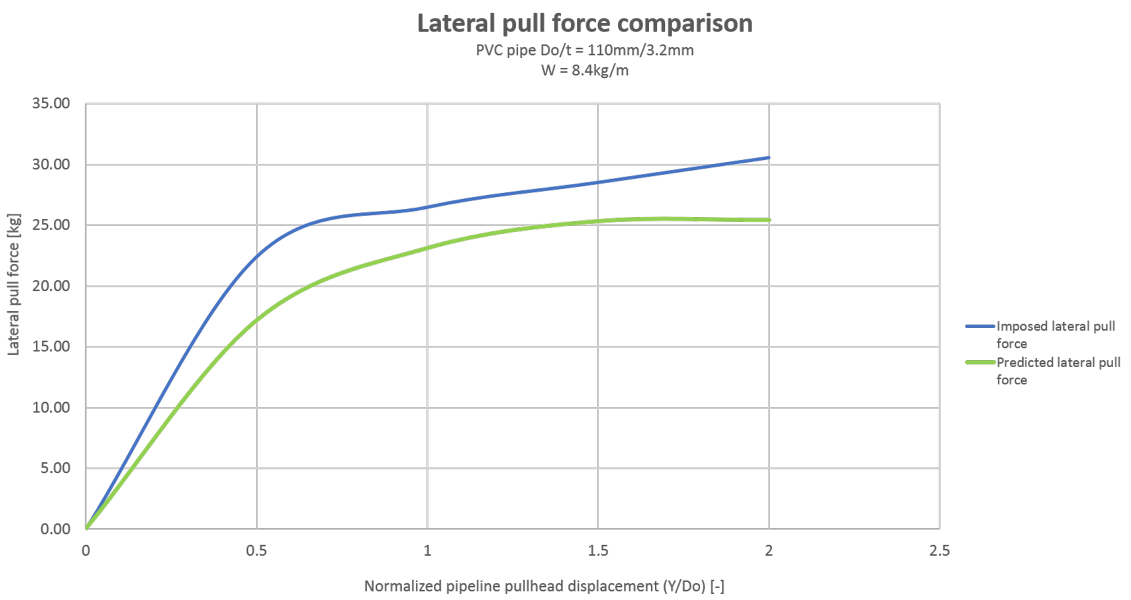

Figure 6.22: Comparison of computed and actual lateral pull head forces of 110mm pipeline breakout

6.2.2. Axial friction validation

In Chapter 2 and onward, the axial friction is modelled according Coulomb friction (described in section 2.2.1). By comparing the friction computation of equation 6.1 of the best scaling D_0 50mm pipeline with the pull graph displayed in figure 6.23 we can conclude that the applied friction factor of 0.6 holds during this specific experiment.

$$F_f = \mu WL = 0.6 * 1.29 * 9.81 * 12 = 9.29[kg] \tag{6.1}$$

In which:
F_f = Friction force $[N]$
μ = Friction factor $[-]$
W = Weight pipeline $[N]$
L = Model pipe length $[DEG]$

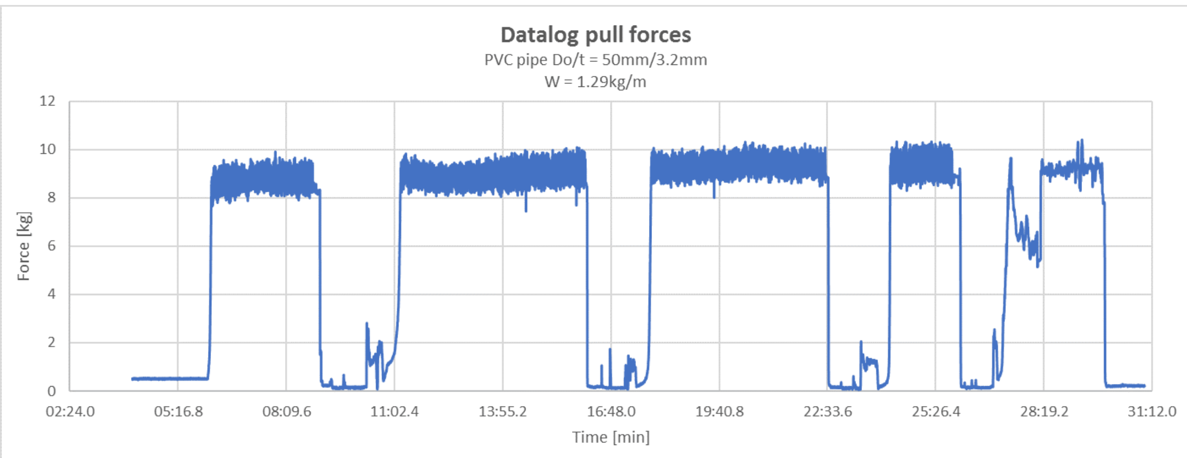

Figure 6.23: Datalog pull forces D_0 50mm (t=3.2mm and W=0.96kg/m) model pipeline

Negligible curve friction gain validation The numerical model that is created during this research assumes that the axial friction of the pipeline does not increase if a pipeline is pulled into a curved trajectory. Figure 6.24 shows a pull angle of 10 degrees, at the start of the fourth curved pull.

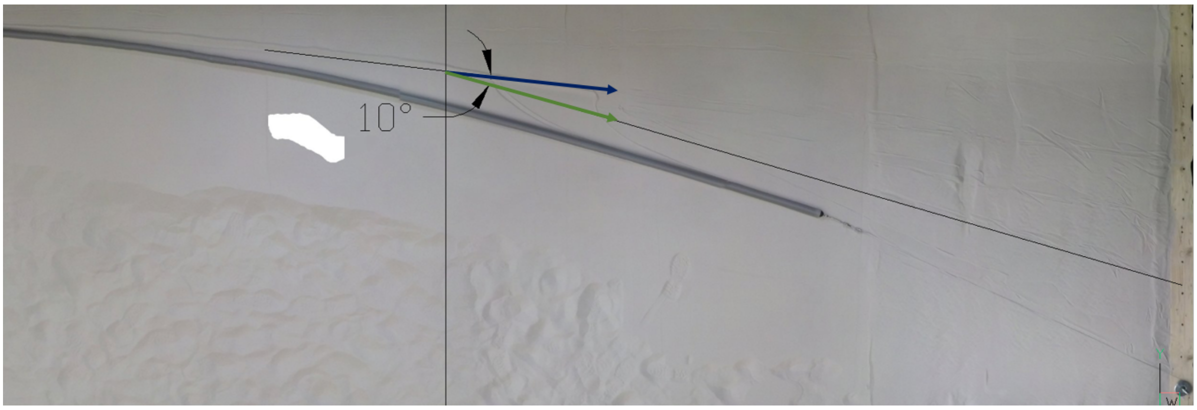

Figure 6.24: Axial component of the pull force (blue) during the start of the fourth curved pull

The axial component of the pull force (visualized in blue) is equal to the cosine of the pull angle times the pull force. Please not that this model value, in contradict to the model value of the lateral force (described per 6.1.3), is equal to the actual axial component of the pull force. This results in an axial force which is equal to 98 percent of the pull force. In the pull force datalog there is only a small increase of the pull force, which confirms the assumption that a mild curved pull does not result in severe pull force gain compared to a straight trajectory.

6.3. Scaling up to target pipeline computations

After the validation of the non-linear numerical model computations it is possible to answer the main research question. By applying the model to the target pipeline (prescribed by 3.3.1) we will observe the safe limit of the extend to which the pipeline can be pulled into a curve.

Project case Let us assume that we have a project case in which we want to install the target pipeline, as prescribed in table 3.2. The client requests a nearshore pipeline trajectory that leaves the coast in a straight 1000 meter course, after which the pipeline has to curve towards an offshore located facility. By means of the numerical model we will make computations to explore to what extend we can pull the 20 inch pipeline into a curve.

In table 6.2 one can find the assumptions that hold for this computation.

Property	Abbreviation	Magnitude	Unit
Computed embedments	z	0.1D, 0.2D, 0.3D, 0.4D and 0.5D	$[m]$
Submerged weight pipeline	Wsub	95.95	$[kg/m]$
Saturated soil unit weight	γ'	15000	$[N/m^3]$
Numerical step size	h	2.00	$[m]$

Table 6.2: Target pipeline of the physical scale tests

6.3.1. Controlled pull target pipeline

We want to conduct a controlled pull-out installation and therefore apply the boundary conditions that hold for this method, as prescribed per subsection 5.3.1. As explained throughout this research, the extend to which the pipeline can be pulled is highly depending on the embedment rate that is obtained during the pull operation. Therefore the numerical predictions give a certain range of pull radii based on the en-reached embedment rate. By choosing for a radius following from an embedment rates of 10-20 percent, one chooses for a safe radius. If the pull radius that corresponds to a 50 percent embedment is chosen as the design radius, there is a larger chance that this radius can not be achieved by means of a controlled pull out (without the pipeline leaving the embedment). In figure 6.25 one can find the results of the numerical model predictions for the examined embedment rates.

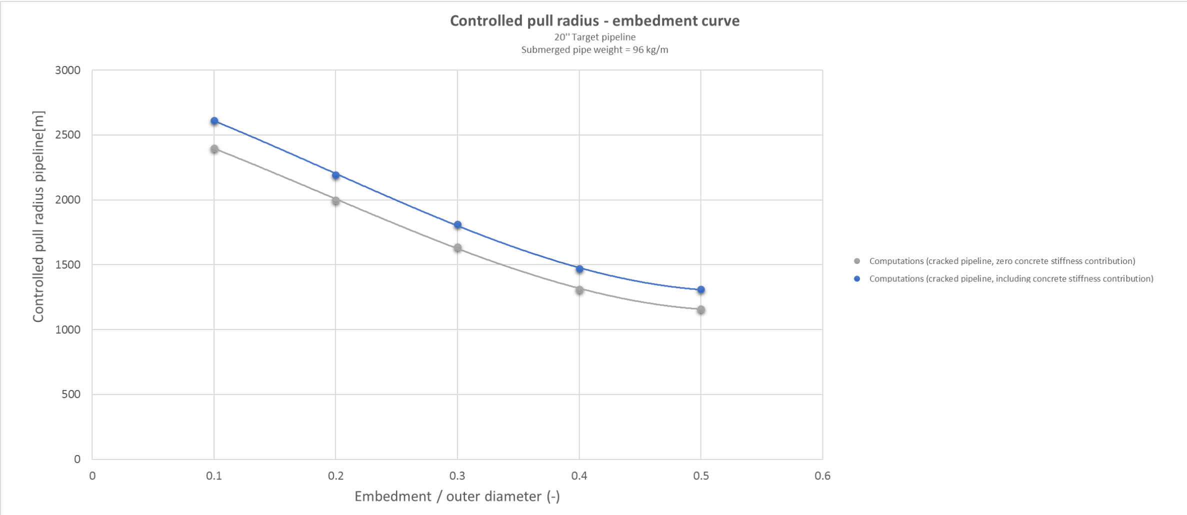

Figure 6.25: Model predictions of the minimum controlled pull radii for different embedment rates

The last 200 meter on the pull head side of the pipeline is modeled. One can observe that, according to the numerical model predictions, a controlled pull-out procedure can be conducted for radii between approximately 1200 meter and 2600 meter. Expected minimum bending radii tend to decrease almost linearly with the embedment rate. In case of cracked behaviour of the pipeline, the pipe pull radius rises approximately 200 meter in case of full material bond conditions.

By monitoring the embedment and pipe position during the (curved) pull operation, the operators should be able to reach the expected bending radii for the appearing embedment. Monitoring will be of key importance to achieve a succesfull curved pull operation, because it enables the project team to observe discrepancies and adapt to them.

6.3.2. Breakout pull target pipeline

If the controlled pull out procedure does not fulfill the design radius requirements, it is possible to conduct a breakout procedure to install the pipeline into a smaller radius. Because there is a higher risk of damaging the pipeline by means of this installation method, the breakout procedure should never be the desired option.

The graph of figure 6.26 shows the bending radius prediction of the pipeline during a forced breakout of the pipe head of 10 meter and negligible axial pipe tension and movement.

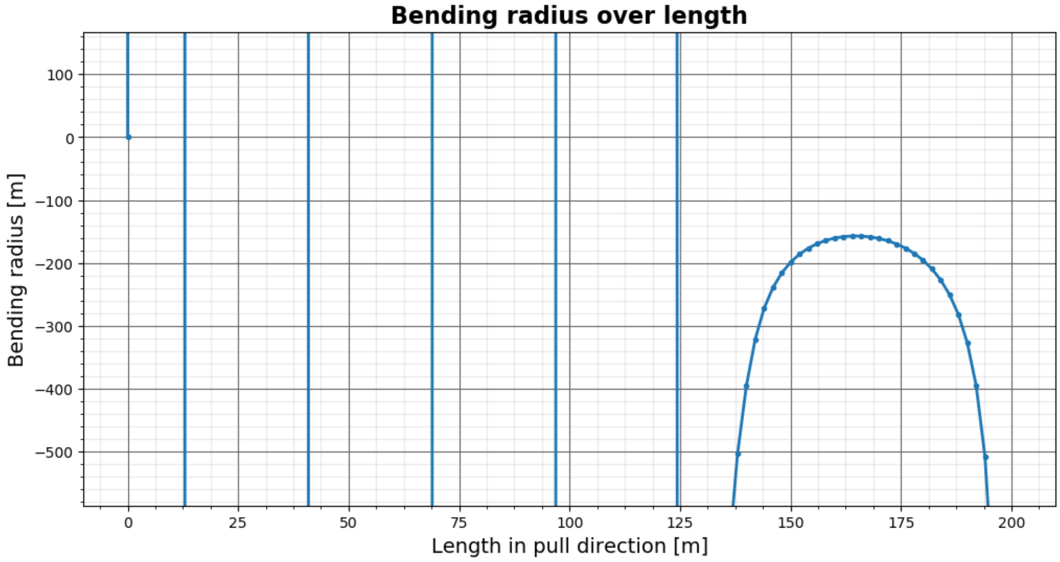

Figure 6.26: Model predictions of the bending radii of the target pipeline under a breakout pull (Y_{head}=10m and z/D=0.5)

The pipeline is predicted to bend at high rates over a relatively small axial length, which induces small bending radii and high pipeline strains/stresses locally. If the predicted curves are achieved, this pipeline should be designated to resist stresses up to 350 N/mm^2. Resulting maximum steel stresses are presented in figure 6.27.

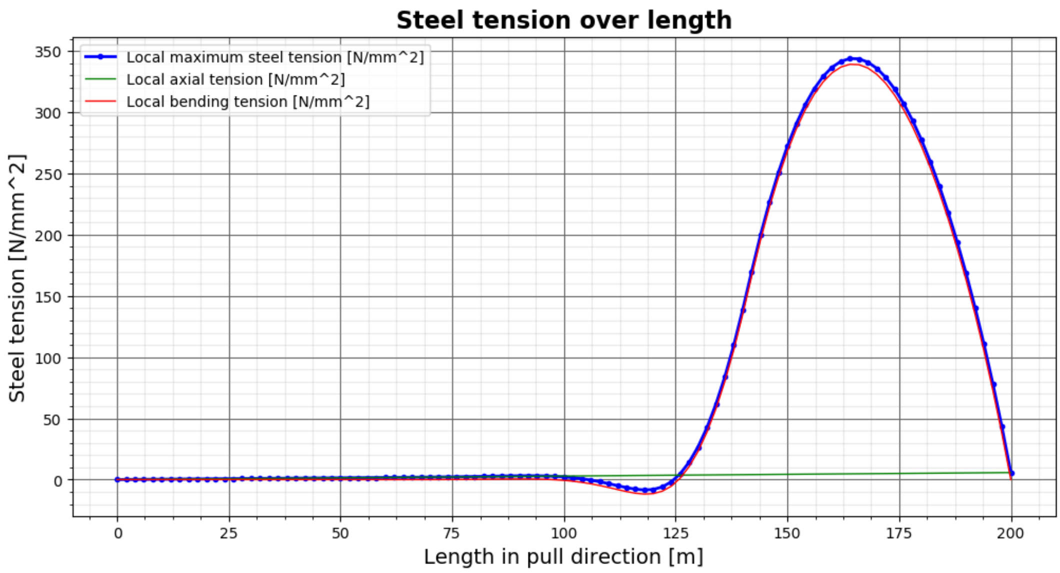

Figure 6.27: Model predictions of the maximum steel stress of the target pipeline under a breakout pull (Y_{head}=10m and z/D=0.5)

When conducting a breakout pull operation monitoring is even more important than for a controlled curved pull operations, since the risks are larger. The resulting steel tensions within this breakout pull would cause low steel quality pipelines to yield.

6.4. Capabilities and analysis of numerical model computations

Besides the pipeline displacement under axial and lateral loading, the numerical model is able to predict some expected main reactions of the pipeline. Examining the breakout behaviour of pipelines by means of the numerical model predictions gives a detailed insight of the processes that play a role during such an operation. Within this section, the output of the model is presented.
Since the model is created to predict dynamic curved pull operations based on the steady state (static) response of the pipeline under combined axial and lateral loading, the model can not be used to predict the reactions of the pipeline and surrounding seabed throughout a complete controlled curved pull operation. For the initial reaction to the first inclined pull the model computes the correct behaviour. The six most important reactions during a breakout are presented in the following subsections by means of the computations of the 110mm model pipeline.

Property	Magnitude	Unit
Test model diameter	110	$[mm]$
Test model length	12	$[m]$
Embedment	0.5D	$[-]$
Behaviour	Forced breakout	$[-]$
Lateral pipe head displacement	-2D	$[m]$
Numerical step size	0.12	$[m]$

Table 6.3: Input parameters computations

6.4.1. Lateral pipe displacement

In figure 6.28 the model output of lateral pipe displacement can be observed. The total length of the computation (hundred computational step heights) corresponds to the actual test model length, which is twelve meter. Special attention should be payed to the scale, which is different for the horizontal and vertical axis.

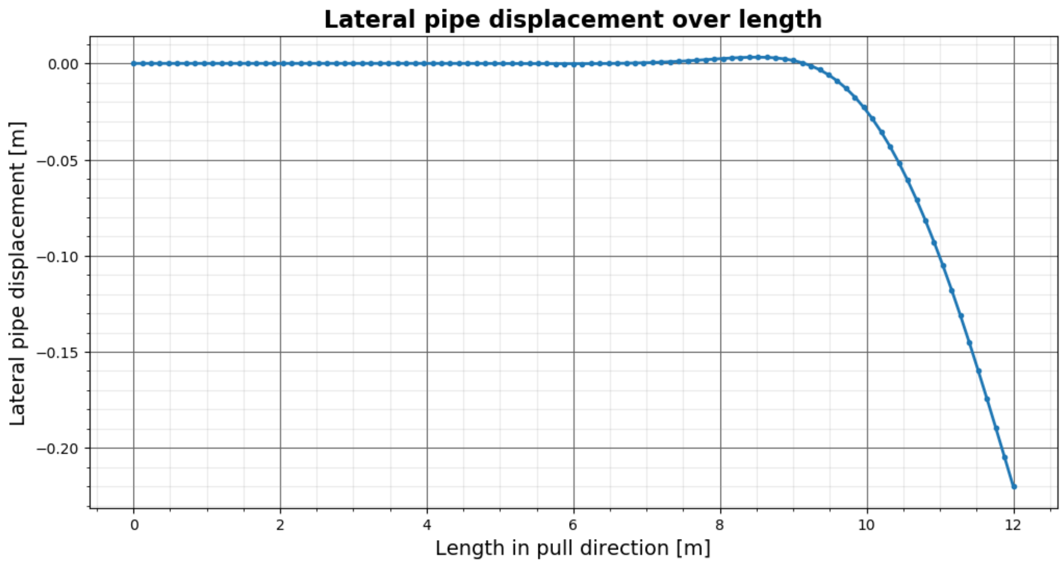

Figure 6.28: Lateral displacement computation of numerical model

On the right-hand side, the imposed boundary conditions of the pipe head displacement can be observed. Over a length of approximately 3 meters, the pipe gradually bends to the original lateral axis. In the following section of pipeline, seen from the pipe head side, the pipeline shows minor displacement into the outer bend seabed. This behaviour was observed throughout the experiments as well, although the outer bend displacement was little. The pipeline shows cantilever like behaviour.

6.4.2. Bending radius

In figure 6.29 the model output of the pipe bending radius can be observed.

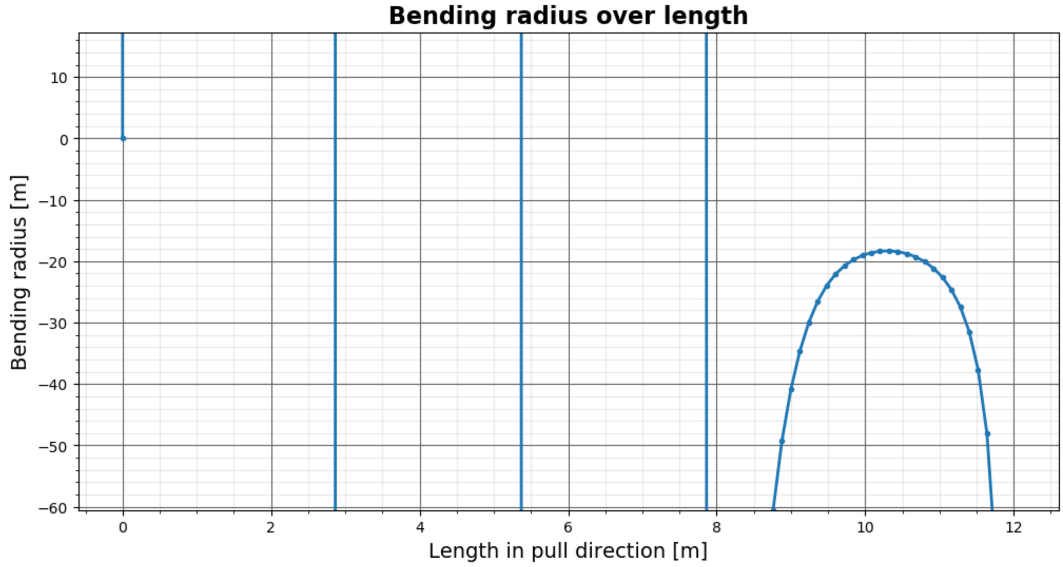

Figure 6.29: Bending radius computation of numerical model

Starting at the displaced pipe head (right-hand) side of the graph, one can observe that the bending radius tends to go to infinity. Approximately halfway the bend (close to coordinate 10.5 meters) the bending radius reaches her minimum bending radii. The latter is of major interest when examining the feasibility of forced breakout installation of pipelines, since the pipeline design tension follows from the smallest bending radius.

After the bend, the pipelines shows minor so-called "snaking" behaviour. Snaking behaviour is the sinusoidal movement of a pipeline. This mechanism is often observed (with significantly larger amplitudes) during the operation phase of offshore pipeline systems, under the influence of normal force resulting from heat expansion. The snaking behaviour has a steady period and results in infinity bending radii for the straight sections within. The zero crossings of the bending radii predictions do not appear in real life, but the value does switch sign.

6.4.3. Steel tension

In figure 6.30 the model output for the maximum tension of the pipeline material can be observed. Normally this computes the maximum tension of the steel part of the pipeline, for this case it represents the maximum tension in the PVC test model (as the Young's modulus of PVC was inserted).
The tension in the material is buildup out of two components, one resulting from axial tension and the other resulting from bending of the pipeline. Since the model assumes a linear decrease of tension from the pipe head side, the axial tension does too.

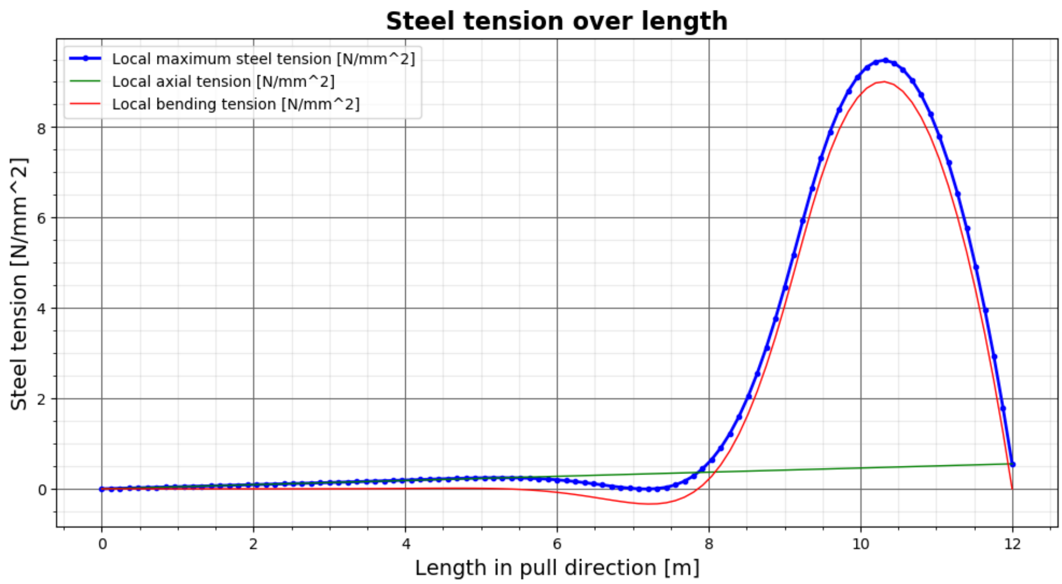

Figure 6.30: Steel tension computation of numerical model

If the maximum tension graph is compared with graph 6.29, we can observe the clear correlation of the bending tension to the bending radius of the pipeline.

6.4.4. Lateral soil resistance

In figure 6.31 the model output for the lateral soil resistance of the seabed can be observed.

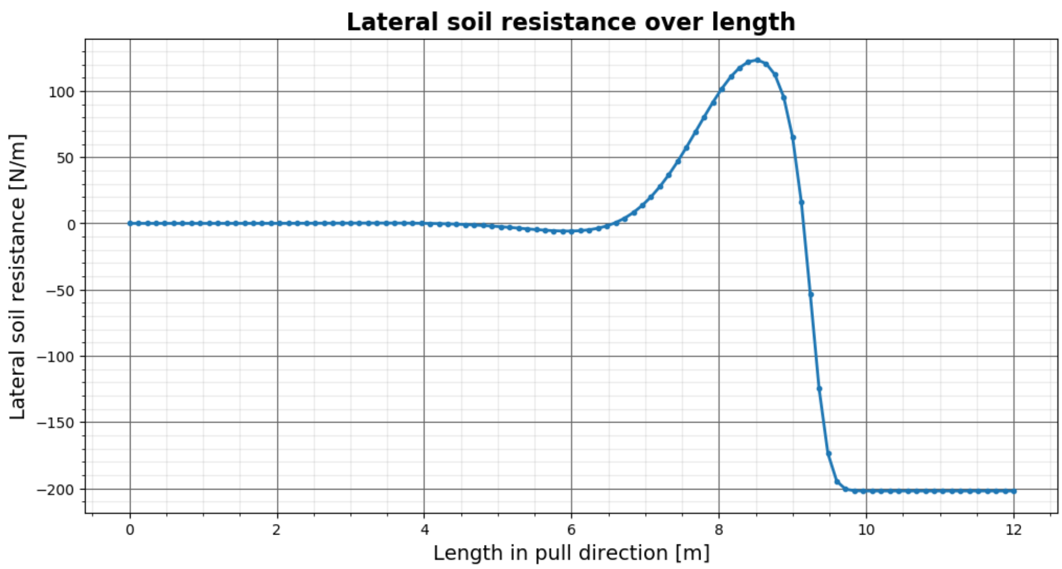

Figure 6.31: Lateral soil resistance computation of numerical model

Following from the P(Y) model assumption for the lateral soil reaction, the soil resistance shows a clear dependency of the lateral soil displacement (shown in figure 6.28). On the right-hand side one can clearly observe that the pipeline reached the full plastic breakout capacity of the soil, since the lateral soil reaction is stable over approximately two meters. The pipeline plowed the amount of soil that was required to accomplish an lateral force equilibrium.

Although the pipeline only showed minor movement after crossing the original neutral axis: the contribution of lateral soil resistance in the outer bend is significant. Pipelines experience significant resistance from the section after the bend because the maximum lateral soil resistance requires only little pipe displacement (minor fraction of the diameter) to be obtained. The underlying theory of this analyses can be found in 2.2.2.

6.4.5. Shear force

In figure 6.32 the model output for the shear force within the pipeline can be observed. Shear force is defined as the sum of the transverse (in this case lateral) forces that are transported through a specific section of a the structural element.

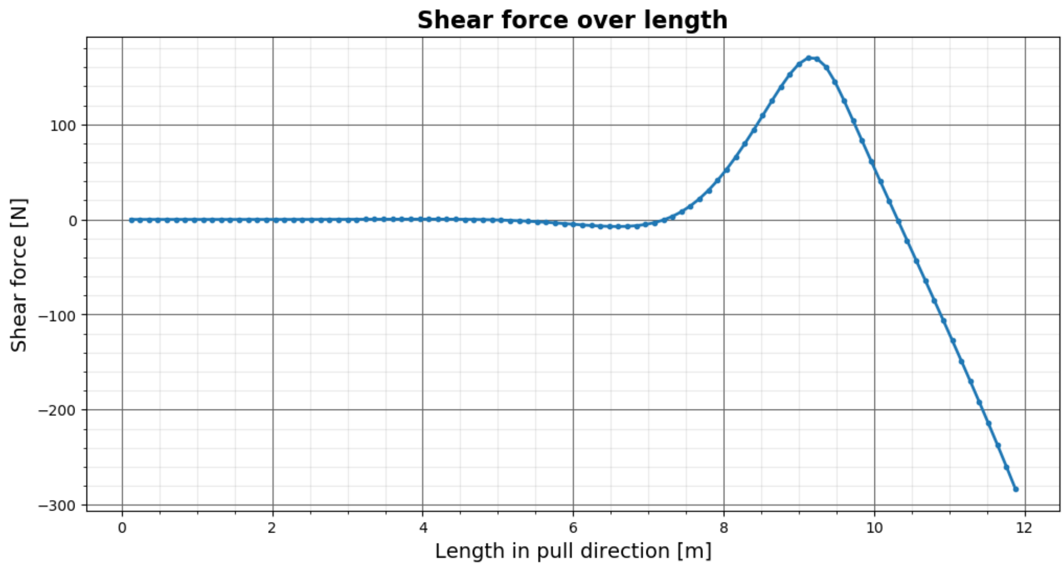

Figure 6.32: Shear force computation of numerical model

The right-hand side of the graph displays the lateral force that is imposed to the pipe head, as shown in figure 6.33. Under influence of the (restoring) lateral soil reaction on the pipe, the shear force in the pipelines dampens out. Figure 6.33 shows the influence of the lateral soil resistance on the shear force.
For future computations of forced breakout pull operations, this graph can be used to obtain the first estimate of the lateral force that should be applied to the pipe head.

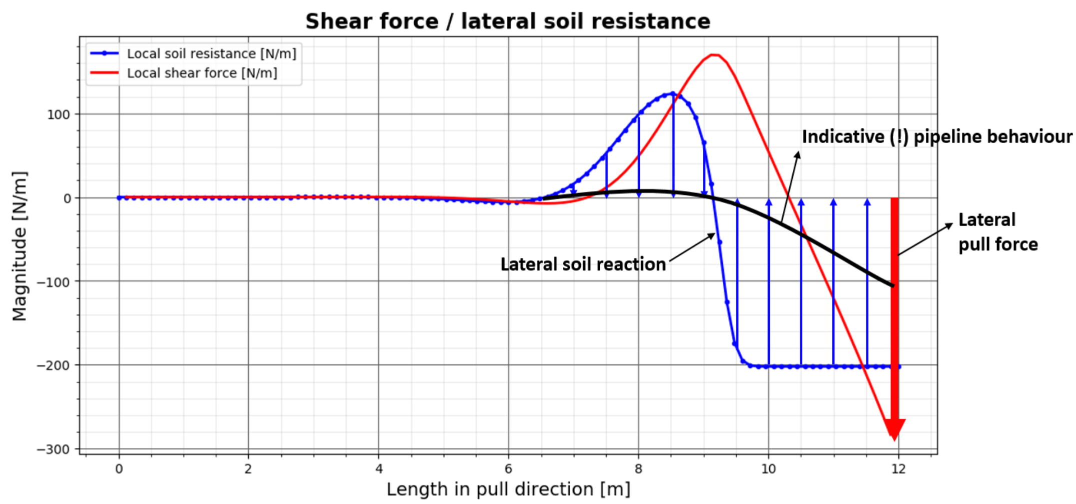

Figure 6.33: Combined plot of the shear force and lateral soil resistance as function of lateral pipeline displacement

Shear force, by definition, follows from the rate of pipeline bending and can therefore be coupled to figure 6.28). Shear force graphs can be used for the preliminary design calculations of forced breakout pipeline operations.

6.4.6. Bending moment

In figure 6.30 the model output for the maximum tension of the pipeline material can be observed.

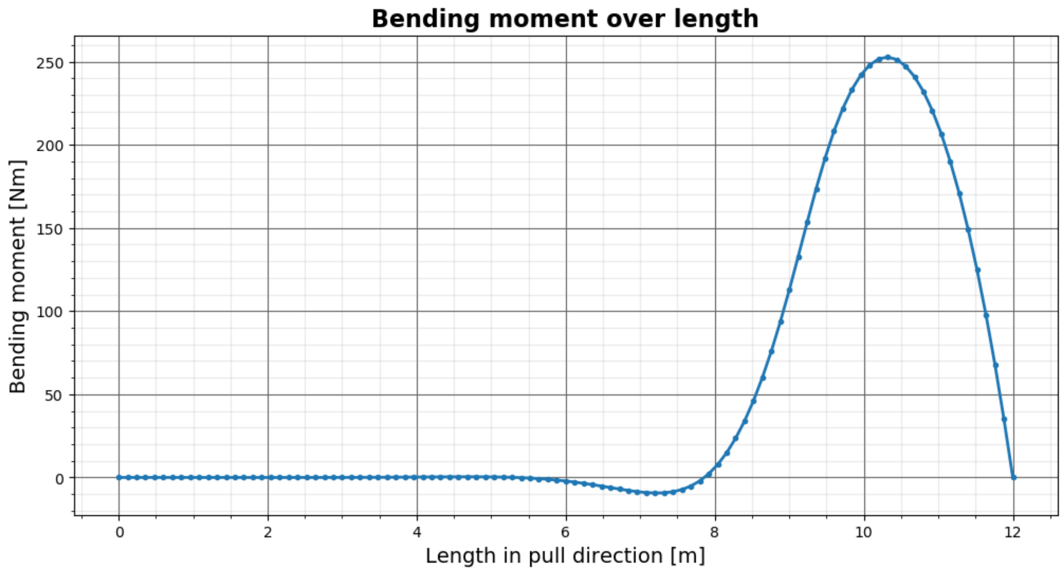

Figure 6.34: Bending moment computation of numerical model

Bending moment follows from the rate of pipeline bending and can therefore be coupled to figure 6.28). Under influence of the lateral soil reaction on the pipe, the shear force in the pipelines dampens out. Figure 6.35 shows the influence of the lateral soil resistance on the shear force.
Bending moment computations, as well as shear force computations, can be used for the preliminary design calculations of forced breakout pipeline operations.

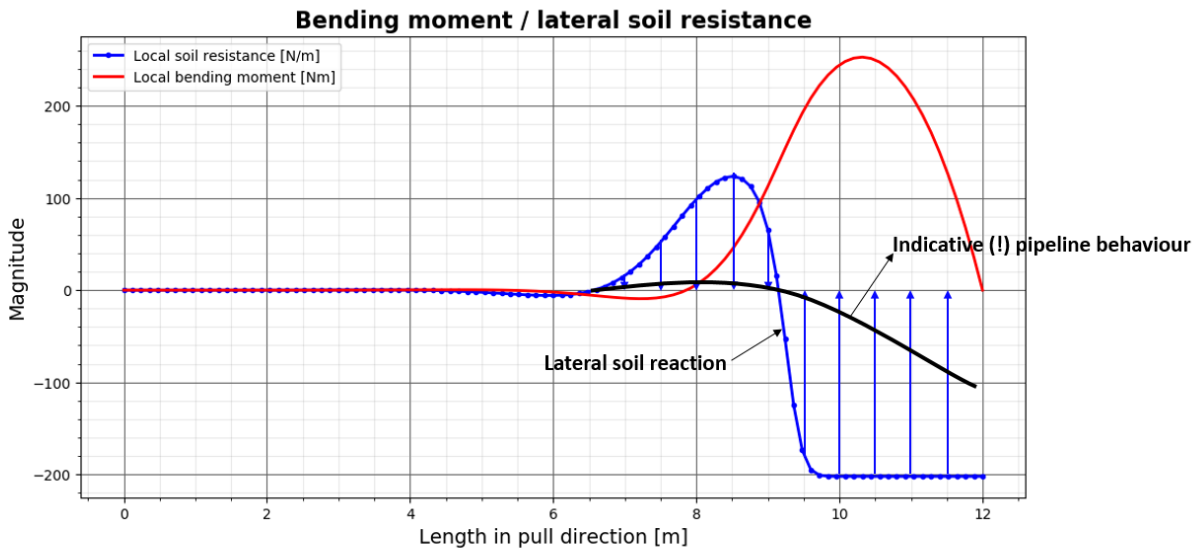

Figure 6.35: Combined plot of the bending moment and lateral soil resistance as function of lateral pipeline displacement

6.5. Limitations

While discussing the limitations of the model, we restrict it to the model limitations that apply to the controlled curved pipe pull behaviour. Although the model has also proven to give acceptable results for a forced lateral breakout behaviour (given that the axial pipeline propagation is negligible); this was not the focus of the model. Furthermore, the controlled pipe pull model was validated by means of a total of thirty tests, while the forced lateral breakout behaviour was validated by two scaled tests.

The limitations for which the controlled curve pull model is valid are summarized in table 6.4. In the right column of the table; the link with the applicable theory is mentioned.

Subject	Limitation	Based on theory of section
Soil types	Sandy seabeds	Section 2.2
Embedment rates	0.1D - 0.5D	Section 2.2
Structural behaviour pipeline	Elastic steel behaviour	Section 2.1
Step size model	1D - 4D	Section 5.2
Controlled pipe behaviour	Y < 1.5D	Section 2.3 and 5.3.1

Table 6.4: Limitations of the controlled numerical pull model

6.6. Intermediate conclusions to the research questions

Within this section the preliminary conclusions to the research questions are given. The conclusions are based on the knowledge gathered throughout this research, which includes:

1. An extensive theoretical study
2. A validated numerical soil-structure interaction model
3. A successful physical test campaign of thirty experiments

The research questions are answered in the paragraphs of this section.

What is the build-up of axial soil resistance of a submerged pipeline on a plain, non-cohesive, granular seabed, as a function of displacement? In practice, the axial soil resistance on a submerged pipeline builds up to a breakout peak resistance as it displaces towards the mobilization displacement (section 2.2.1). When the local axial tension exceeds the maximum breakout resistance of the underlying seabed, the pipeline is set into axial motion. While propagating into axial direction, the dynamic friction on the pipeline decreases. Considering the latter, the axial pull resistance during submerged pipeline on sandy seabeds are characterized by an undrained response.

Since the tension in a pipeline has a restoring effect on lateral pipeline displacement: the model obtained during this research is based on the local maximum tension in a pipeline. Based on former pipe pull projects, the Coulomb friction captures the axial maximum breakout friction well. Due to the latter, the Coulomb friction is adapted to incorporate the axial soil resistance in the computational model.

During the physical test phase of this research, the Coulomb friction model corresponded with the drained experimental data for axial friction.

What is the build-up of lateral soil resistance of a submerged pipeline on a plain, non-cohesive, granular seabed, as a function of displacement? Based on the fact that lateral displacement of partially embedded pipelines during a controlled curved pull operations is a slow process, the submerged lateral resistance of the surrounding soil can be prescribed by a drained response (section 6.1.3). This assumption implies that the lateral velocity of partially embedded pipelines throughout a controlled pipe pull operations is so low that is allows the pores of the pressurized saturated sand to drain without liquefaction effects (undrained response).

As the pipeline moves in lateral direction it builds up resistance until a breakout occurs. A breakout is reached at the displacement called the lateral breakout mobilization distance. The buildup of the resistance has a shape that can be prescribed by means of a tangent hyperbolic, with a maximum at the lateral mobilization distance.

During a lateral breakout, soil is plowed as a result of displacement of the pipeline. The amount of plowed soil has a strong effect on the subsequent pipe-soil interaction response. After the breakout this plowed sand berm, combined with the Coulomb friction of the pipeline, delivers the residual lateral resistance of the pipeline. The volume of plowed sand is dependent on the lateral pipe path that appears during the breakout.

Within section 6.1 the imposed lateral forces of the experiments were compared to those of the numerical model predictions. Along the classified critical curved pulls (described by figure 6.16), the imposed lateral force during the experiments was within 20% of the maximum predicted force in 86% of the physical tests. From this observation we can conclude that the numerical model captures the maximum lateral pull force with a high accuracy.

What is the influence of the stiffness of a pipeline on the trajectory of the submerged curved pull operation? The influence of the stiffness of a concrete covered steel pipeline on the trajectory of a curved pull operation is described according relation 5.8. Increasing bending stiffness of the pipeline will lead to a larger controlled pull radius, as resulted from both the experimental results as the validated numerical model predictions. Depending on the magnitude of the other restoring influences (the lateral soil resistance and the tension), the influence of pipeline stiffness changes can be examined.

Based on the combined plot (figure 4.22) of the controlled pull radii of two D_o 50 mm model pipelines that solely differed in stiffness one can conclude that the stiffness has less than a linear influence on the predicted pull radii. From the numerical model predictions within this research this was already expected. By plotting the numerical pull radii computations of the two pipelines into the former discussed graph of figure 4.22, figure 6.36 is obtained. This graph enables to compare the influence of pipeline stiffness in the model computations to those of the physically obtained results.

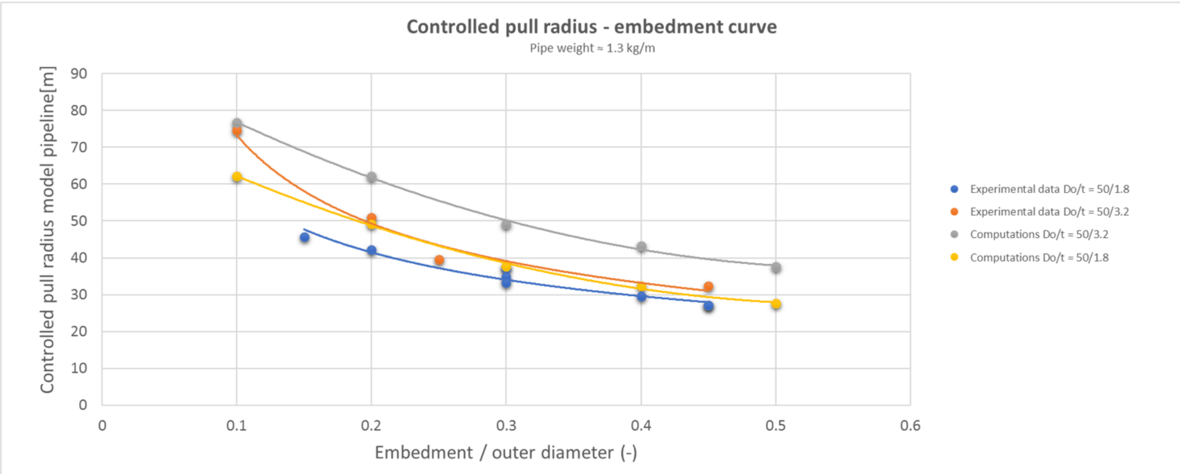

Figure 6.36: Bending moment computation of numerical model

The numerical model obtained within this research captures the influence of stiffness well, since the correlation of the numerical model predictions correlate with those of the corresponding experimental results. For larger normalized embedment ratios the influence of pipeline stiffness decreases for both the experiments as for the computations. The latter is an immediate result of the relative increase of the restoring lateral soil resistance force, which rises as the pipeline embedment increases.

As mentioned before during this paragraph, the influence of pipeline stiffness is specific for every different situation. The project specific influence of pipeline stiffness can only be predicted when studied extensively, by taking the magnitude/influence of submerged pipeline weight, saturated soil conditions, embedment and tensile forces into account. The validated numerical model of this research is a good tool to conduct these preliminary design studies.

7

Conclusions and recommendations

Throughout this research the feasibility of curved pipe pull operations on sandy seabeds is studied extensively. The research is based on three fundamental elements:

1. An extensive theoretical study
2. A validated numerical soil-structure interaction model
3. A successful physical test campaign of thirty-two experiments

During the two sections of this chapter, the conlusions of this research are stated and the recommendations for future studies are lined up.

7.1. Conclusions

At the starting phase of the research, a feasible installation method of pipelines into a curved trajectory arised. The installation method was based on the assumption of an adapted pull-out method. During the pull-out operation, the installation vessel (or barge) is relocated multiple times. By always maintaining an angle between the pull wire and the pipeline head: the pipeline will propagate in a curved trajectory while it propagates in axial direction. To create an installation procedure that is as controlled as reasonably possible, the pipeline is attempted to stay embedded throughout the complete pull-out procedure.

By creating a numerical model of the soil-structure interaction of the partially embedded pipeline, computations of the pipeline behaviour can be made. This enabled to predict to what extend concrete covered pipelines can be pulled into a curved trajectory. The model is based on the conducted theoretical study.
To validate the computations made with the numerical model, a physical test setup was constructed. By means of the test setup, thirty controlled curved pipe pull experiments where conducted. Five different model pipelines provided a brought range of pipelines to validate the model.

After the physical test phase, the experimental data was compared to the numerical model computations that corresponded to the model tests. Model computations of controlled curved pipe pull radii give an appropriate upper-bound prediction, since the obtained pull radii where 0 to 32% lower than the predicted numerical values. Only one experiment exceeded the predicted pull radius, by 7%.
The model was validated on two forced breakout tests as well. The numerical model computations captured both the breakout behaviour as the break out forces well.

Within the desired classification of critical curved pulls (described by figure 6.16), the imposed lateral force during the experiments was within 20% of the numerically predicted force in 86% of the physical tests. From this observation we can conclude that the numerical model is able to predict the maximum lateral pull force with a high accuracy.
For the other 14% of the critical curved pull experiments the soil appeared to have more bearing strength

than expected, as the required lateral pull force on the head was 20-50% higher for those cases.

From the diagram of curved breakout pulls, displayed in 6.16), one can conclude that 75% of the curved breakouts was expected to appear by the numerical model predictions. Another 25% was likely to happen since the computational model predictions showed that the physically imposed lateral pull exceeded 80% of the maximum soil capacity. Again, the numerical model was able to predict the behaviour of the pipeline with a high accuracy.

Depending on the project-specific pipeline and seabed parameters, typical concrete covered submerged pipelines can be pulled into a radius varying in the order of multiple hundreds to thousands of pipeline diameters. This research provides a validated non-linear numerical model to predict the controlled pull radius and lateral pull force for different normalized embedment rates.

Answer to the research question

By means of the validated prediction model, a numerical answer is computed to the research question. We examine two pipelines on the outer edges of the scope of research, to compute to what extend pipelines can be pulled into a curved trajectory.

The proposed pipelines are:

- 18” pipeline (t=9.53mm and CC=60mm), 500 meter pull length
- 50” pipeline (t=25.4mm and CC=40mm), 5000 meter pull length

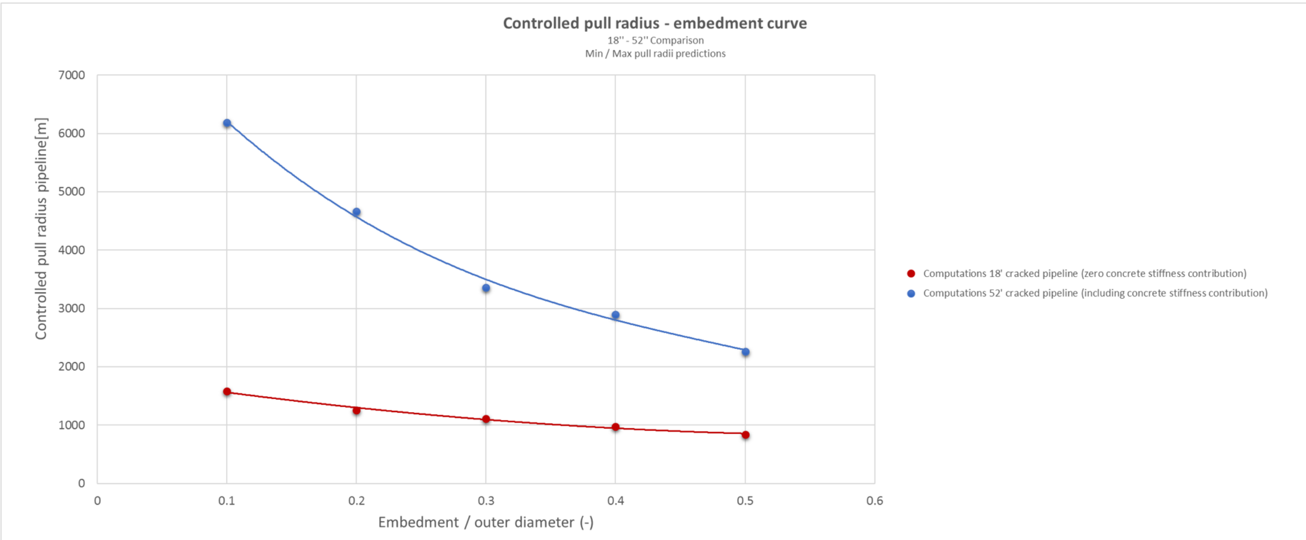

Figure 7.1: Numerical model computations of two pipelines on the outer edges of the scope of research, providing answer to the research question

After the computations (displayed in 7.1) of pipelines on the outer edges of the spectrum of research, we can state that pipelines can be pulled into radii varying between 800 meter and 6000 meter.

7.2. Recommendations

This research does not include all curved pipe pull related subjects of interest. Future studies can pursue research regarding the feasibility of curved pipe pull operations to broaden knowledge of this interesting installation method.

The physical test setup constructed for the purpose of this research provides the opportunity to be reused and obtain experimental data of more elaborate curved pipe pull installation methods.

First, the submerged behaviour of model pipelines should be studied. By means of submerged tests the computational model predictions can be validated for submerged conditions. Discrepancies will appear if the lateral soil resistance is not characterized by drained behaviour. The pull velocity will have to be modeled correctly during these experiments, since it is an essential parameter to study the submerged pipeline behaviour correctly.

Within the pipe pull industry there is a saying which implies that a pipeline will follow the trajectory of the pull wire during a pull installation. By testing with different combinations of pipeline models and pull wires, an experimental study can be conducted to see to what extend this assumption holds. The physical test setup built during this research enables to performsubmerged pipe pull experiments to test this pipe pull myth on a relatively large scale (1/20 to 1/5).

The last interesting element that can be elaborated in future studies involve the influence of seabed irregularities on curved pipe pull operations. By seabed irregularities one can think of the influence of an artificial dredged trench trajectory or the influence of natural phenomena like seabed ripples and dunes.

Bibliography

[1] Wang et al. *Experimental and upper-bound analysis of lateral soil resistance for shallow embedded pipeline in Bohai Sand.* Article in Journal of Pipeline Systems Engineering and Practice, November 2018.
[2] C. Vuik. *Numerical Methods for Ordinary Differential Equations.* Booklet, June 2016.
[3] A.V. Metrikine. *Dynamics, Slender Structures and an Introduction to Continuum Mechanics.* Booklet, August 2016.
[4] K.G. Gavin. *CIE 4362-Structure Interaction.* Handout - Parameter assessment in Geomechanics, 2016.
[5] Det Norske Veritas. *DNVGL-ST-F101.* Design Standard: Submarine pipeline systems, December 2017.
[6] Det Norske Veritas. *DNVGL-RP-F109.* Recommended practice: On-bottom stability design of submarine pipelines, May 2017.
[7] Det Norske Veritas. *DNVGL-RP-F110.* Recommended practice: Global buckling of submarine pipelines, April 2018.
[8] Det Norske Veritas. *DNVGL-RP-F114.* Recommended practice: Pipe-soil interaction for submarine pipelines, May 2017.
[9] Det Norske Veritas. *DNVGL-RP-C212.* Recommended practice: Offshore soil mechanics and geotechnical engineering, August 2017.

8
Appendices

A

Summary experimental data $D_o/t = 50/1.8[mm]$ model

Pull No.	X start [m]	X end [m]	Δ X [m]	Y start [m]	Y end [m]	Δ Y [m]	θ start [°]	θ end [°]	α start [°]	α end [°]	F pull start [kg]	F pull end [kg]	Δ F pull [kg]	F pull lateral start [kg]	F pull lateral end [kg]	Δ F pull lateral [kg]	F pull axial start [kg]	F pull axial end [kg]	Δ F pull axial [kg]	F predicted lateral breakout [kg]	F predicted axial resistance [kg]
Pull I	3.00	4.00	1.00	0.00	0.00	0.00	0.00	0.00	0.00	0.00	12.50	11.50	-1.00	0.00	0.00	0.00	12.50	11.50	-1.00	2.65	9.79
Pull II	4.00	6.00	2.00	0.00	0.04	0.04	1.00	2.00	2.65	3.10	12.00	12.00	0.00	0.55	0.65	0.09	12.00	12.00	0.00	2.65	9.79
Pull III	6.00	9.30	3.30	0.04	0.27	0.23	2.00	9.00	6.53	9.02	12.50	12.50	0.00	1.42	1.96	0.54	12.46	12.50	0.04	2.65	9.79
Pull IV	9.30	11.90	2.60	0.27	0.75	0.48	9.00	12.00	12.33	18.67	12.50	11.00	-1.50	2.67	3.52	0.85	12.48	10.93	-1.55	2.65	9.79

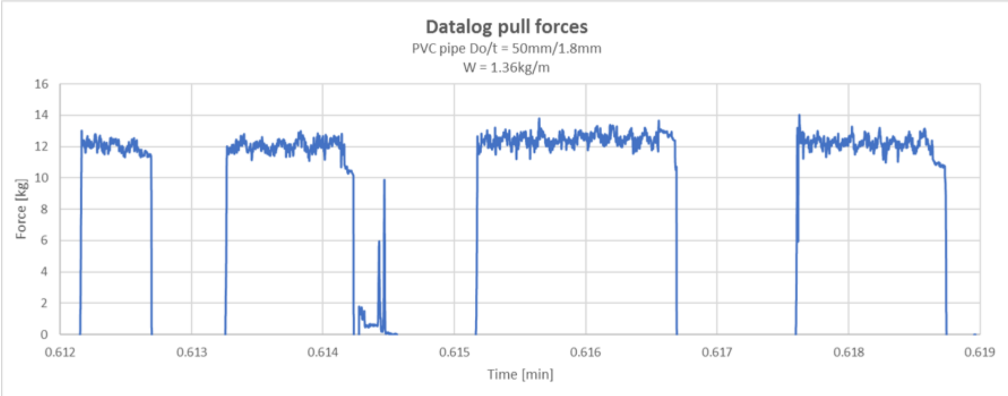

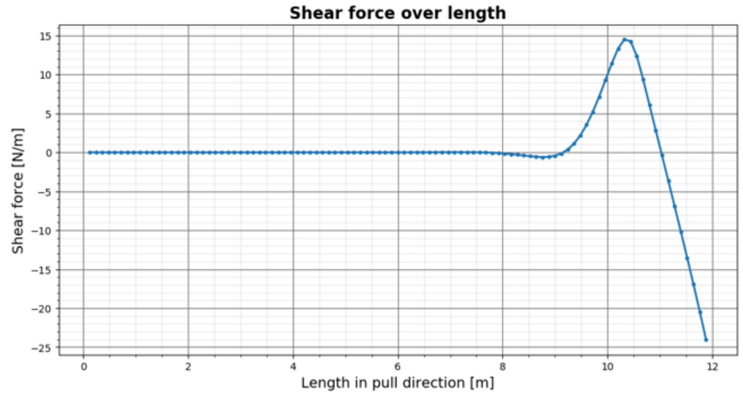

Figure A.1: Summary of experimental data;
Model $D_o/t = 50/1.8[mm]$ and $W = 1.36[kg/m]$,
Test 1

Pull No.	X start [m]	X end [m]	Δ X [m]	Y start [m]	Y end [m]	Δ Y [m]	θ start [°]	θ end [°]	α start [°]	α end [°]	F pull start [kg]	F pull end [kg]	Δ F pull [kg]	F pull lateral start [kg]	F pull lateral end [kg]	Δ F pull lateral [kg]	F pull axial start [kg]	F pull axial end [kg]	Δ F pull axial [kg]	F predicted lateral breakout [kg]	F predicted axial resistance [kg]
Pull I	3.00	5.00	2.00	0.00	0.00	0.00	0.00	0.00	0.00	0.00	11.50	10.50	-1.00	0.00	0.00	0.00	11.50	10.50	-1.00	2.26	9.79
Pull II	5.00	7.00	2.00	0.00	0.04	0.04	1.00	2.00	3.00	3.65	11.00	12.00	1.00	0.58	0.76	0.19	10.99	12.00	1.00	2.26	9.79
Pull III	7.00	9.30	2.30	0.06	0.25	0.19	2.00	4.00	7.47	9.35	12.00	11.50	-0.50	1.56	1.87	0.31	11.95	11.45	-0.50	2.26	9.79
Pull IV	9.00	11.50	2.50	0.25	1.15	1.15	4.00	15.00	20.35	21.54	11.50	11.00	-0.50	4.00	4.04	0.04	11.04	10.93	-0.11	2.26	9.79

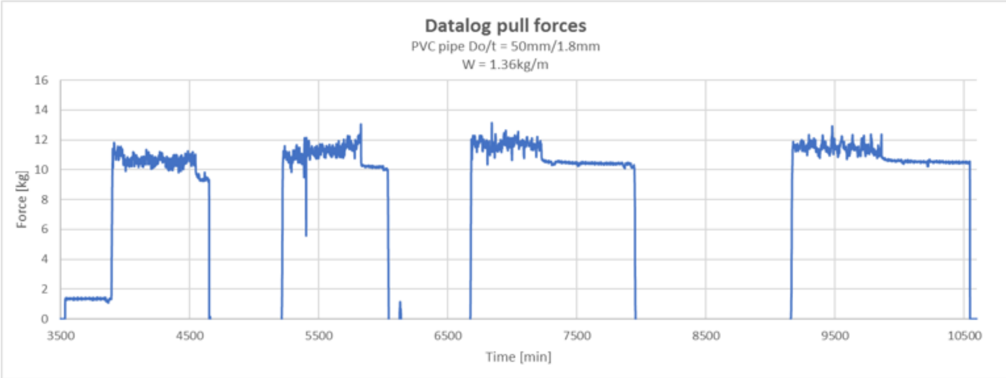

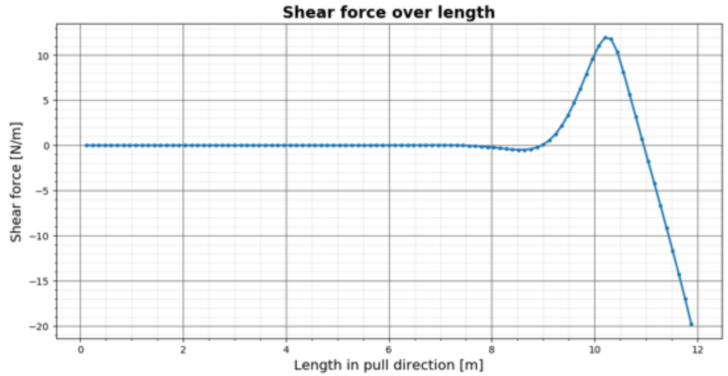

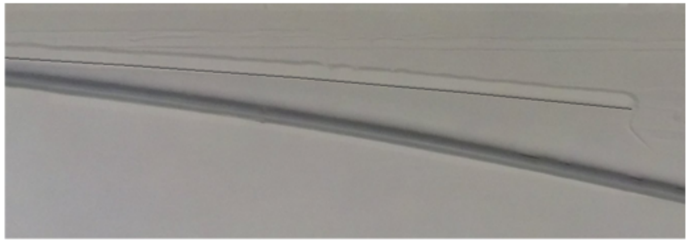

Figure A.2: Summary of experimental data;
Model $D_o/t = 50/1.8[mm]$ and $W = 1.36[kg/m]$,
Test 2

Pull No.	X start [m]	X end [m]	Δ X [m]	Y start [m]	Y end [m]	Δ Y [m]	θ start [°]	θ end [°]	α start [°]	α end [°]	F pull start [kg]	F pull end [kg]	Δ F pull [kg]	F pull lateral start [kg]	F pull lateral end [kg]	Δ F pull lateral [kg]	F pull axial start [kg]	F pull axial end [kg]	ΔF pull axial [kg]	F predicted lateral breakout [kg]	F predicted axial resistance [kg]
Pull I	3.00	5.00	2.00	0.00	0.00	0.00	0.00	0.00	0.00	0.00	14.00	12.50	-1.50	0.00	0.00	0.00	14.00	12.50	-1.50	2.94	9.79
Pull II	5.00	7.00	2.00	0.00	0.08	0.08	1.00	4.00	3.00	3.25	13.00	13.50	0.50	0.68	0.76	0.09	12.99	13.50	0.51	2.94	9.79
Pull III	7.00	8.90	1.90	0.08	0.22	0.14	4.00	5.00	7.28	8.82	13.50	13.50	0.00	1.71	2.07	0.36	13.48	13.47	-0.01	2.94	9.79
Pull IV	8.90	11.70	2.80	0.22	0.77	0.55	5.00	10.00	11.78	14.00	14.00	11.00	-3.00	2.86	2.66	-0.20	13.90	10.97	-2.93	2.94	9.79

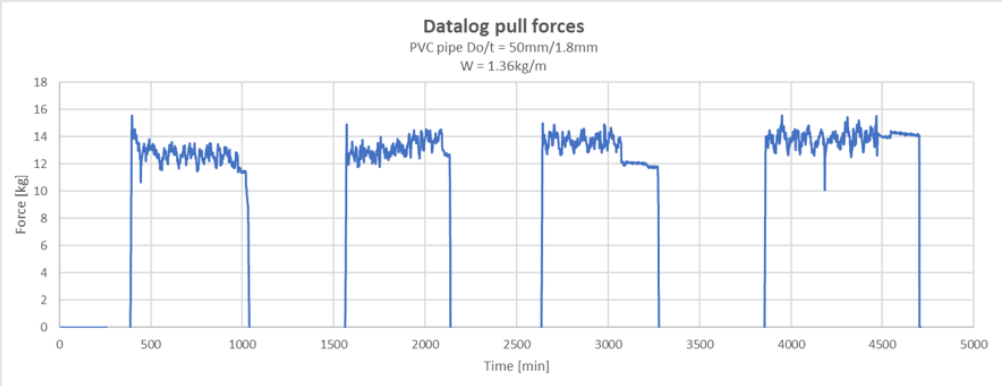

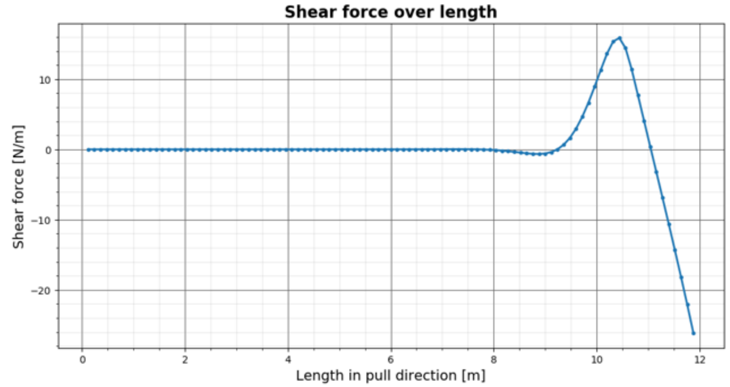

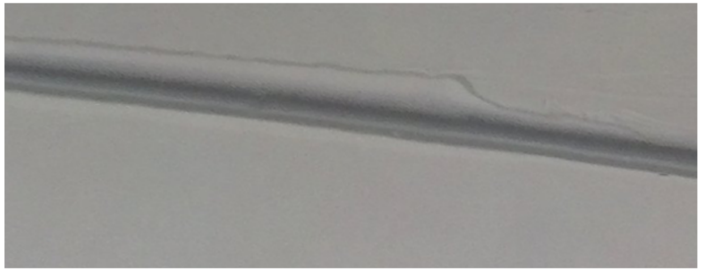

Figure A.3: Summary of experimental data;
Model $D_o/t = 50/1.8[mm]$ and $W = 1.36[kg/m]$,
Test 3

Pull No.	X start [m]	X end [m]	Δ X [m]	Y start [m]	Y end [m]	Δ Y [m]	θ start [°]	θ end [°]	α start [°]	α end [°]	F pull start [kg]	F pull end [kg]	Δ F pull [kg]	F pull lateral start [kg]	F pull lateral end [kg]	Δ F pull lateral [kg]	F pull axial start [kg]	F pull axial end [kg]	Δ F pull axial [kg]	F predicted lateral breakout [kg]	F predicted axial resistance [kg]
Pull I	3.00	5.00	2.00	0.00	0.06	0.06	0.00	2.00	2.38	2.55	14.00	14.00	0.00	0.58	0.62	0.04	13.99	14.00	0.01	2.94	9.79
Pull II	5.00	6.90	1.90	0.06	0.24	0.18	2.00	4.00	5.53	5.57	14.50	15.00	0.50	1.40	1.46	0.06	14.47	14.99	0.52	2.94	9.79
Pull III	6.90	8.90	2.00	0.24	0.52	0.28	4.00	8.00	9.49	10.30	14.50	14.00	-0.50	2.39	2.50	0.11	14.43	13.99	-0.44	2.94	9.79
Pull IV	8.90	11.40	2.50	0.52	1.09	0.57	5.00	12.00	13.24	14.00	14.50	14.50	0.00	3.32	3.51	0.19	14.35	14.49	0.14	2.94	9.79

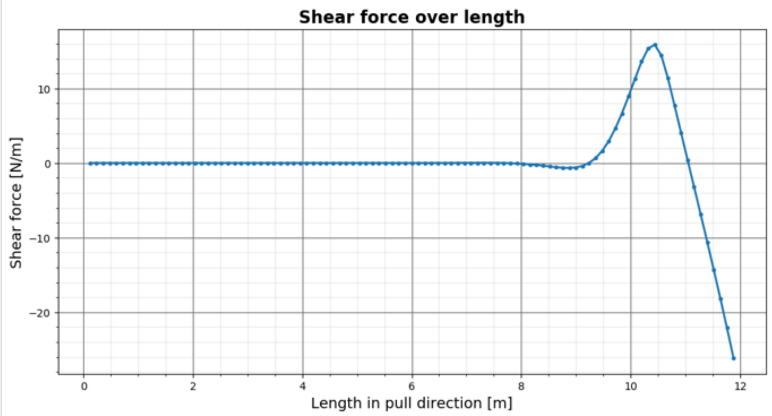

Figure A.4: Summary of experimental data;
Model $D_o/t = 50/1.8[mm]$ and $W = 1.36[kg/m]$,
Test 4

Pull No.	X start [m]	X end [m]	ΔX [m]	Y start [m]	Y end [m]	ΔY [m]	θ start [°]	θ end [°]	α start [°]	α end [°]	F pull start [kg]	F pull end [kg]	ΔF pull [kg]	F pull lateral start [kg]	F pull lateral end [kg]	ΔF pull lateral [kg]	F pull axial start [kg]	F pull axial end [kg]	ΔF pull axial [kg]	F predicted lateral breakout [kg]	F predicted axial resistance [kg]
Pull I	3.00	5.00	2.00	0.00	0.03	0.03	0.00	1.00	0.00	-0.22	14.50	14.50	0.00	0.00	-0.06	-0.06	14.50	14.50	0.00	2.26	9.79
Pull II	5.00	7.00	2.00	0.03	0.12	0.09	1.00	3.00	2.77	2.84	15.00	15.00	0.00	0.73	0.74	0.02	14.99	15.00	0.01	2.26	9.79
Pull III	7.00	9.00	2.00	0.12	0.31	0.19	3.00	6.00	6.87	7.67	15.00	15.00	0.00	1.80	2.00	0.21	14.97	14.99	0.03	2.26	9.79
Pull IV	9.00	11.70	2.70	0.31	0.81	0.50	6.00	11.00	10.73	14.00	14.50	14.50	0.00	2.70	3.51	0.81	14.45	14.48	0.03	2.26	9.79

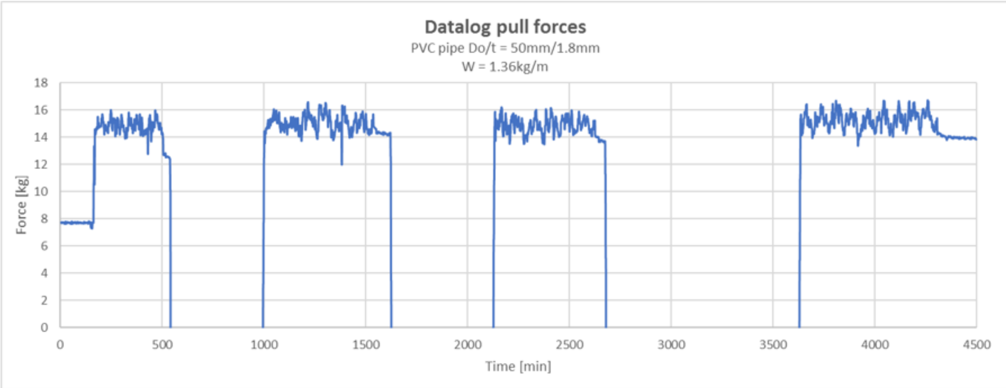

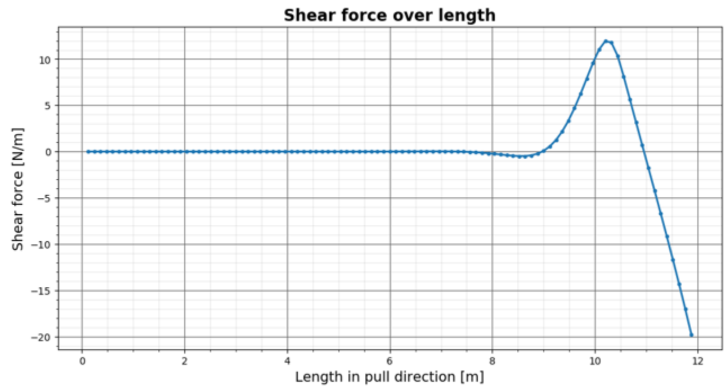

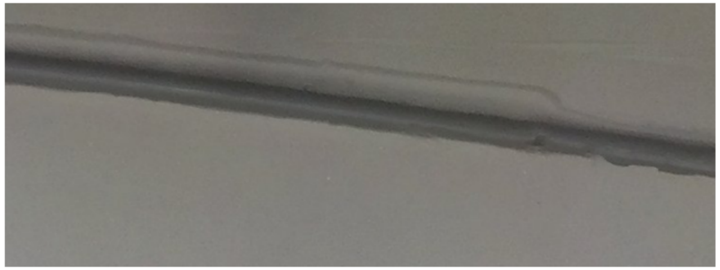

Figure A.5: Summary of experimental data;
Model $D_o/t = 50/1.8[mm]$ and $W = 1.36[kg/m]$,
Test 5

Pull No.	Xstart [m]	X end [m]	Δ X [m]	Y start [m]	Y end [m]	Δ Y [m]	θ start [°]	θ end [°]	α start [°]	α end [°]	F pull start [kg]	F pull end [kg]	Δ F pull [kg]	F pull lateral start [kg]	F pull lateral end [kg]	Δ F pull lateral [kg]	F pull axial start [kg]	F pull axial end [kg]	Δ F pull axial [kg]	F predicted lateral breakout [kg]	F predicted axial resistance [kg]
Pull I	3.00	5.00	2.00	0.00	0.12	0.12	0.00	3.00	0.00	-0.90	11.50	11.50	0.00	0.00	-0.18	-0.18	11.50	11.47	-0.03	1.77	9.79
Pull II	5.00	6.00	1.00	0.12	0.18	0.06	3.00	5.00	2.10	1.90	11.50	11.00	-0.50	0.42	0.36	-0.06	11.50	10.98	-0.51	1.77	9.79
Pull III	6.00	7.00	1.00	0.18	0.30	0.12	5.00	7.00	5.33	5.07	11.50	11.50	0.00	1.07	1.02	-0.05	11.50	11.49	-0.01	1.77	9.79
Pull IV	7.00	8.00	1.00	0.30	0.46	0.16	7.00	8.00	7.07	14.00	11.50	11.50	0.00	1.42	2.78	1.37	11.50	11.44	-0.06	1.77	9.79
Pull V	8.00	10.60	2.60	0.46	0.92	0.46	8.00	11.00	9.06	7.82	11.50	11.50	0.00	1.81	1.56	-0.25	11.50	11.48	-0.02	1.77	9.79

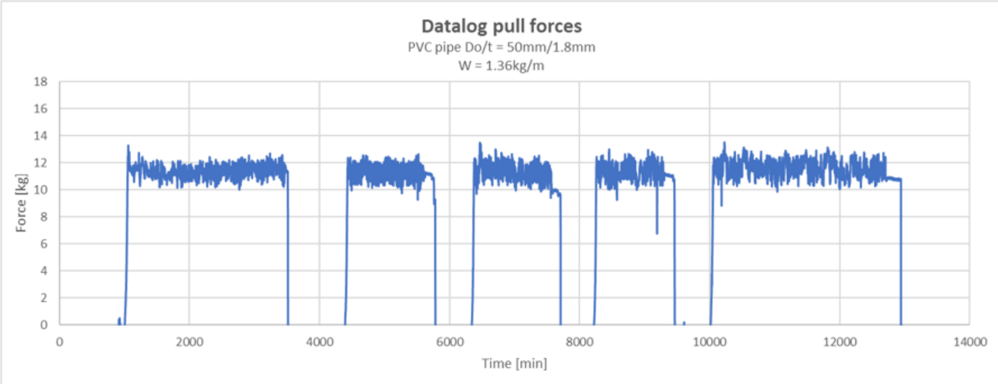

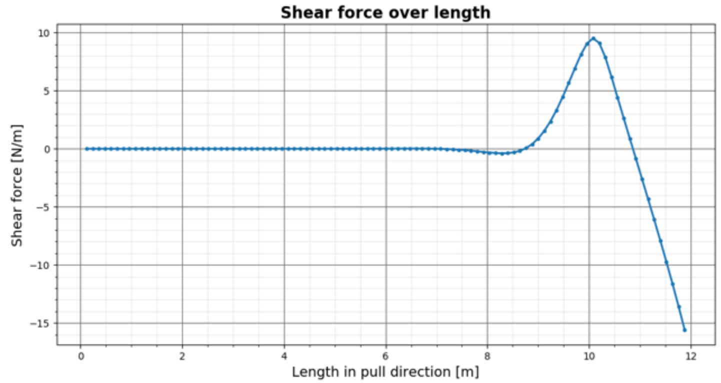

Figure A.6: Summary of experimental data;
Model $D_o/t = 50/1.8[mm]$ and $W = 1.36[kg/m]$,
Test 6

Pull No.	X start [m]	X end [m]	ΔX [m]	Y start [m]	Y end [m]	ΔY [m]	θ start [°]	θ end [°]	α start [°]	α end [°]	F pull start [kg]	F pull end [kg]	Δ F pull [kg]	F pull lateral start [kg]	F pull lateral end [kg]	Δ F pull lateral [kg]	F pull axial start [kg]	F pull axial end [kg]	Δ F pull axial [kg]	F predicted lateral breakout [kg]	F predicted axial resistance [kg]
Pull I	3.00	5.00	2.00	0.00	0.10	0.10	0.00	3.00	2.38	2.25	11.50	11.50	0.00	0.48	0.45	-0.03	11.49	11.50	0.01	1.47	9.79
Pull II	5.00	7.00	2.00	0.10	0.24	0.14	3.00	5.00	5.23	5.67	11.50	11.50	0.00	1.05	1.14	0.09	11.49	11.50	0.01	1.47	9.79
Pull III	7.00	8.90	1.90	0.24	0.47	0.23	5.00	8.00	7.67	8.07	11.50	11.50	0.00	1.54	1.61	0.08	11.49	11.50	0.01	1.47	9.79
Pull IV	8.90	11.20	2.30	0.47	0.88	0.41	8.00	9.00	11.04	14.00	11.50	12.00	0.50	2.20	2.90	0.70	11.48	11.95	0.47	1.47	9.79

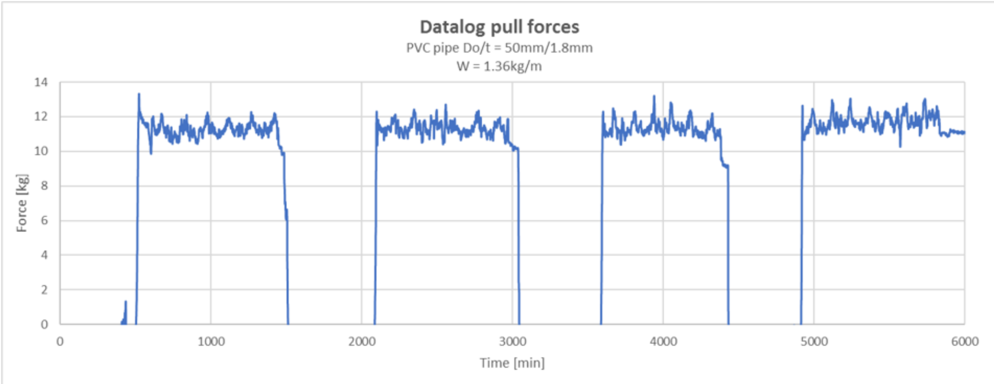

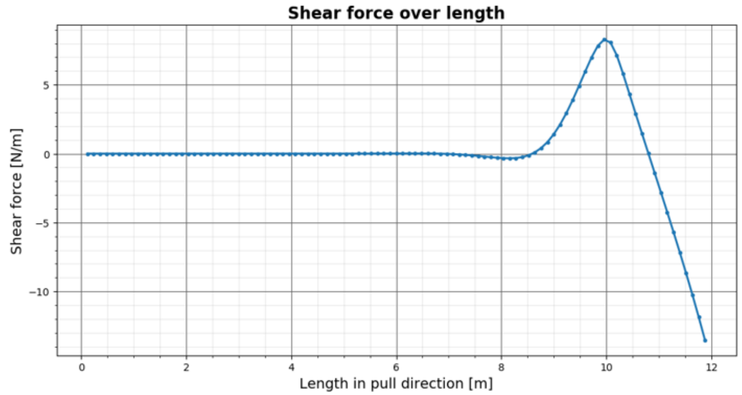

Figure A.7: Summary of experimental data;
Model $D_o/t = 50/1.8[mm]$ and $W = 1.36[kg/m]$,
Test 7

Pull No.	X start [m]	Xend [m]	Δ X [m]	Y start [m]	Y end [m]	Δ Y [m]	θ start [°]	θ end [°]	α start [°]	α end [°]	F pull start [kg}	F pull end [kg]	Δ F pull [kg]	F pull lateral start [kg]	F pull lateral end [kg]	Δ F pull lateral [kg]	F pull axial start [kg]	F pull axial end [kg]	ΔF pull axial [kg]	F predicted lateral breakout [kg]	F predicted axial resistance [kg]
Pull I	3.00	5.00	2.00	0.00	0.04	0.04	0.00	1.00	2.38	2.70	10.50	11.50	1.00	0.44	0.54	0.11	10.49	11.49	1.00	2.26	9.79
Pull II	5.00	8.00	3.00	0.04	0.19	0.15	1.00	5.00	5.68	7.49	11.00	14.00	3.00	1.09	1.82	0.74	10.96	13.99	3.02	2.26	9.79
Pull III	8.00	9.40	1.40	0.19	0.30	0.11	5.00	6.00	9.90	12.19	12.00	13.00	1.00	2.06	2.75	0.68	11.96	12.92	0.97	2.26	9.79
Pull IV	9.40	11.20	1.80	0.30	0.74	0.44	6.00	10.00	15.52	14.00	12.50	12.00	-0.50	3.35	2.90	-0.44	12.33	11.97	-0.36	2.26	9.79

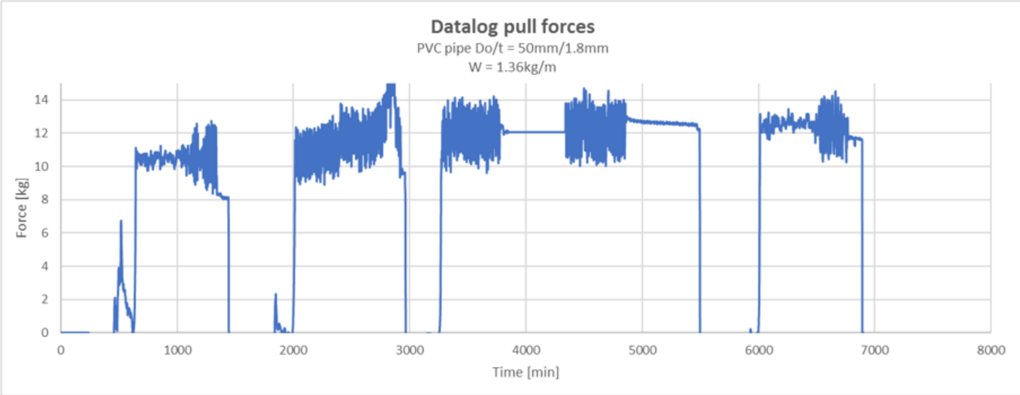

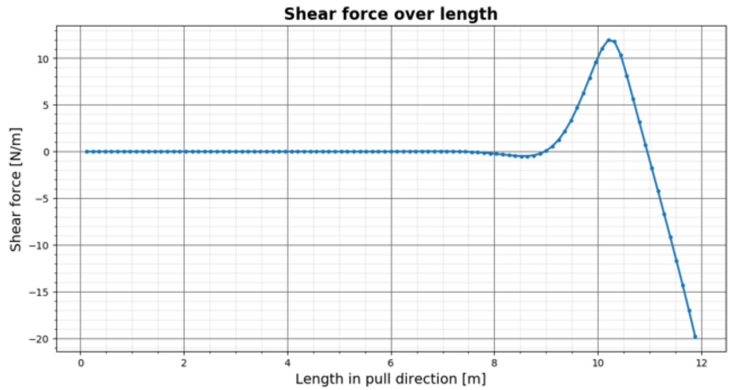

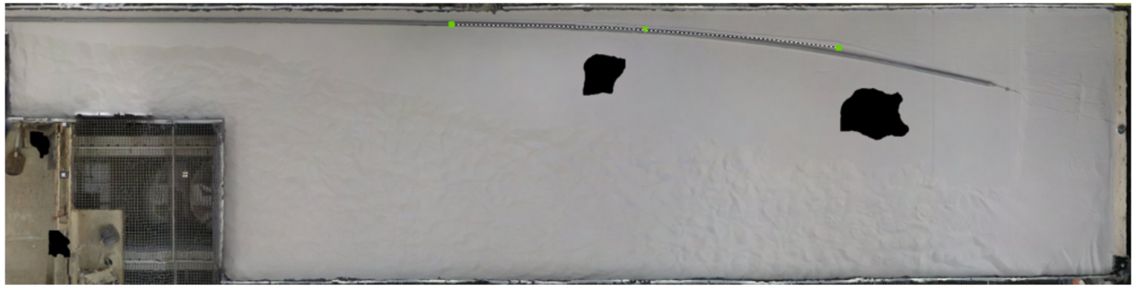

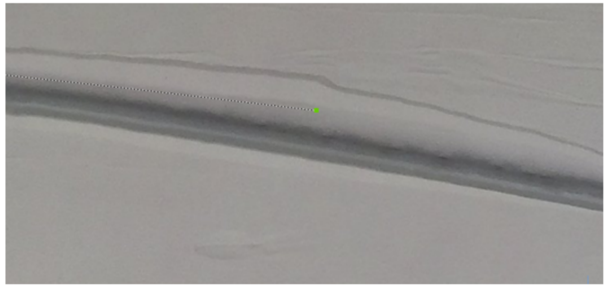

Figure A.8: Summary of experimental data;
Model $D_o/t = 50/1.8[mm]$ and $W = 1.36[kg/m]$,
Test 8

B

Summary experimental data $D_o/t = 50/3.2[mm]$ model

Pull No.	X start [m]	X end [m]	Δ X [m]	Y start [m]	Y end [m]	Δ Y [m]	θ start [°]	θ end [°]	α start [°]	α end [°]	F pull start [kg]	F pull end [kg]	Δ F pull [kg]	F pull lateral start [kg]	F pull lateral end [kg]	Δ F pull lateral [kg]	F pull axial start [kg]	F pull axial end [kg]	ΔF pull axial [kg]	F predicted lateral breakout [kg]	F predicted axial resistance [kg]
Pull I	3.00	5.00	2.00	0.00	0.00	0.00	0.00	0.00	0.00	0.00	6.00	6.00	0.00	0.00	0.00	0.00	6.00	6.00	0.00	3.34	6.91
Pull II	5.00	6.20	1.20	0.00	0.03	0.03	0.00	2.00	4.49	6.00	6.50	6.50	0.00	0.51	0.68	0.17	6.48	6.48	0.00	3.34	6.91
Pull III	6.20	7.00	0.80	0.03	0.07	0.04	2.00	3.00	8.57	9.36	6.50	6.80	0.30	0.97	1.11	0.14	6.46	6.76	0.30	3.34	6.91
Pull IV	7.00	9.40	2.40	0.07	0.37	0.30	3.00	8.00	15.18	20.79	6.80	6.00	-0.80	1.78	2.13	0.35	6.65	5.85	-0.80	3.34	6.91

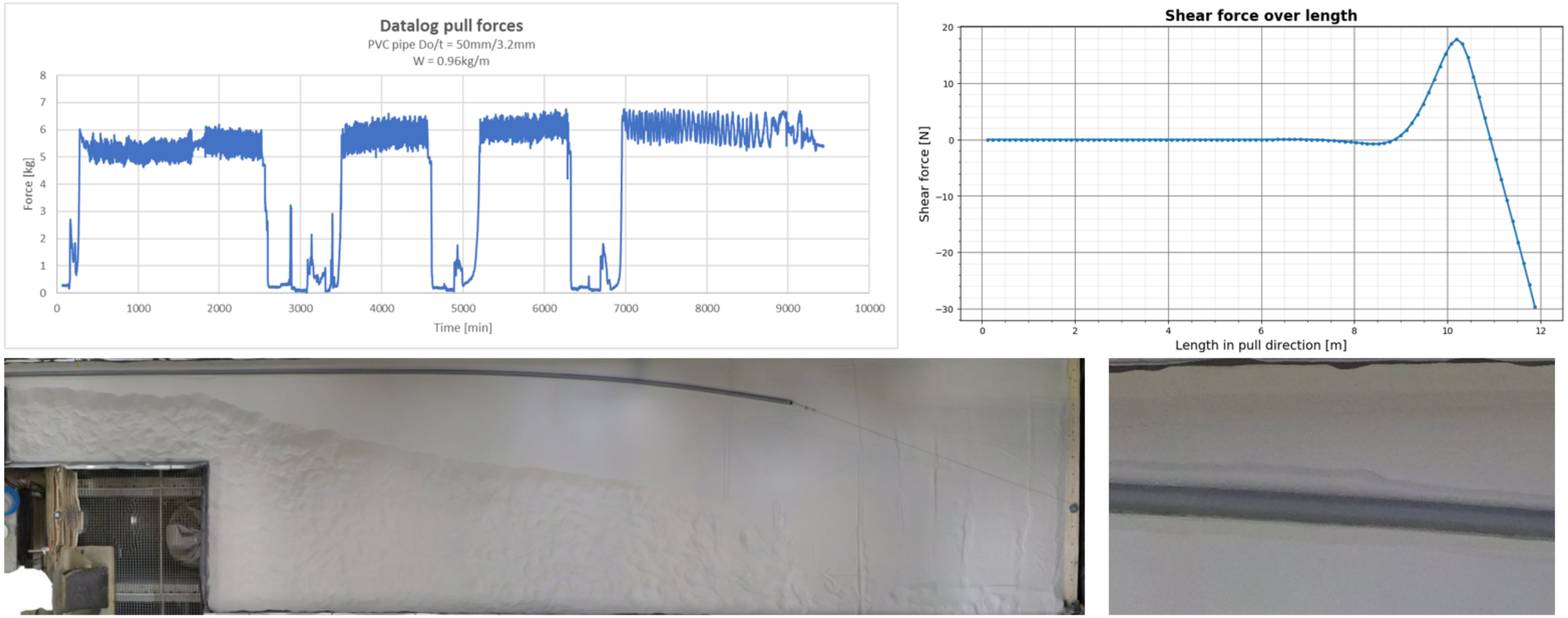

Figure B.1: Summary of experimental data;
Model $D_o/t = 50/3.2[mm]$ and $W = 0.96[kg/m]$,
Test 1

Pull No.	Xstart [m]	X end [m]	Δ X [m]	Y start [m]	Y end [m]	Δ Y [m]	θ start [°]	θ end [°]	α start [°]	α end [°]	F pull start [kg]	F pull end [kg]	Δ F pull [kg]	F pull lateral start [kg]	F pull lateral end [kg]	Δ F pull lateral [kg]	F pull axial start [kg]	F pull axial end [kg]	ΔF pull axial [kg]	F predicted lateral breakout [kg]	F predicted axial resistance [kg]
Pull I	3.00	5.00	2.00	0.00	0.00	0.00	0.00	0.00	0.00	0.00	12.00	9.00	-3.00	0.00	0.00	0.00	12.00	9.00	-3.00	3.34	6.91
Pull II	5.00	6.20	1.20	0.00	0.06	0.06	0.00	2.00	4.49	4.79	12.00	12.00	0.00	0.94	1.00	0.06	11.96	11.99	0.02	3.34	6.91
Pull III	6.20	7.00	0.80	0.06	0.12	0.06	2.00	3.00	8.30	8.87	14.00	10.00	-4.00	2.02	1.54	-0.48	13.92	9.95	-3.97	3.34	6.91
Pull IV	7.00	9.70	2.70	0.12	0.95	0.83	3.00	9.00	14.70	14.00	14.00	9.00	-5.00	3.55	2.18	-1.38	13.71	8.97	-4.74	3.34	6.91

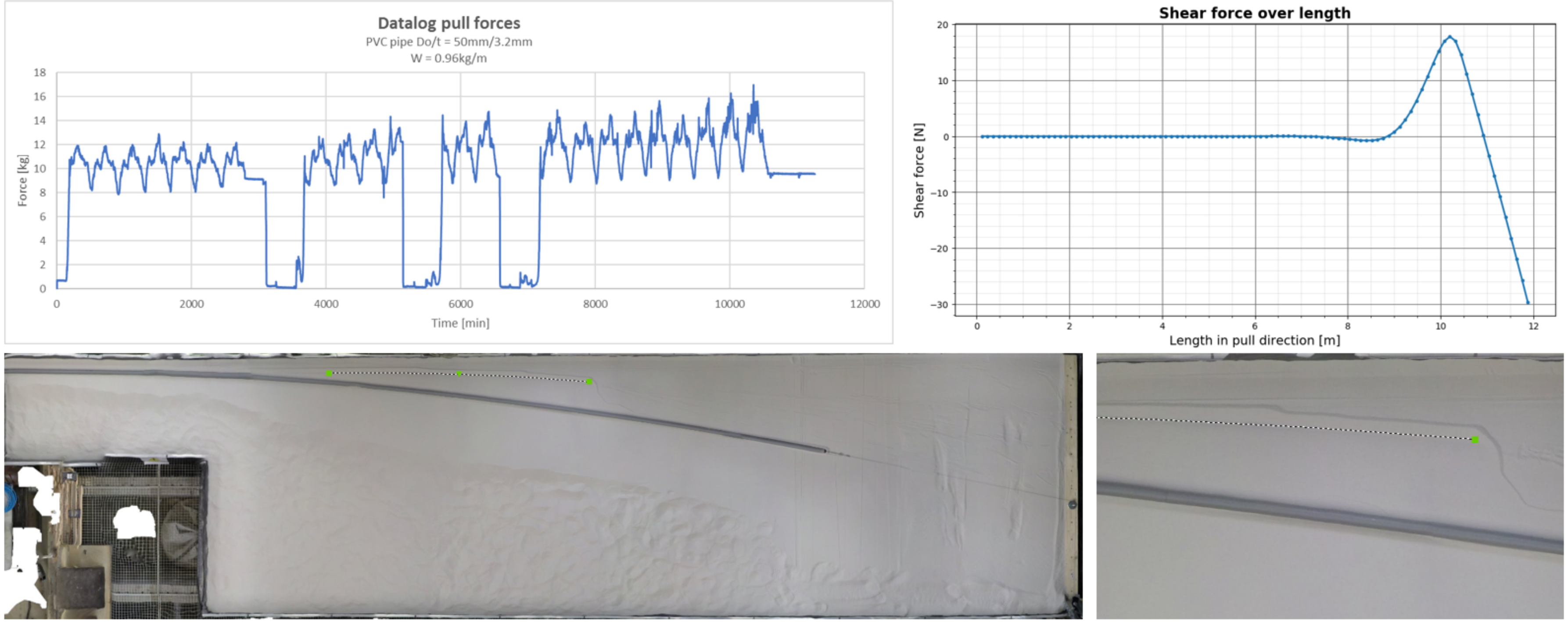

Figure B.2: Summary of experimental data;
Model $D_o/t = 50/3.2[mm]$ and $W = 0.96[kg/m]$,
Test 2

Pull No.	X start [m]	X end [m]	Δ X [m]	Y start [m]	Y end [m]	ΔY [m]	θ start [°]	θ end [°]	α start [°]	α end [°]	F pull start [kg]	F pull end [kg]	Δ F pull [kg]	F pull lateral start [kg]	F pull lateral end [kg]	Δ F pull lateral [kg]	F pull axial start [kg]	F pull axial end [kg]	Δ F pull axial [kg]	F predicted lateral breakout [kg]	F predicted axial resistance [kg]
Pull I	3.00	5.00	2.00	0.00	0.00	0.00	0.00	0.00	0.00	0.00	6.50	5.00	-1.50	0.00	0.00	0.00	6.50	5.00	-1.50	2.65	6.91
Pull II	5.00	6.20	1.20	0.00	0.05	0.05	0.00	2.00	4.49	4.88	7.00	7.00	0.00	0.55	0.60	0.05	6.98	6.99	0.01	2.65	6.91
Pull III	6.20	7.40	1.20	0.06	0.13	0.07	2.00	4.00	8.30	9.43	7.00	7.00	0.00	1.01	1.15	0.14	6.96	6.97	0.01	2.65	6.91
Pull IV	7.40	10.00	2.60	0.13	1.15	1.15	4.00	11.00	19.64	17.85	7.00	6.50	-0.50	2.35	1.99	-0.36	6.74	6.45	-0.29	2.65	6.91

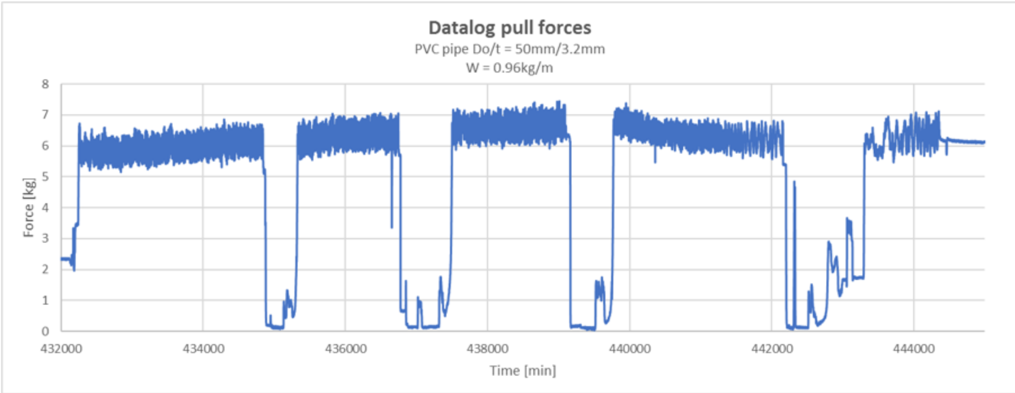

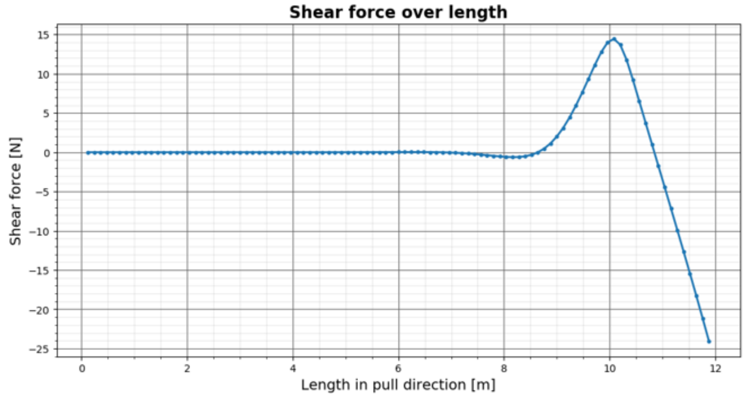

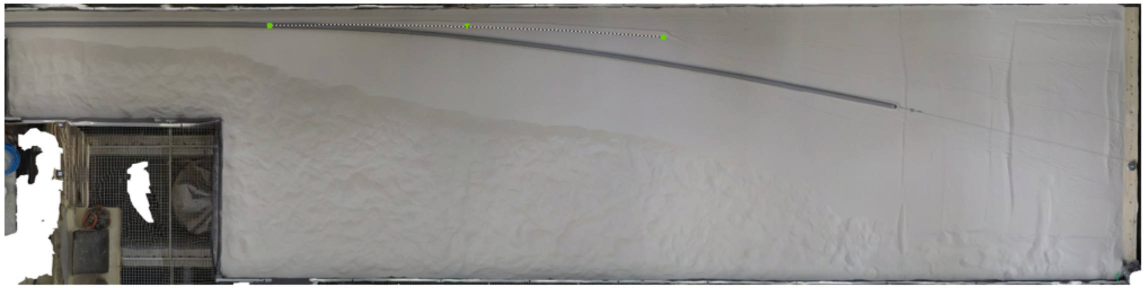

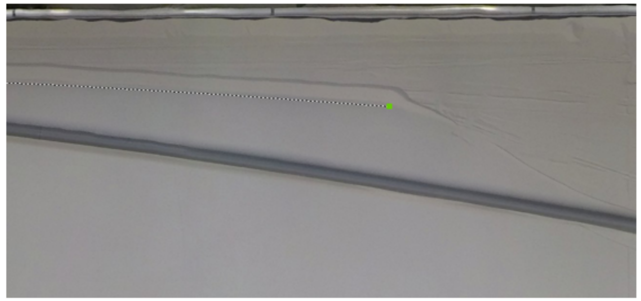

Figure B.3: Summary of experimental data;
Model $D_o/t = 50/3.2[mm]$ and $W = 0.96[kg/m]$,
Test 3

Pull No.	X start [m]	X end [m]	Δ X [m]	Y start [m]	Y end [m]	Δ Y [m]	θ start [°]	θ end [°]	α start [°]	α end [°]	F pull start [kg]	F pull end [kg]	Δ F pull [kg]	F pull lateral start [kg]	F pull lateral end [kg]	Δ F pull lateral [kg]	F pull axial start [kg]	F pull axial end [kg]	Δ F pull axial [kg]	F predicted lateral breakout [kg]	F predicted axial resistance [kg]
Pull I	3.00	4.90	1.90	0.00	0.10	0.10	0.00	2.00	3.56	3.70	6.50	6.80	0.30	0.40	0.44	0.03	6.49	6.80	0.31	2.40	6.91
Pull II	4.90	6.20	1.30	0.10	0.16	0.06	2.00	4.00	6.63	7.43	7.00	7.00	0.00	0.81	0.91	0.10	6.98	6.99	0.01	2.40	6.91
Pull III	6.20	7.60	1.40	0.16	0.77	0.61	4.00	11.00	19.18	17.92	7.00	7.00	0.00	2.30	2.15	-0.15	6.76	6.95	0.19	2.40	6.91

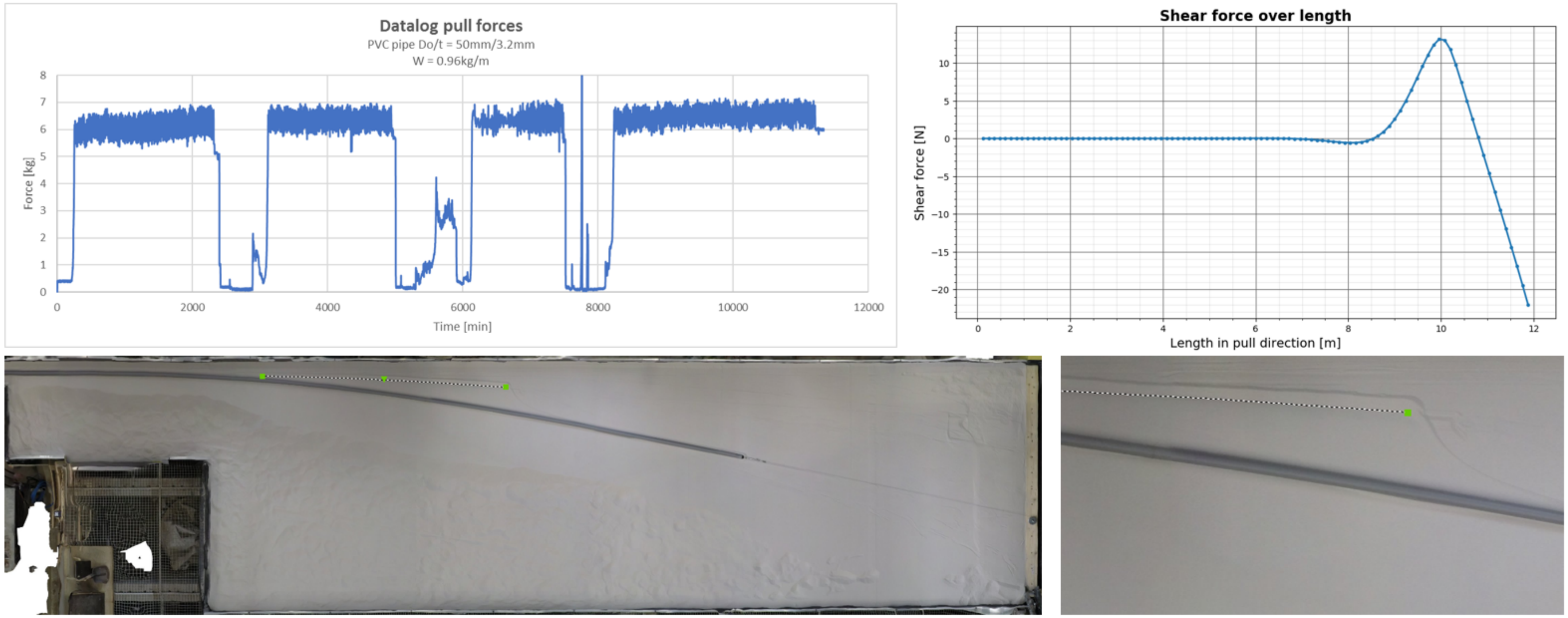

Figure B.4: Summary of experimental data;
Model $D_o/t = 50/3.2[mm]$ and $W = 0.96[kg/m]$,
Test 4

Pull No.	X start [m]	X end [m]	Δ X [m]	Y start [m]	Y end [m]	Δ Y [m]	θ start [°]	θ end [°]	α start [°]	α end [°]	F pull start [kg]	F pull end [kg]	ΔF pull [kg]	F pull lateral start [kg]	F pull lateral end [kg]	Δ F pull lateral [kg]	F pull axial start [kg]	F pull axial end [kg]	ΔF pull axial [kg]	F predicted lateral breakout [kg]	F predicted axial resistance [kg]
Pull I	3.00	4.00	1.00	0.00	0.05	0.05	0.00	2.00	2.38	2.32	6.50	6.80	0.30	0.27	0.28	0.01	6.49	6.80	0.31	2.94	6.91
Pull II	4.00	5.00	1.00	0.05	0.10	0.05	2.00	4.00	4.96	5.23	6.80	7.00	0.20	0.59	0.64	0.05	6.79	7.00	0.21	2.94	6.91
Pull III	5.00	6.00	1.00	0.10	0.16	0.06	4.00	5.00	8.19	8.90	7.00	7.00	0.00	1.00	1.08	0.09	6.98	6.98	0.00	2.94	6.91
Pull IV	6.00	7.00	1.00	0.16	0.26	1.15	5.00	7.00	12.24	13.37	7.00	7.20	0.20	1.48	1.66	0.18	6.94	7.16	0.21	2.94	6.91
Pull V	7.00	7.80	0.80	0.26	0.38	0.12	7.00	8.00	17.15	18.51	7.30	7.30	0.00	2.15	2.32	0.17	7.19	7.18	-0.01	2.94	6.91
Pull VI	7.80	10.00	2.20	0.38	1.27	1.15	8.00	14.00	22.65	23.17	7.30	7.00	-0.30	2.81	2.75	-0.06	7.06	6.91	-0.15	2.94	6.91

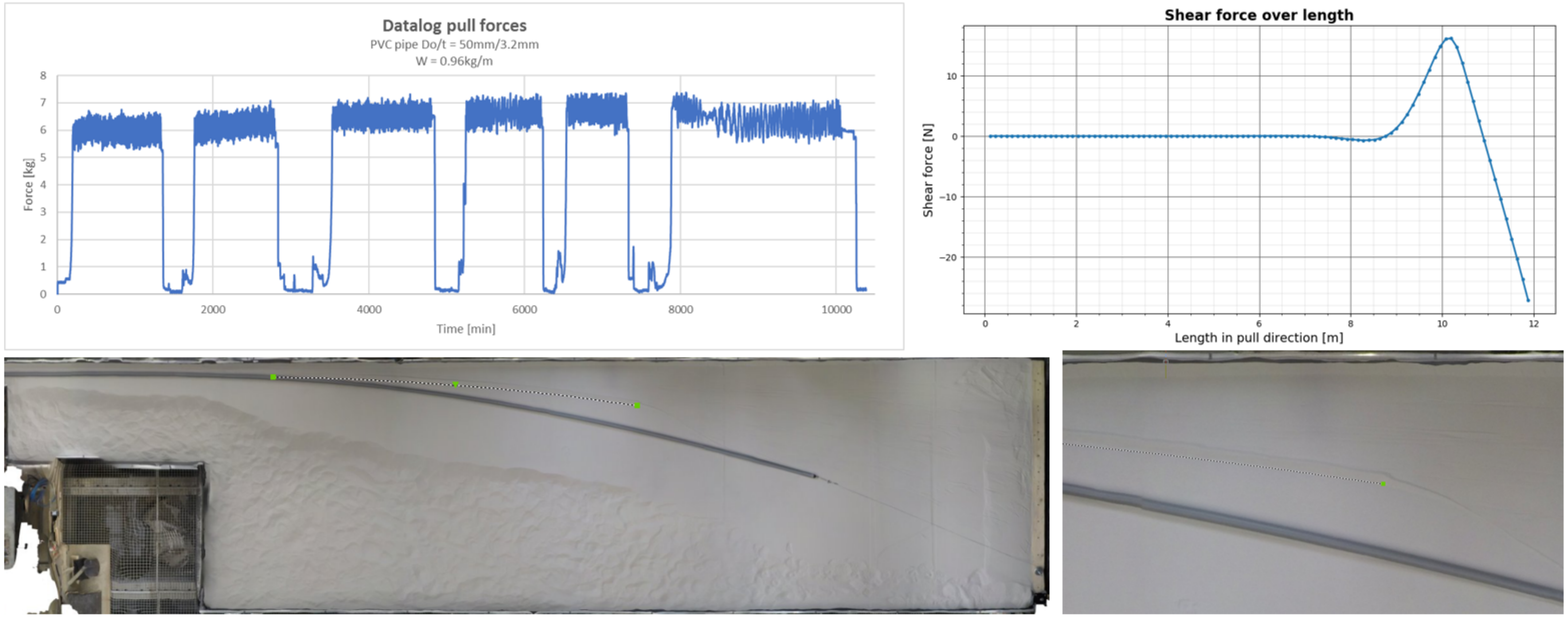

Figure B.5: Summary of experimental data;
Model $D_o/t = 50/3.2[mm]$ and $W = 0.96[kg/m]$,
Test 5

Pull No.	X start [m]	X end [m]	Δ X [m]	Y start [m]	Y end [m]	ΔY [m]	θ start [°]	θ end [°]	α start [°]	α end [°]	F pull start [kg}	F pull end [kg]	Δ F pull [kg]	F pull lateral start [kg]	F pull lateral end [kg]	Δ F pull lateral [kg]	F pull axial start [kg]	F pull axial end [kg]	Δ F pull axial [kg]	F predicted lateral breakout [kg]	F predicted axial resistance [kg]
Pull I	3.00	6.00	3.00	0.00	0.00	0.00	0.00	0.00	0.00	0.00	12.00	11.00	-1.00	0.00	0.00	0.00	12.00	11.00	-1.00	1.42	9.29
Pull II	6.00	8.00	2.00	0.00	0.15	0.15	0.00	3.00	5.16	6.00	12.00	12.00	0.00	1.08	1.25	0.17	11.95	11.98	0.03	1.42	9.29
Pull III	8.00	10.00	2.00	0.15	0.52	0.37	2.00	6.00	10.38	10.30	13.00	12.00	-1.00	2.34	2.15	-0.20	12.86	11.97	-0.90	1.42	9.29

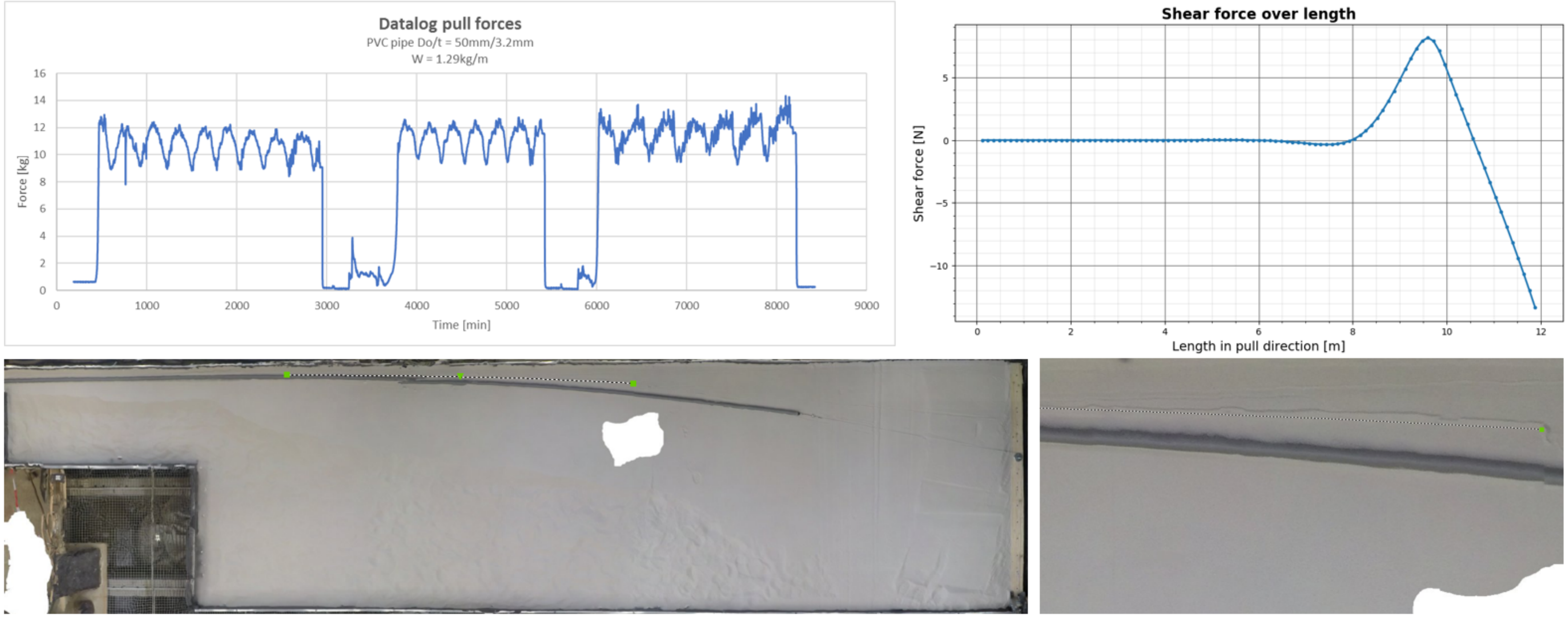

Figure B.6: Summary of experimental data;
Model $D_o/t = 50/3.2[mm]$ and $W = 1.29[kg/m]$,
Test 1

Pull No.	X start [m]	X end [m]	ΔX [m]	Y start [m]	Y end [m]	ΔY [m]	θ start [°]	θ end [°]	α start [°]	α end [°]	F pull start [kg]	F pull end [kg]	Δ F pull [kg]	F pull lateral start [kg]	F pull lateral end [kg]	Δ F pull lateral [kg]	F pull axial start [kg]	F pull axial end [kg]	Δ F pull axial [kg]	F predicted lateral breakout [kg]	F predicted axial resistance [kg]
Pull I	3.00	4.30	1.30	0.00	0.03	0.03	0.00	3.00	2.38	2.54	9.00	9.50	0.50	0.37	0.42	0.05	8.99	9.50	0.51	3.34	9.29
Pull II	4.30	6.20	1.90	0.03	0.15	0.12	3.00	6.00	7.99	9.26	10.00	10.00	0.00	1.39	1.61	0.22	9.96	9.98	0.02	3.34	9.29
Pull III	6.20	8.00	1.80	0.15	0.36	0.21	6.00	7.00	12.69	14.96	10.00	10.00	0.00	2.20	2.58	0.39	9.93	9.90	-0.03	3.34	9.29
Pull IV	8.00	8.80	0.80	0.36	0.50	0.14	7.00	9.00	19.47	14.00	10.00	10.00	0.00	3.33	2.42	-0.91	9.76	9.96	0.20	3.34	9.29
Pull V	8.80	10.40	1.60	0.50	1.29	0.79	9.00	18.00	28.67	14.00	9.00	9.00	0.00	4.32	2.18	-2.14	8.47	8.98	0.50	3.34	9.29

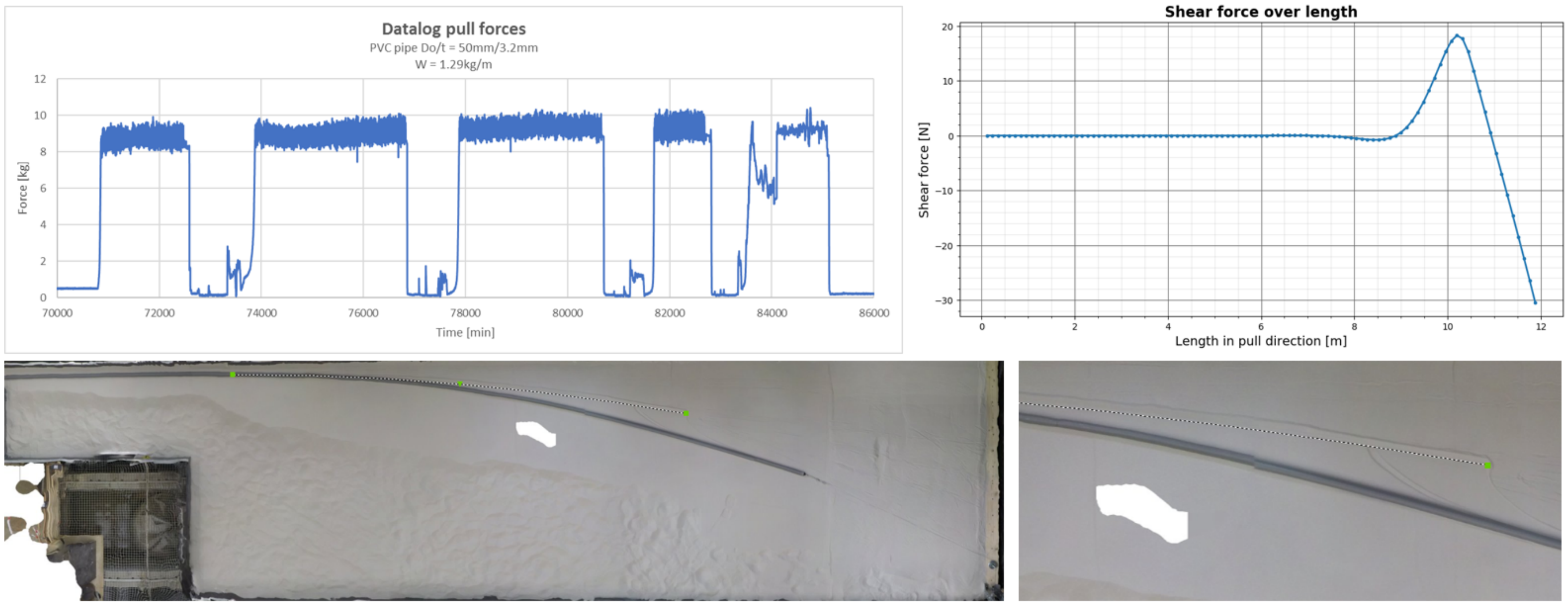

Figure B.7: Summary of experimental data;
Model $D_o/t = 50/3.2[mm]$ and $W = 1.29[kg/m]$,
Test 2

Pull No.	X start [m]	X end [m]	Δ X [m]	Y start [m]	Y end [m]	Δ Y [m]	θ start [°]	θ end [°]	α start [°]	α end [°]	F pull start [kg]	F pull end [kg]	Δ F pull [kg]	F pull lateral start [kg]	F pull lateral end [kg]	Δ F pull lateral [kg]	F pull axial start [kg]	F pull axial end [kg]	Δ F pull axial [kg]	F predicted lateral breakout [kg]	F predicted axial resistance [kg]
Pull I	3.00	5.40	2.40	0.00	0.14	0.14	0.00	2.00	2.38	2.06	9.00	9.00	0.00	0.37	0.32	-0.05	8.99	9.00	0.01	1.96	9.29
Pull II	5.40	6.90	1.50	0.14	0.19	0.05	2.00	5.00	5.21	6.07	9.00	9.50	0.50	0.82	1.00	0.19	8.99	9.50	0.51	1.96	9.29
Pull III	6.90	8.10	1.20	0.06	0.31	0.25	5.00	7.00	11.23	11.09	10.00	9.50	-0.50	1.95	1.83	-0.12	9.94	9.48	-0.47	1.96	9.29
Pull IV	8.10	11.40	3.30	0.31	1.64	1.33	7.00	16.00	22.60	24.30	8.50	10.00	1.50	3.27	4.12	0.85	8.19	9.90	1.71	1.96	9.29

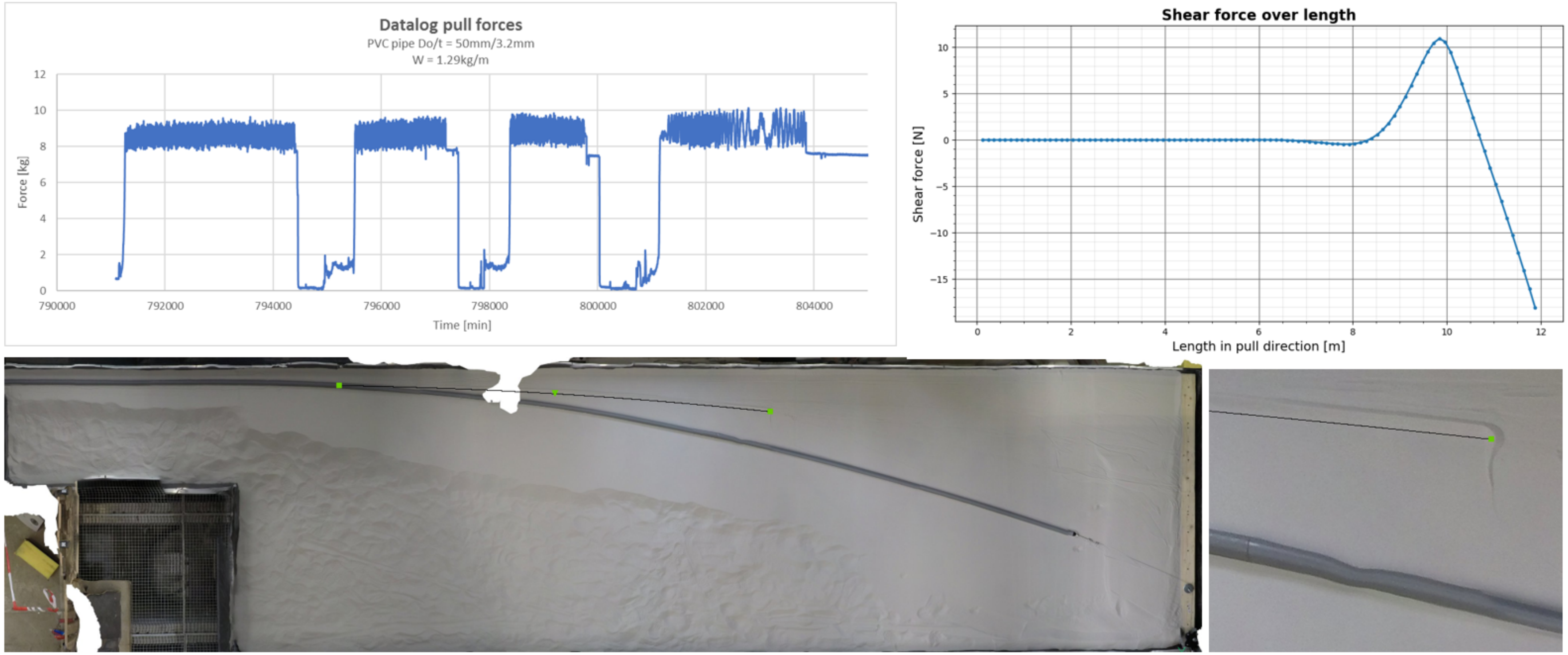

Figure B.8: Summary of experimental data;
Model $D_o/t = 50/3.2[mm]$ and $W = 1.29[kg/m]$,
Test 3

Pull No.	X start [m]	X end [m]	Δ X [m]	Y start [m]	Y end [m]	ΔY [m]	θ start [°]	θ end [°]	α start [°]	α end [°]	F pull start [kg]	F pull end [kg]	Δ F pull [kg]	F pull lateral start [kg]	F pull lateral end [kg]	Δ F pull lateral [kg]	F pull axial start [kg]	F pull axial end [kg]	Δ F pull axial [kg]	F predicted lateral breakout [kg]	F predicted axial resistance [kg]
Pull I	3.00	5.40	2.40	0.00	0.14	0.14	0.00	2.00	2.38	2.06	9.00	9.00	0.00	0.37	0.32	-0.05	8.99	9.00	0.01	1.96	9.29
Pull II	5.40	6.90	1.50	0.14	0.19	0.05	2.00	5.00	5.21	6.07	9.00	9.50	0.50	0.82	1.00	0.19	8.99	9.50	0.51	1.96	9.29
Pull III	6.90	8.10	1.20	0.06	0.31	0.25	5.00	7.00	11.23	11.09	10.00	9.50	-0.50	1.95	1.83	-0.12	9.94	9.48	-0.47	1.96	9.29
Pull IV	8.10	11.40	3.30	0.31	1.64	1.33	7.00	16.00	22.60	24.30	8.50	10.00	1.50	3.27	4.12	0.85	8.19	9.90	1.71	1.96	9.29

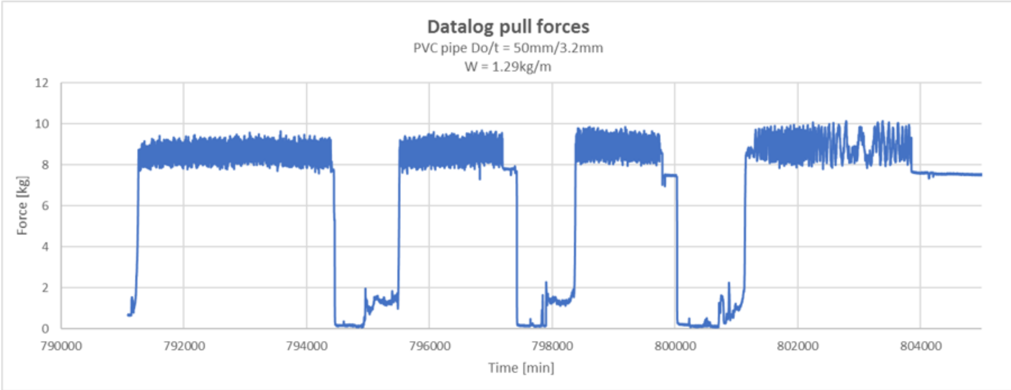

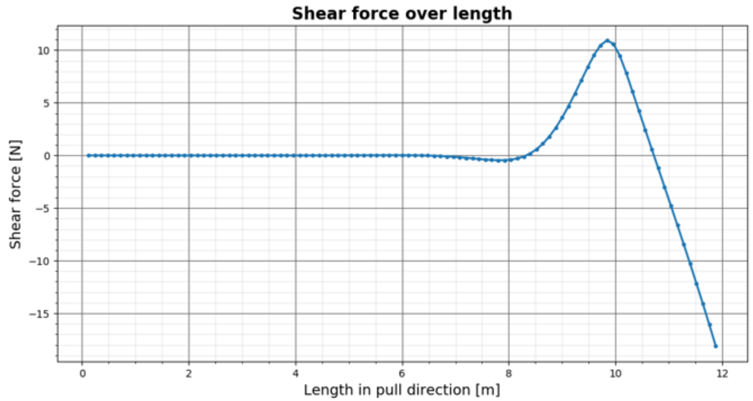

Figure B.9: Summary of experimental data;
Model $D_o/t = 50/3.2[mm]$ and $W = 1.29[kg/m]$,
Test 3

Pull No.	X start [m]	X end [m]	Δ X [m]	Y start [m]	Y end [m]	Δ Y [m]	θ start [°]	θ end [°]	α start [°]	α end [°]	F pull start [kg]	F pull end [kg]	Δ F pull [kg]	F pull lateral start [kg]	F pull lateral end [kg]	ΔF pull lateral [kg]	F pull axial start [kg]	F pull axial end [kg]	Δ F pull axial [kg]	F predicted lateral breakout [kg]	F predicted axial resistance [kg]
Pull I	3.00	4.90	1.90	0.00	0.14	0.14	0.00	3.00	2.38	1.92	9.00	9.50	0.50	0.37	0.32	-0.05	8.99	9.50	0.51	2.26	9.29
Pull II	4.90	6.00	1.10	0.14	0.19	0.05	3.00	5.00	6.34	6.96	9.50	9.50	0.00	1.05	1.15	0.10	9.48	9.49	0.01	2.26	9.29
Pull III	6.00	7.40	1.40	0.06	0.31	0.25	5.00	7.00	13.06	13.83	10.00	10.00	0.00	2.26	2.39	0.13	9.90	9.93	0.03	2.26	9.29
Pull IV	7.40	10.00	2.60	0.31	1.64	1.33	7.00	15.00	19.83	11.98	10.00	10.00	0.00	3.39	2.08	-1.32	9.75	9.99	0.24	2.26	9.29

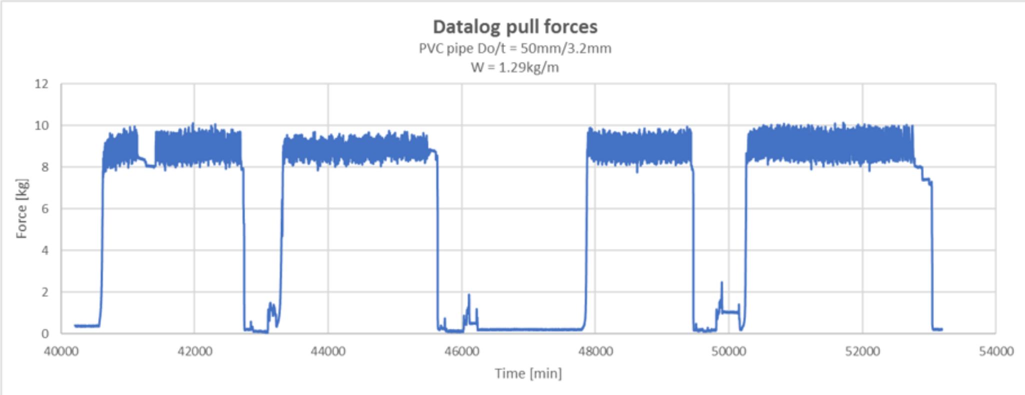

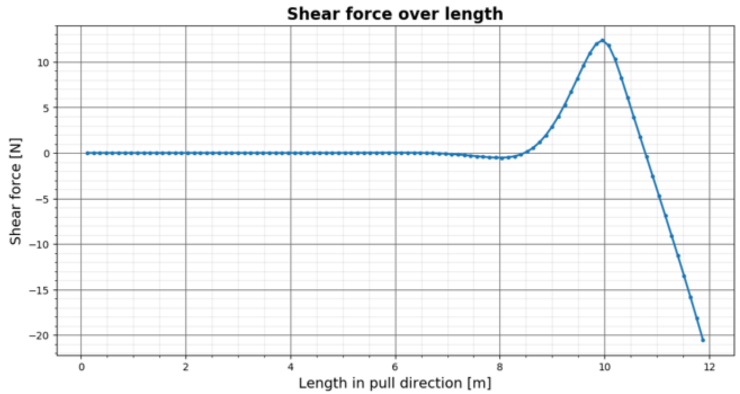

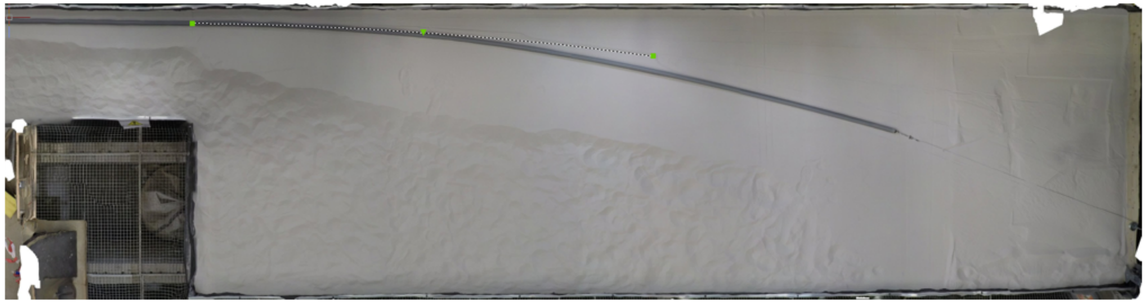

Figure B.10: Summary of experimental data;
Model $D_o/t = 50/3.2[mm]$ and $W = 1.29[kg/m]$,
Test 4

Pull No.	X start [m]	X end [m]	ΔX [m]	Y start [m]	Y end [m]	Δ Y [m]	θ start [°]	θ end [°]	α start [°]	α end [°]	F pull start [kg]	F pull end [kg]	Δ F pull [kg]	F pull lateral start [kg]	F pull lateral end [kg]	ΔF pull lateral [kg]	F pull axial start [kg]	F pull axial end [kg]	ΔF pull axial [kg]	F predicted lateral breakout [kg]	F predicted axial resistance [kg]
Pull I	3.00	5.00	2.00	0.00	0.00	0.00	0.00	0.00	0.00	0.00	11.00	11.00	0.00	0.00	0.00	0.00	11.00	11.00	0.00	3.24	11.66
Pull II	5.00	7.00	2.00	0.00	0.05	0.05	0.00	2.00	3.00	3.55	11.00	12.00	1.00	0.58	0.74	0.17	10.98	12.00	1.01	3.24	11.66
Pull III	7.00	8.80	1.80	0.06	0.12	0.06	2.00	7.00	7.47	10.04	12.00	12.50	0.50	1.56	2.18	0.62	11.95	12.48	0.54	3.24	11.66
Pull IV	8.80	10.80	2.00	0.12	0.48	0.36	7.00	12.00	12.91	15.78	14.00	15.00	1.00	3.13	4.08	0.95	13.93	14.97	1.04	3.24	11.66

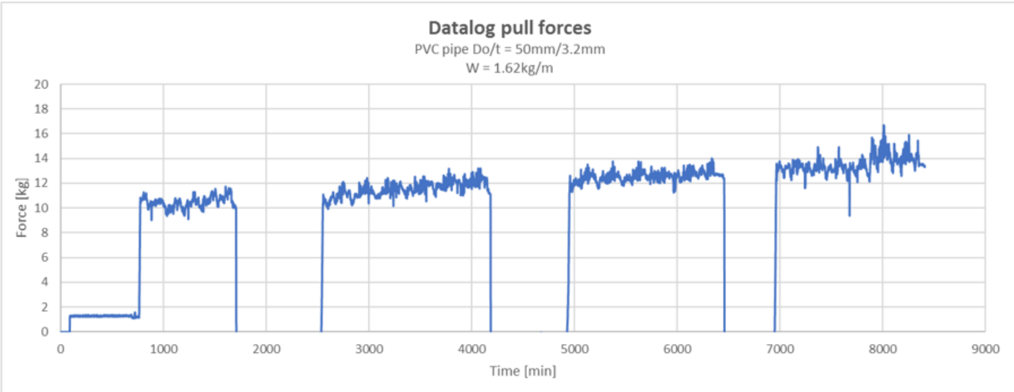

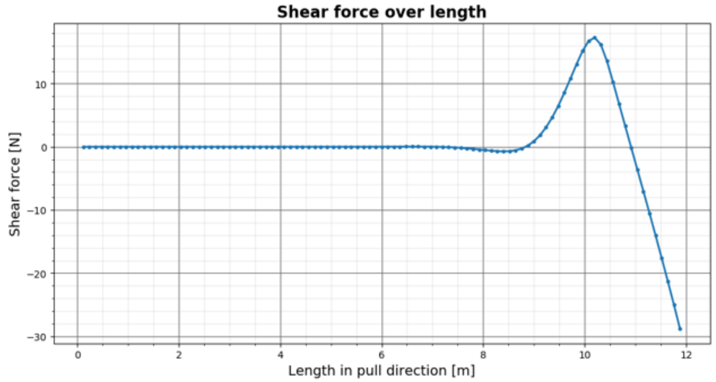

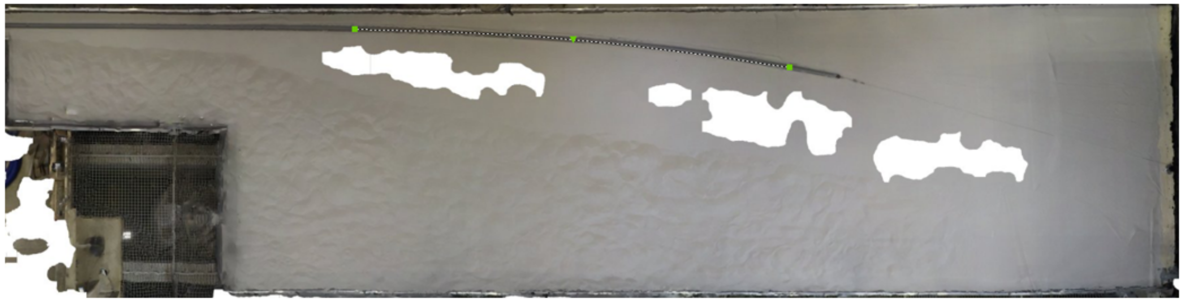

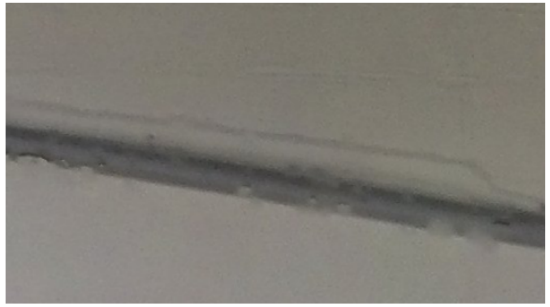

Figure B.11: Summary of experimental data;
Model $D_o/t = 50/3.2[mm]$ and $W = 1.62[kg/m]$,
Test 1

Pull No.	X start [m]	X end [m]	ΔX [m]	Y start [m]	Y end [m]	ΔY [m]	θ start [°]	θ end [°]	α start [°]	α end [°]	F pull start [kg]	F pull end [kg]	Δ F pull [kg]	F pull lateral start [kg]	F pull lateral end [kg]	ΔF pull lateral [kg]	F pull axial start [kg]	F pull axial end [kg]	ΔF pull axial [kg]	F predicted lateral breakout [kg]	F predicted axial resistance [kg]
Pull I	3.00	5.00	2.00	0.00	0.08	0.08	0.00	2.00	2.38	2.40	12.00	13.00	1.00	0.50	0.54	0.05	11.99	13.00	1.01	3.43	11.66
Pull II	5.00	6.00	1.00	0.08	0.12	0.04	2.00	4.00	5.38	5.85	12.00	13.00	1.00	1.13	1.32	0.20	11.98	12.99	1.01	3.43	11.66
Pull III	6.00	7.40	1.40	0.06	0.21	0.15	4.00	6.00	8.06	8.57	14.00	14.00	0.00	1.96	2.09	0.12	13.96	13.99	0.02	3.43	11.66
Pull IV	7.40	8.50	1.10	0.21	0.37	0.16	6.00	8.00	10.70	11.34	15.00	14.00	-1.00	2.78	2.75	-0.03	14.95	13.98	-0.97	3.43	11.66
Pull V	8.50	9.10	0.60	0.37	0.54	0.17	8.00	9.00	16.55	16.67	14.00	13.00	-1.00	3.99	3.73	-0.26	13.84	12.88	-0.96	3.43	11.66

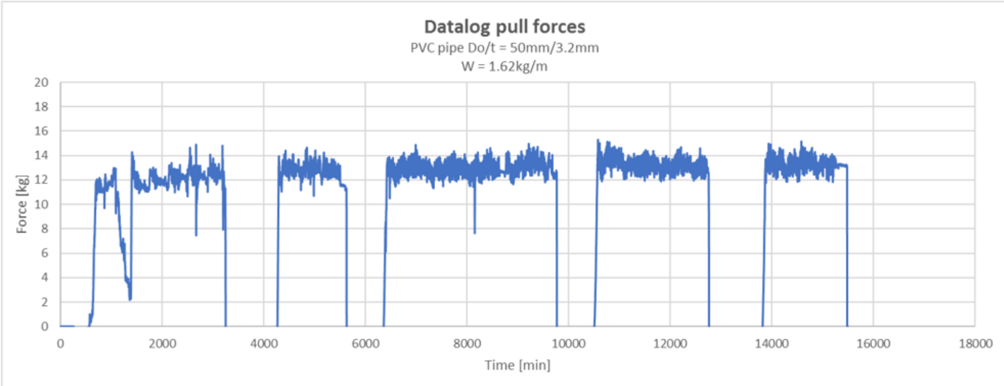

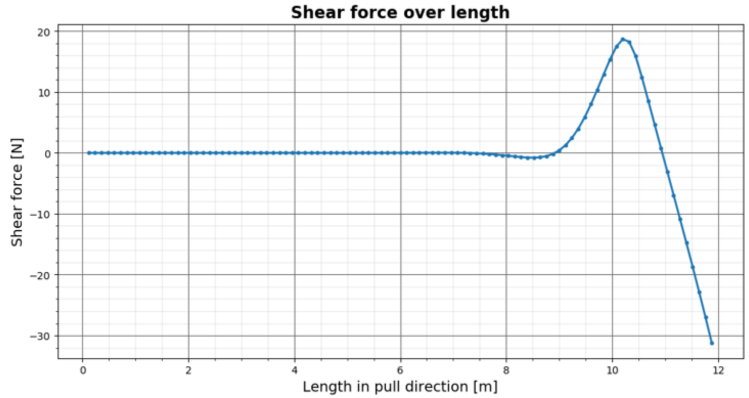

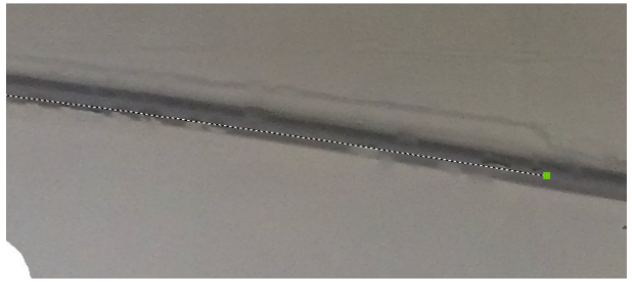

Figure B.12: Summary of experimental data;
Model $D_o/t = 50/3.2[mm]$ and $W = 1.62[kg/m]$,
Test 2

Pull No.	X start [m]	X end [m]	Δ X [m]	Y start [m]	Y end [m]	Δ Y [m]	θ start [°]	θ end [°]	α start [°]	α end [°]	F pull start [kg]	F pull end [kg]	Δ F pull [kg]	F pull lateral start [kg]	F pull lateral end [kg]	Δ F pull lateral [kg]	F pull axial start [kg]	F pull axial end [kg]	Δ F pull axial [kg]	F predicted lateral breakout [kg]	F predicted axial resistance [kg]
Pull I	3.00	5.00	2.00	0.00	0.02	0.02	0.00	1.00	2.38	2.85	11.00	11.00	0.00	0.46	0.55	0.09	10.99	10.99	0.00	1.86	11.66
Pull II	5.00	7.00	2.00	0.02	0.10	0.08	1.00	4.00	5.83	7.07	12.00	13.00	1.00	1.22	1.60	0.38	11.96	12.98	1.02	1.86	11.66
Pull III	7.00	8.20	1.20	0.06	0.44	0.38	4.00	7.00	11.43	9.71	15.00	13.00	-2.00	2.97	2.19	-0.78	14.87	12.99	-1.89	1.86	11.66
Pull IV	8.20	11.20	3.00	0.44	1.61	1.17	7.00	15.00	19.36	15.15	13.00	12.50	-0.50	4.31	3.27	-1.04	12.70	12.50	-0.20	1.86	11.66

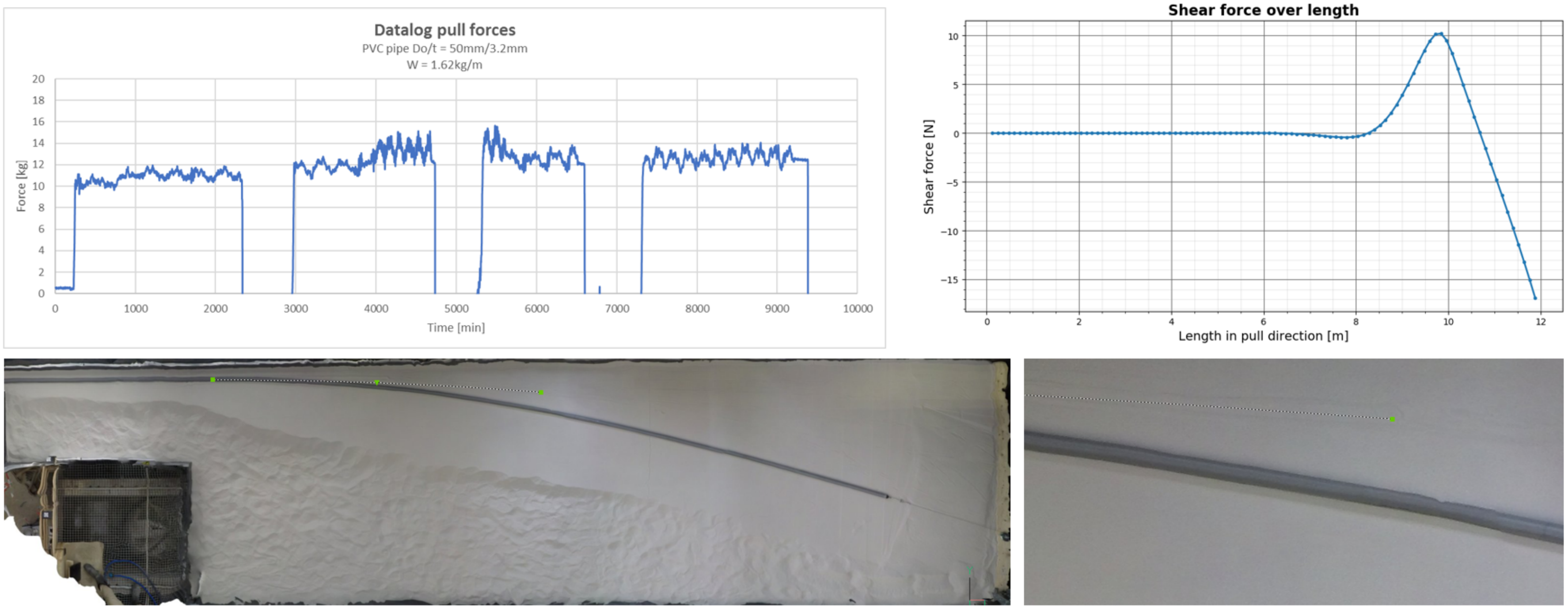

Figure B.13: Summary of experimental data; Model $D_o/t = 50/3.2[mm]$ and $W = 1.62[kg/m]$, Test 3

Pull No.	X start [m]	X end [m]	ΔX [m]	Y start [m]	Y end [m]	ΔY [m]	θ start [°]	θ end [°]	α start [°]	α end [°]	F pull start [kg}	F pull end [kg]	ΔF pull [kg]	F pull lateral start [kg]	F pull lateral end [kg]	Δ F pull lateral [kg]	F pull axial start [kg]	F pull axial end [kg]	ΔF pull axial [kg]	F predicted lateral breakout [kg]	F predicted axial resistance [kg]
Pull I	3.00	5.00	2.00	0.00	0.08	0.08	0.00	3.00	2.38	2.40	12.00	12.00	0.00	0.50	0.50	0.00	11.99	12.00	0.01	3.43	11.66
Pull II	5.00	7.00	2.00	0.08	0.22	0.14	3.00	5.00	5.38	5.87	12.00	12.00	0.00	1.13	1.23	0.10	11.99	12.00	0.01	3.43	11.66
Pull III	7.00	8.20	1.20	0.22	1.08	0.86	5.00	12.00	9.86	1.55	12.00	12.00	0.00	2.05	0.32	-1.73	11.96	11.80	-0.16	3.43	11.66

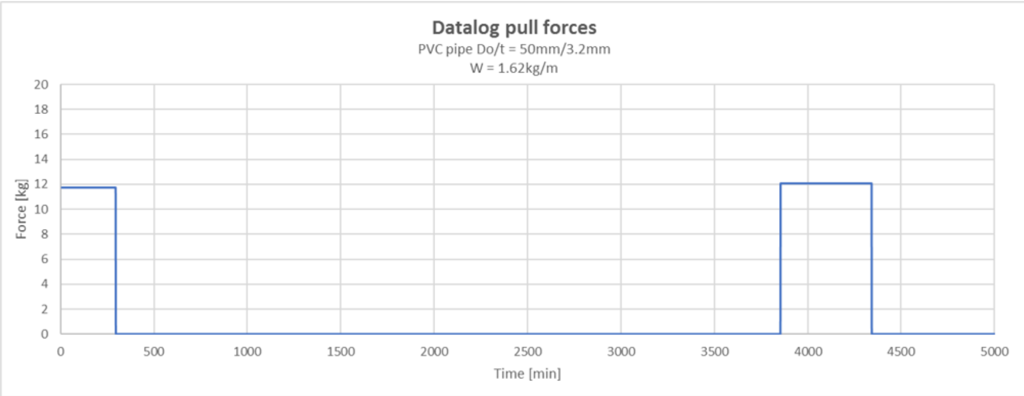

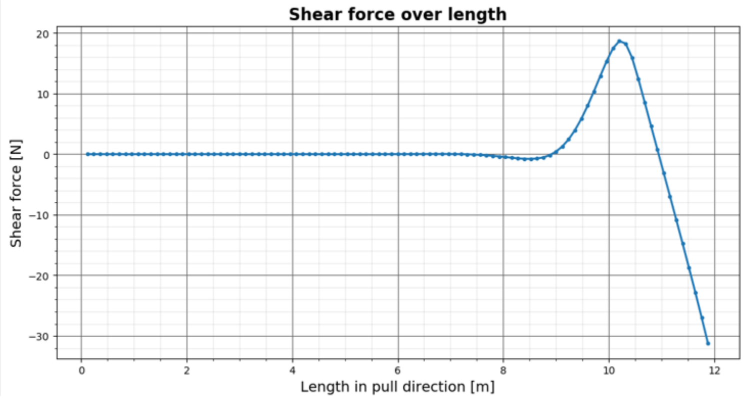

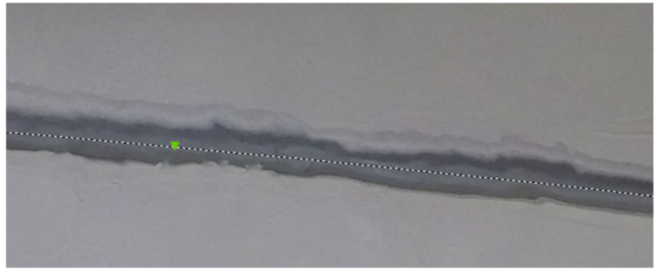

Figure B.14: Summary* of experimental data;
Model $D_o/t = 50/3.2[mm]$ and $W = 1.62[kg/m]$,
Test 4

* PLEASE NOTE: This pull data log is only indicative since an malfunction of the data logging appeared.

Pull No.	X start [m]	X end [m]	Δ X [m]	Y start [m]	Y end [m]	Δ Y [m]	θ start [°]	θ end [°]	α start [°]	α end [°]	F pull start [kg]	F pull end [kg]	Δ F pull [kg]	F pull lateral start [kg]	F pull lateral end [kg]	Δ F pull lateral [kg]	F pull axial start [kg]	F pull axial end [kg]	Δ F pull axial [kg]	F predicted lateral breakout [kg]	F predicted axial resistance [kg]
Pull I	3.00	5.00	2.00	0.00	0.08	0.08	0.00	3.00	2.38	2.40	13.00	13.00	0.00	0.54	0.54	0.01	12.99	13.00	0.01	3.43	11.66
Pull II	5.00	7.00	2.00	0.08	0.22	0.14	3.00	5.00	5.38	5.87	14.00	12.00	-2.00	1.31	1.23	-0.09	13.99	12.00	-1.99	3.43	11.66
Pull III	7.00	8.20	1.20	0.22	1.08	0.86	5.00	12.00	11.82	4.12	14.00	13.50	-0.50	2.87	0.97	-1.90	13.90	13.37	-0.53	3.43	11.66

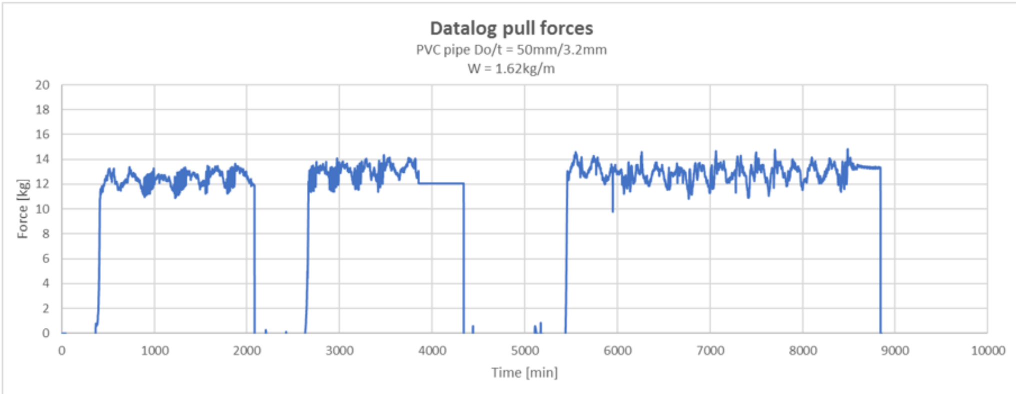

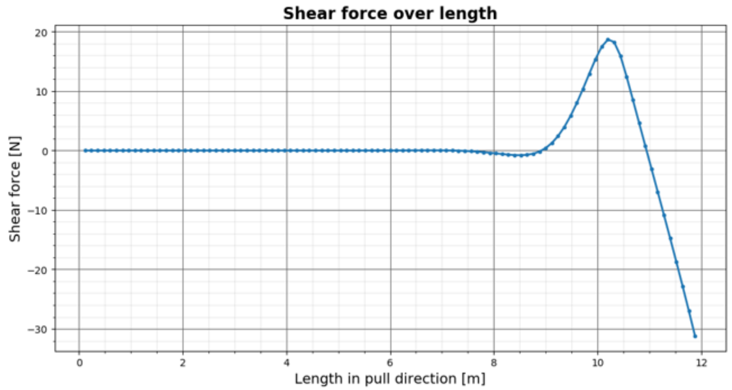

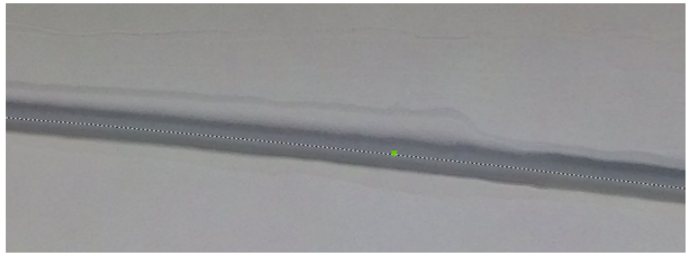

Figure B.15: Summary of experimental data;
Model $D_o/t = 50/3.2[mm]$ and $W = 1.62[kg/m]$,
Test 5

Pull No.	X start [m]	Xend [m]	ΔX [m]	Y start [m]	Y end [m]	ΔY [m]	θ start [°]	θ end [°]	α start [°]	α end [°]	F pull start [kg]	F pull end [kg]	ΔF pull [kg]	F pull lateral start [kg]	F pull lateral end [kg]	ΔF pull lateral [kg]	F pull axial start [kg]	F pull axial end [kg]	ΔF pull axial [kg]	F predicted lateral breakout [kg]	F predicted axial resistance [kg]
Pull I	3.00	5.00	2.00	0.00	0.07	0.07	0.00	2.00	2.38	2.47	13.00	13.50	0.50	0.54	0.58	0.04	12.99	13.50	0.51	2.65	11.66
Pull II	5.00	6.00	1.00	0.07	0.17	0.10	2.00	4.00	5.46	5.42	14.50	13.50	-1.00	1.38	1.28	-0.10	14.47	13.50	-0.98	2.65	11.66
Pull III	6.00	8.20	2.20	0.17	0.31	0.14	4.00	6.00	10.49	13.79	16.00	13.00	-3.00	2.91	3.10	0.19	15.90	12.88	-3.02	2.65	11.66
Pull IV	8.20	11.40	3.20	0.31	1.19	0.88	6.00	10.00	16.20	18.30	15.00	14.50	-0.50	4.19	4.55	0.37	14.76	14.35	-0.41	2.65	11.66

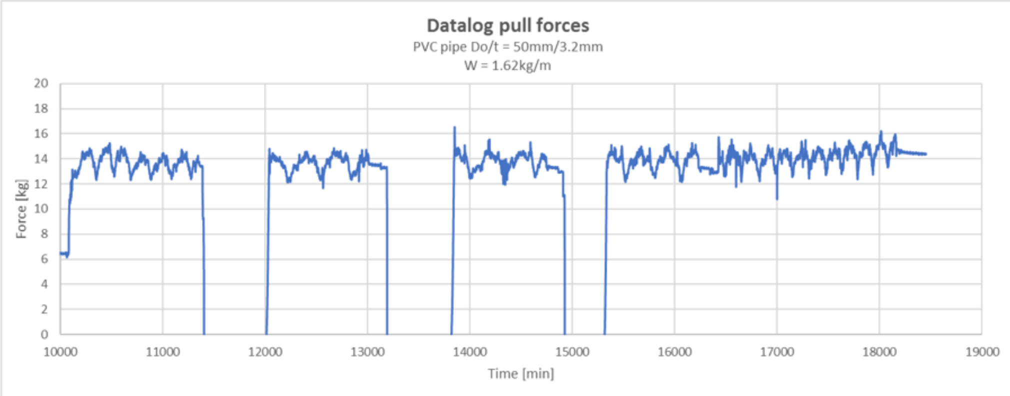

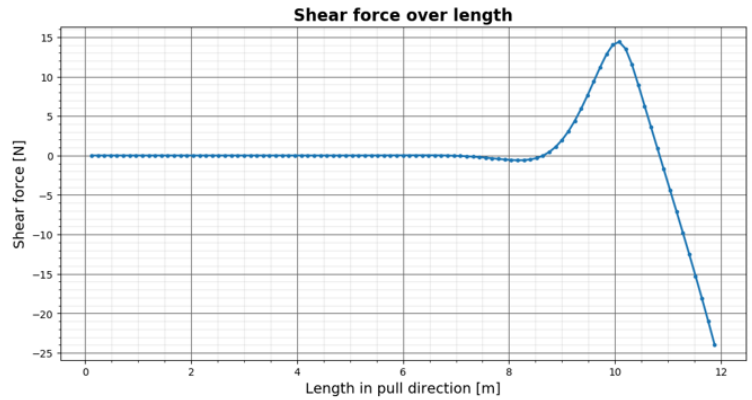

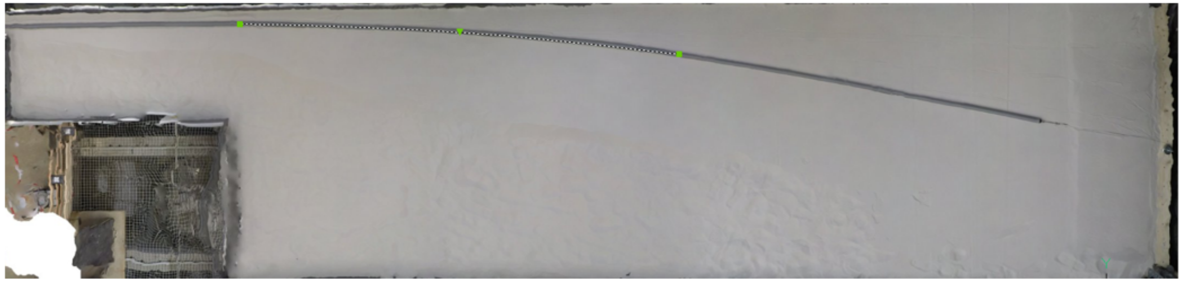

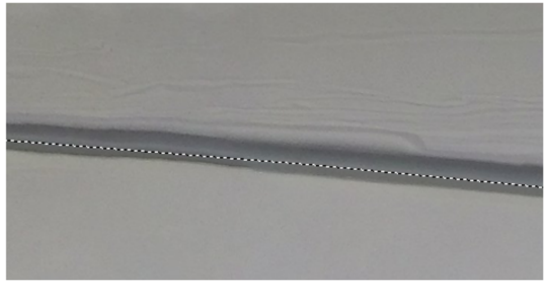

Figure B.16: Summary of experimental data;
Model $D_o/t = 50/3.2[mm]$ and $W = 1.62[kg/m]$,
Test 6

Pull No.	X start [m]	X end [m]	Δ X [m]	Y start [m]	Y end [m]	Δ Y [m]	θ start [°]	θ end [°]	α start [°]	α end [°]	F pull start [kg]	F pull end [kg]	Δ F pull [kg]	F pull lateral start [kg]	F pull lateral end [kg]	Δ F pull lateral [kg]	F pull axial start [kg]	F pull axial end [kg]	Δ F pull axial [kg]	F predicted lateral breakout [kg]	F predicted axial resistance [kg]
Pull I	3.00	5.00	2.00	0.00	0.07	0.07	0.00	3.00	2.38	2.47	13.00	13.00	0.00	0.54	0.56	0.02	12.99	13.00	0.01	2.11	11.66
Pull II	5.00	7.00	2.00	0.07	0.33	0.26	3.00	5.00	5.46	4.76	12.00	13.00	1.00	1.14	1.08	-0.06	11.99	13.00	1.01	2.11	11.66
Pull III	7.00	11.40	4.40	0.33	1.15	0.82	10.00	6.00	12.69	19.95	13.00	13.00	0.00	2.86	4.43	1.58	12.99	12.62	-0.37	2.11	11.66

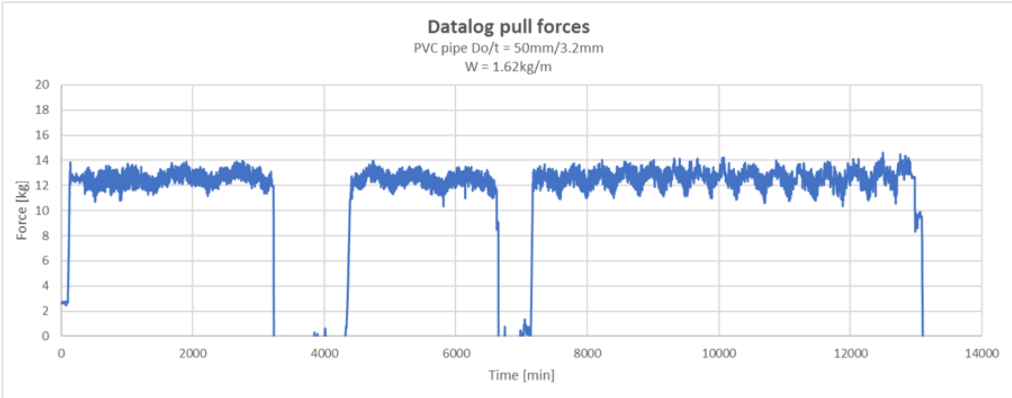

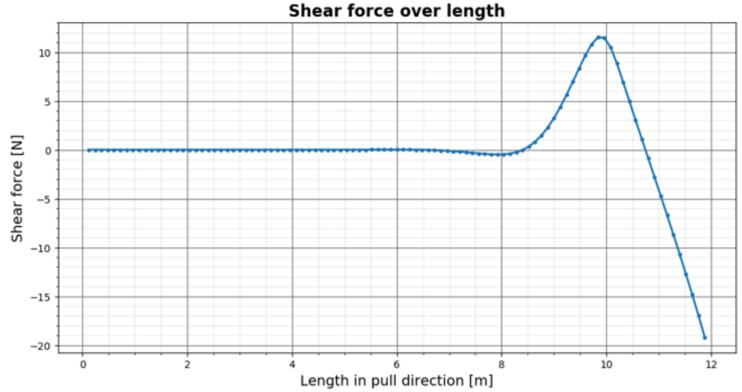

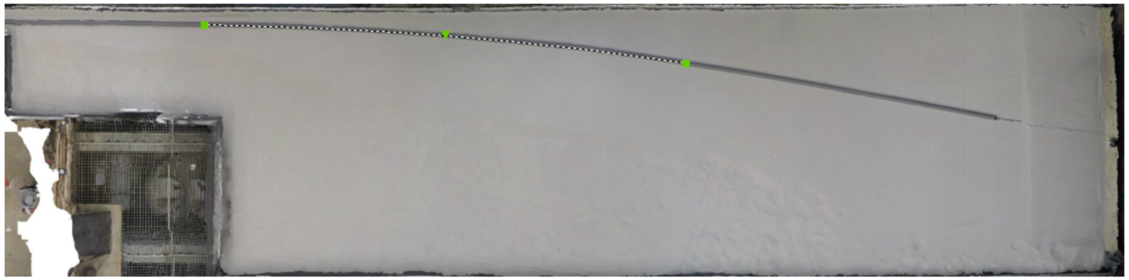

Figure B.17: Summary of experimental data; Model $D_o/t = 50/3.2[mm]$ and $W = 1.62[kg/m]$, Test 7

Pull No.	X start [m]	X end [m]	Δ X [m]	Y start [m]	Y end [m]	Δ Y [m]	θ start [°]	θ end [°]	α start [°]	α end [°]	F pull start [kg]	F pull end [kg]	Δ F pull [kg]	F pull lateral start [kg]	F pull lateral end [kg]	Δ F pull lateral [kg]	F pull axial start [kg]	F pull axial end [kg]	Δ F pull axial [kg]	F predicted lateral breakout [kg]	F predicted axial resistance [kg]
Pull I	3.00	5.00	2.00	0.00	0.10	0.10	0.00	2.00	0.00	-0.75	13.00	14.00	1.00	0.00	-0.18	-0.18	13.00	13.98	0.98	2.11	11.66
Pull II	5.00	6.00	1.00	0.10	0.14	0.04	2.00	4.00	3.74	3.96	14.00	14.00	0.00	0.91	0.97	0.05	13.99	14.00	0.01	2.11	11.66
Pull III	6.00	10.50	4.50	0.14	0.69	0.55	4.00	8.00	7.38	8.24	14.00	14.00	0.00	1.80	2.01	0.21	13.98	14.00	0.02	2.11	11.66

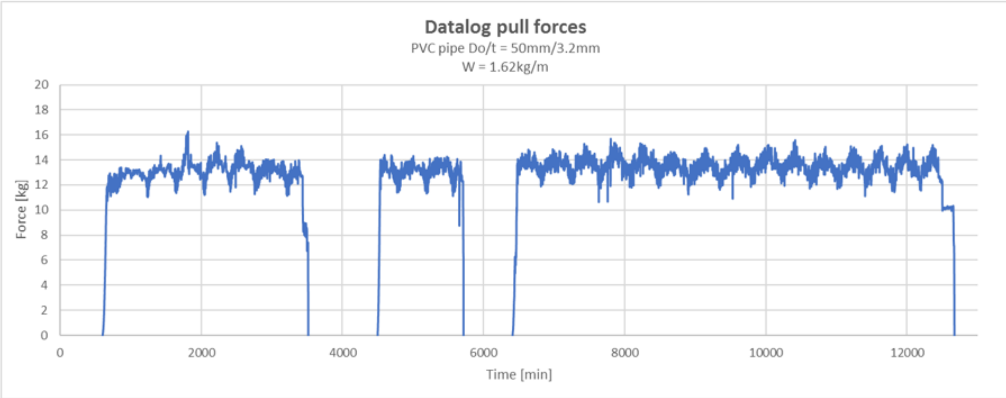

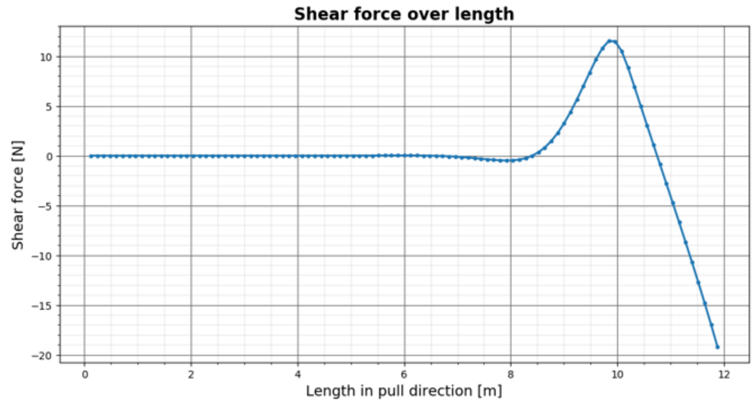

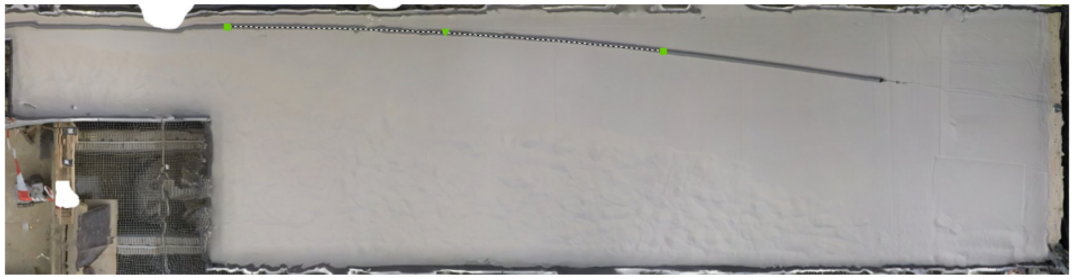

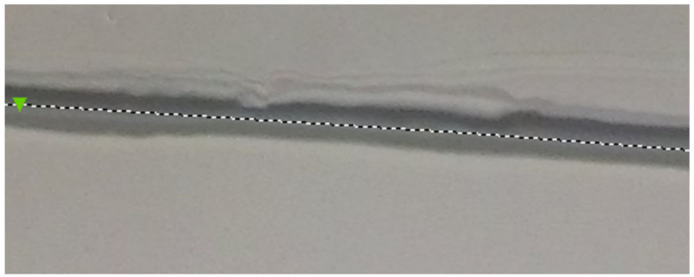

Figure B.18: Summary of experimental data;
Model $D_o/t = 50/3.2[mm]$ and $W = 1.62[kg/m]$,
Test 8

C

Summary experimental data $D_o/t = 110/3.2[mm]$ model

Pull No.	X start [m]	X end [m]	Δ X [m]	Y start [m]	Y end [m]	Δ Y [m]	θ start [°]	θ end [°]	α start [°]	α end [°]	F pull start [kg]	F pull end [kg]	Δ F pull [kg]	F pull lateral start [kg]	F pull lateral end [kg]	Δ F pull lateral [kg]	F pull axial start [kg]	F pull axial end [kg]	Δ F pull axial [kg]	F predicted lateral breakout [kg]	F predicted axial resistance [kg]
Pull I	3.00	5.00	2.00	0.00	0.00	0.00	0.00	0.00	0.00	0.00	46.00	45.00	-1.00	0.00	0.00	0.00	46.00	45.00	-1.00	14.72	60.48
Pull II	5.00	6.40	1.40	0.00	0.05	0.06	0.00	2.00	4.49	5.04	48.00	53.00	5.00	3.76	4.65	0.90	47.85	52.93	5.07	14.72	60.48
Pull III	6.40	8.00	1.60	0.06	0.21	0.15	2.00	7.00	10.35	12.04	52.00	52.00	0.00	9.35	10.85	1.51	51.45	51.80	0.35	14.72	60.48
Pull IV	8.00	10.00	2.00	0.21	0.48	0.27	7.00	12.00	16.68	22.99	53.00	53.00	0.00	15.21	20.70	5.49	52.25	52.03	-0.22	14.72	60.48

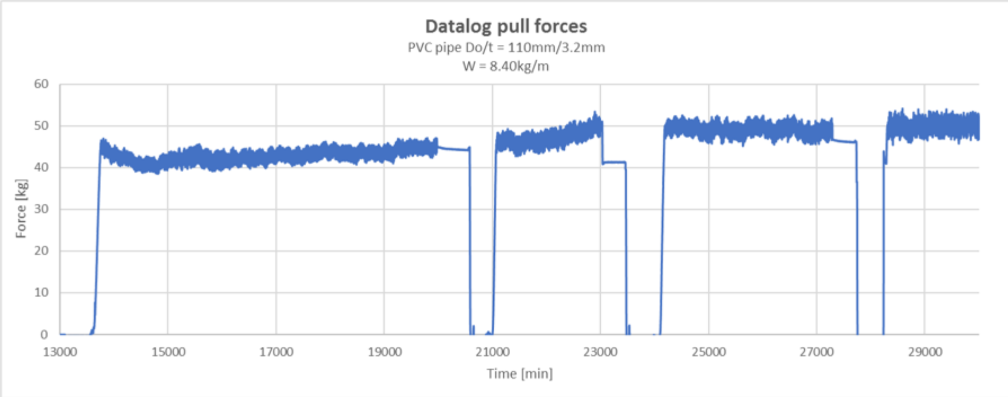

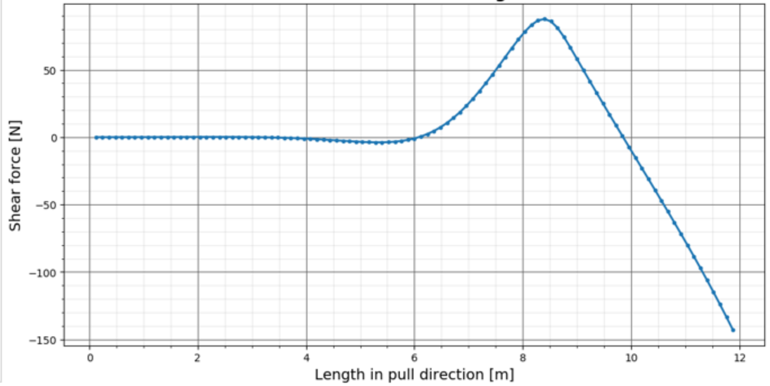

Figure C.1: Summary of experimental data;
Model $D_o/t = 110/3.2[mm]$ and $W = 8.40[kg/m]$,
Test 1

Pull No.	X start [m]	X end [m]	Δ X [m]	Y start [m]	Y end [m]	Δ Y [m]	θ start [°]	θ end [°]	α start [°]	α end [°]	F pull start [kg]	F pull end [kg]	ΔF pull [kg]	F pull lateral start [kg]	F pull lateral end [kg]	Δ F pull lateral [kg]	F pull axial start [kg]	F pull axial end [kg]	ΔF pull axial [kg]	F predicted lateral breakout [kg]	F predicted axial resistance [kg]
Pull I	3.00	5.00	2.00	0.00	0.00	0.00	0.00	0.00	0.00	0.00	50.00	52.00	2.00	0.00	0.00	0.00	50.00	52.00	2.00	14.72	60.48
Pull II	5.00	6.00	1.00	0.00	0.05	0.04	0.00	1.00	4.49	4.74	52.00	48.00	-4.00	4.07	3.96	-0.11	51.84	47.90	-3.94	14.72	60.48
Pull III	6.00	7.00	1.00	0.06	0.21	0.11	1.00	2.00	8.06	7.97	50.00	52.00	2.00	7.01	7.21	0.20	49.62	51.72	2.10	14.72	60.48
Pull IV	7.00	10.00	3.00	0.21	0.62	0.41	2.00	9.00	11.91	16.46	52.00	54.00	2.00	10.74	15.30	4.57	51.22	53.54	2.32	14.72	60.48
Pull V	10.00	11.90	1.90	0.62	1.25	0.63	9.00	14.00	20.37	25.31	55.00	60.00	5.00	19.14	25.65	6.51	53.92	58.83	4.91	14.72	60.48

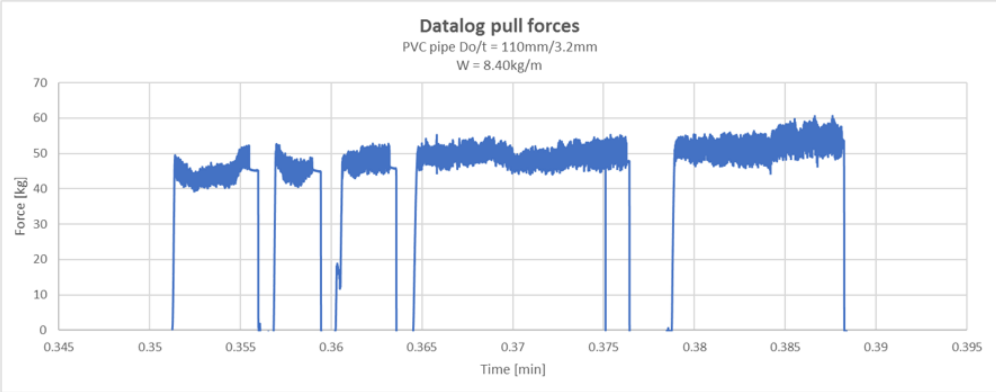

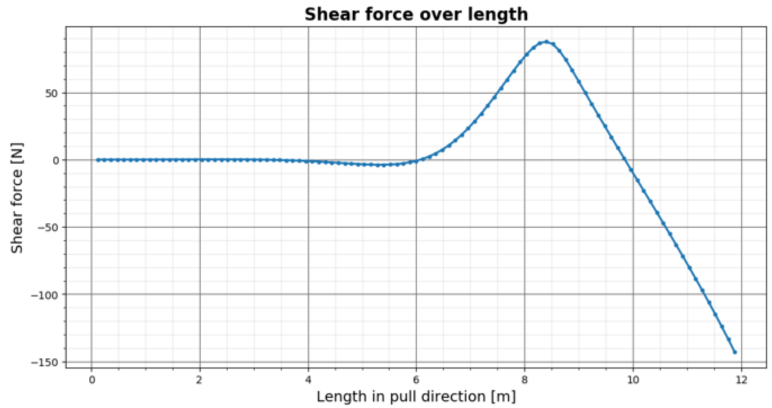

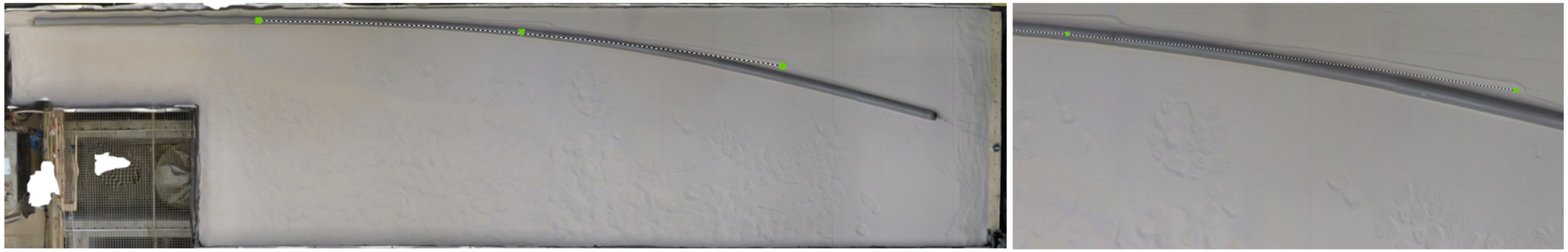

Figure C.2: Summary of experimental data;
Model $D_o/t = 110/3.2[mm]$ and $W = 8.40[kg/m]$,
Test 2

Pull No.	X start [m]	X end [m]	ΔX [m]	Y start [m]	Y end [m]	Δ Y [m]	θ start [°]	θ end [°]	α start [°]	α end [°]	F pull start [kg]	F pull end [kg]	Δ F pull [kg]	F pull lateral start [kg]	F pull lateral end [kg]	ΔF pull lateral [kg]	F pull axial start [kg]	F pull axial end [kg]	Δ F pull axial [kg]	F predicted lateral breakout [kg]	F predicted axial resistance [kg]
Pull I	3.00	5.00	2.00	0.00	0.00	0.00	0.00	0.00	0.00	0.00	62.00	53.00	-9.00	0.00	0.00	0.00	62.00	53.00	-9.00	12.36	60.48
Pull II	5.00	6.00	1.00	0.00	0.06	0.04	0.00	3.00	3.00	2.93	55.00	53.00	-2.00	2.88	2.71	-0.17	54.92	53.00	-1.92	12.36	60.48
Pull III	6.00	7.50	1.50	0.06	0.15	0.11	3.00	5.00	6.36	7.21	53.00	57.00	4.00	5.87	7.15	1.28	52.91	56.96	4.05	12.36	60.48
Pull IV	7.50	11.80	4.30	0.15	0.83	0.68	5.00	10.00	11.55	23.77	57.00	58.00	1.00	11.41	23.38	11.97	56.63	56.33	-0.30	12.36	60.48

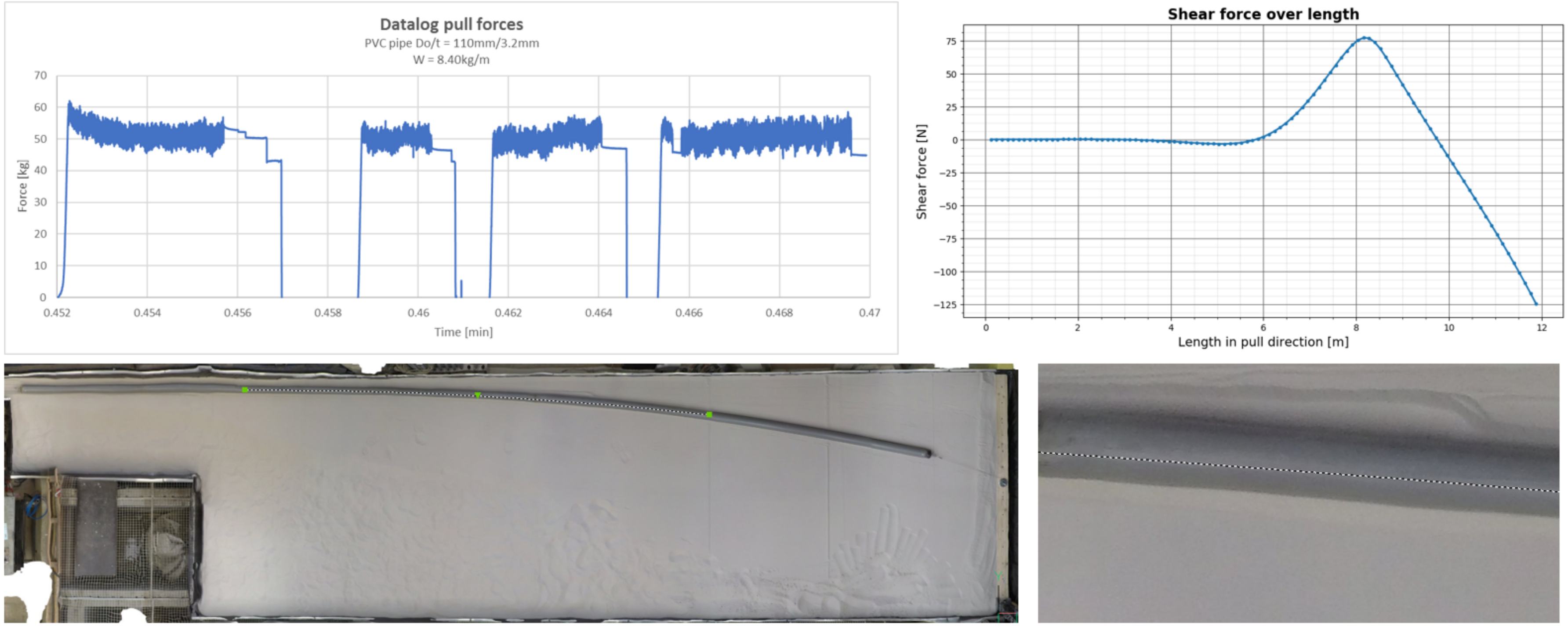

Figure C.3: Summary of experimental data;
Model $D_o/t = 110/3.2[mm]$ and $W = 8.40[kg/m]$,
Test 3

D

Summary experimental data breakout pulls

Pull No.	X start [m]	X end [m]	Δ X [m]	Y start [m]	Y end [m]	Δ Y [m]	θ start [°]	θ end [°]	α start [°]	α end [°]	F pull start [kg]	F pull end [kg]	Δ F pull [kg]	F pull lateral start [kg]	F pull lateral end [kg]	ΔF pull lateral [kg]	F pull axial start [kg]	F pull axial end [kg]	Δ F pull axial [kg]	F predicted lateral breakout [kg]	F predicted axial resistance [kg]
Pull I	0.00	9.45	9.45	0.00	0.00	0.00	0.00	0.00	0.00	0.00	60.00	59.00	-1.00	0.00	0.00	0.00	60.00	59.00	-1.00	0.00	11.66
Pull II	9.45	9.45	0.00	0.00	0.00	0.06	0.00	0.00	26.64	26.64	38.26	14.00	-24.26	17.15	6.28	-10.88	34.20	12.51	-21.68	22.43	11.66
Pull II	9.45	9.45	0.00	0.00	0.06	0.11	0.00	0.00	26.64	25.84	51.52	14.00	-37.52	23.10	6.10	-17.00	46.05	12.60	-33.45	26.50	11.66
Pull II	9.45	9.45	0.00	0.06	0.11	0.17	0.00	0.00	25.84	25.04	58.06	14.00	-44.06	25.31	5.92	-19.38	52.26	12.68	-39.57	28.54	11.66
Pull II	9.45	9.45	0.00	0.11	0.17	0.22	0.00	0.00	25.04	24.22	60.05	14.00	-46.05	25.41	5.74	-19.67	54.40	12.77	-41.64	30.58	11.66

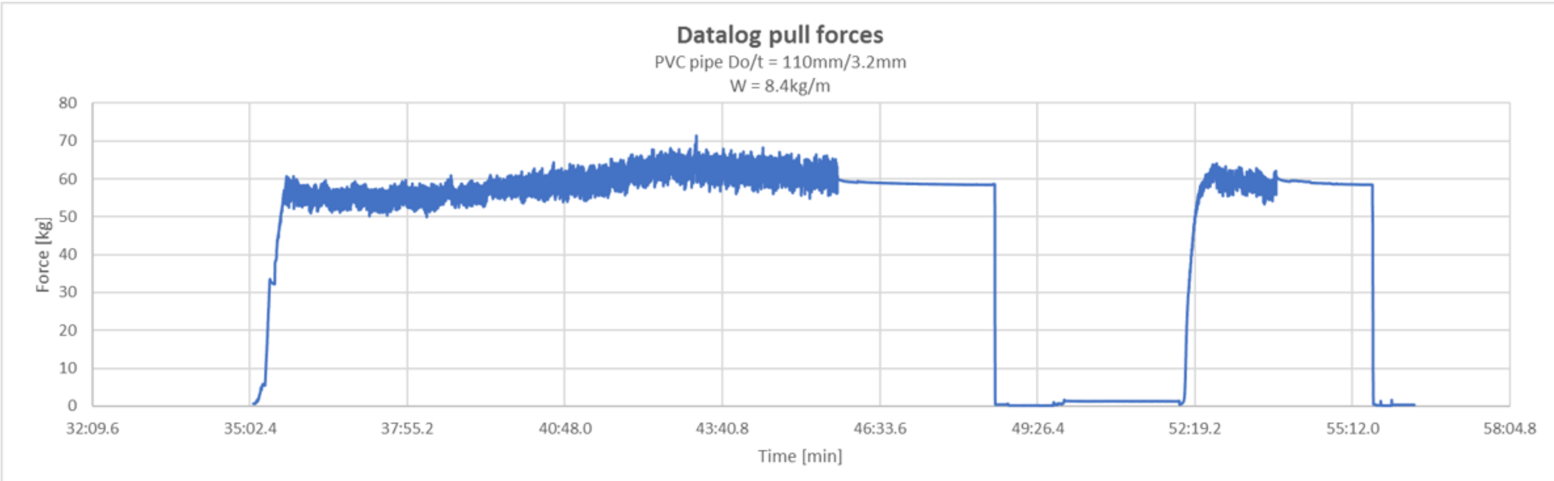

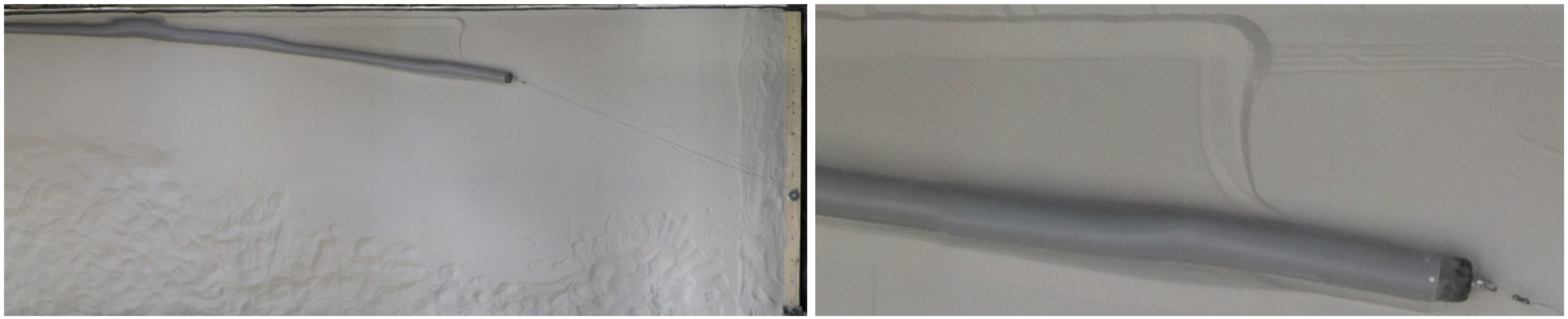

Figure D.1: Summary of experimental data breakout pull
Model $D_o/t = 110/3.2[mm]$ and $W = 8.40[kg/m]$, $z/D = 0.21$

Pull No.	X start [m]	X end [m]	Δ X [m]	Y start [m]	Y end [m]	ΔY [m]	θ start [°]	θ end [°]	α start [°]	α end [°]	F pull start [kg]	F pull end [kg]	ΔF pull [kg]	F pull lateral start [kg]	F pull lateral end [kg]	Δ F pull lateral [kg]	F pull axial start [kg]	F pull axial end [kg]	Δ F pull axial [kg]	F predicted lateral breakout [kg]	F predicted axial resistance [kg]
Pull I	3.00	6.45	3.45	0.00	0.00	0.00	0.00	0.00	0.00	0.00	8.00	9.00	1.00	0.00	0.00	0.00	8.00	9.00	1.00	0.00	9.29
Pull II	6.45	6.45	0.00	0.00	0.025	0.025	0.00	0.00	21.19	20.99	5.00	5.00	0.00	1.81	1.79	-0.02	4.66	4.67	0.01	2.29	9.29
Pull II	6.45	6.45	0.00	0.03	0.050	0.025	0.00	0.00	20.99	20.79	7.00	7.00	0.00	2.51	2.48	-0.02	6.54	6.54	0.01	2.75	9.29
Pull II	6.45	6.45	0.00	0.05	0.075	0.025	0.00	0.00	20.79	20.59	8.00	8.00	0.00	2.84	2.81	-0.03	7.48	7.49	0.01	2.96	9.29
Pull II	6.45	6.45	0.00	0.08	0.100	0.025	0.00	0.00	20.59	20.38	8.50	8.50	0.00	2.99	2.96	-0.03	7.96	7.97	0.01	3.16	9.29

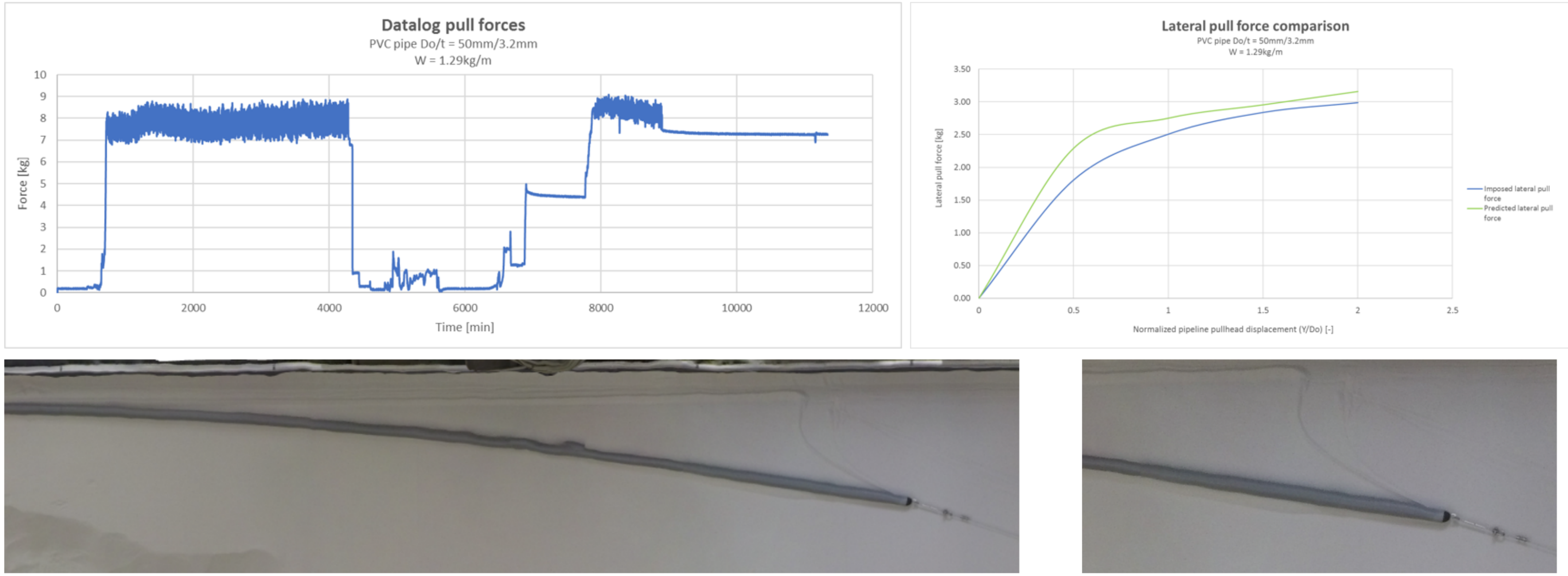

Figure D.2: Summary of experimental data breakout pull
Model $D_o/t = 550/3.2[mm]$ and $W = 8.40[kg/m]$, $z/D = 0.35$